LA-11685-T
Thesis

UC-410
Issued: November 1989

LA--11685-T

DE90 002909

Cross Sections and Analyzing Powers of $^{15}N(p,n)^{15}O$ at 200 MeV and 494 MeV

*Douglas Edward Ciskowski**

*Guest Scientist at Los Alamos.

Los Alamos National Laboratory
Los Alamos, New Mexico 87545

ACKNOWLEDGMENTS

I would like to thank all who helped in the execution of these experiments, specifically, John McClelland, and Terry Taddeucci for guiding me at LAMPF; Tom Carey and Lanny Ray for many helpful conversations; my collaborators Kevin Jones, Roger Byrd, Charles Goodman, Jack Rapaport, Evan Sugarbaker, Larry Rybarcyk, Marti Barlett; and last but certainly not least, my advisor, Gerry Hoffmann.

CROSS SECTIONS AND ANALYZING POWERS OF ^{15}N(p,n)^{15}O AT 200 MeV AND 494 MeV

by

Douglas Edward Ciskowski

ABSTRACT

Differential cross sections and analyzing powers have been measured for the ^{15}N(p,n)^{15}O (g.s.) reaction at bombarding energies of 200 MeV and 494 MeV. The 494 MeV data were obtained at the LAMPF Neutron Time-Of-Flight Facility on an 82 m flight path with a resolution of about 2.7 MeV. The 200 MeV data were obtained at IUCF on a 76 m flight path with a resolution of about 1.1 MeV. At both energies, the measured analyzing power is small, the magnitude is less than .2 for momentum transfers of less than 1 fm^{-1}. In contrast, both Relativistic and standard DWIA calculations predict a maximum of A=-.7 near q=0.7 fm^{-1}.

TABLE OF CONTENTS

CHAPTER 1

INTRODUCTION

One important new advancement in the study of medium energy nuclear physics is the ability to measure cross sections (σ), analyzing powers (A) and polarization transfer coefficients (D_{ij}) for nucleon-nucleus scattering. Measurement of such sets of observables for select transitions can provide needed specific information about specific elements of the NN effective interaction or transition amplitude and provide concise tests of relativistic and non-relativistic models of nucleon-nucleus scattering.

Early studies with (p,p') elastic and inelastic scattering established the need to measure spin observables[1-2]. The first measurements of analyzing powers and the spin-rotation function Q led to the current prominence of relativistic treatments of the data[3-4].

Elements of the reaction, different and distinct from those studied in (p,p') experiments can be studied with the (p,n) reaction due to the pure isovector nature of the probe. It allows selection of the strength of the pseudoscalar NN amplitude which is contaminated by other factors in the even-even target nuclei of proton-nucleus elastic scattering studied thus far[5]. Data for these (p,n) studies at medium energy can now be obtained at The Neutron Time Of Flight Facility at Los Alamos Meson Physics

(NTOF), The Indiana University Cyclotron Facility (IUCF) and TRIUMF, Vancouver, Canada. The experiments done for this work were completed at NTOF and IUCF.

Measurement of data which selects specific pieces of the interaction could constrain the isovector components of the intermediate energy NN effective interactions, give insights into the effects of the nuclear medium and test relativistic and nonrelativistic models of nuclear structure. Ray and Shepard[6] have proposed, using Relativistic Impulse Approximation (RIA) calculations utilizing the pseudovector form of the pseudoscalar component of the Lorentz invariant NN amplitude, a schema for analyzing isobaric analog ($\vec{p}$,n) reaction at intermediate energies for light odd-A nuclei.

Two different forms of the relativistic invariant NN amplitude have been proposed by Horowitz[7] and Tjon-Wallace[8]. Both forms show some success in their description of proton-nucleus elastic scattering data below 400 MeV by treating the exchange term explicitly and by substituting a pseudovector term in place of the pseudoscalar term of the original Relativistic Impulse Approximation (RIA) prescription. However, the strength of the pseudoscalar NN amplitude is contaminated by other terms of the amplitude in the even-even target nuclei of proton-nucleus elastic. In studies above 400 MeV, little sensitivity to the pseudoscalar or pseudovector form has been found[9]. Ray and Shepard[6] have shown that the purely isovector nature of (p,n) reactions would clear up the ambiguity of the pseudoscalar versus pseudovector terms.

In the charge exchange reaction, a neutron is replaced by a proton. In this way, the (p,n) reaction is related to β decay. In β decay, a neutron decays into an electron, a neutrino and a proton. Weak interactions are of such short range that the

spatial wave function of the initial and final nucleon states must match exactly. Thus for allowed decays, $\Delta L=0$; the angular momentum cannot change. The types of change that can occur are a flip in the isospin alone and a flip in the isospin paired with a change in spin.

For low momentum transfers, there are two (p,n) transitions which are analogous to β decay. These are the Fermi and Gamow-Teller (GT) transitions.

Where both of the spatial and spin states of the initial and final wave functions are the same, the isospin flip transition is called a Fermi transition. The Fermi transition is mediated by the $(\vec{\tau}_1 \cdot \vec{\tau}_2)$ term in the effective NN interaction, where $\vec{\tau}_1(\vec{\tau}_2)$ is the isospin transition operator of the target (projectile). The case when the spatial parts of the initial and final wave functions are identical but the spin states change for an isospin flip transition is called a Gamow-Teller transition. The Gamow-Teller transition is mediated by the $(\vec{\tau}_1 \cdot \vec{\tau}_2)\cdot(\vec{\sigma}_1 \cdot \vec{\sigma}_2)$ term in the effective NN interaction, where $\vec{\sigma}_1(\vec{\sigma}_2)$ is the spin transition operator of the target (projectile).

When a Fermi (or GT) transition leaves the resultant or daughter nucleus in the same state as the parent except for the flip in isospin (or spin and isospin), such states are known as Isobaric Analog States, (IAS). It is the Fermi transition which leads to the IAS in even-even target nuclei.

The (p,p) elastic transition is primarily determined by the isoscalar portion of the NN effective interaction and the proton and neutron ground state densities, while showing little sensitivity to the isovector portions which determine the (p,n) transitions. The (p,n) reaction allows study of the spin and isospin exchange within a nucleus and by measurement of

specific spin-isospin structure strengths, can select certain features of the nucleon-nucleus interaction.

Early proton-nucleus data analyzed with simple non-relativistic models established that such studies were sensitive to underlying nuclear structure[10-12]. Cross section and analyzing powers were measured in an attempt to determine neutron densities within the nucleus. At the time, this was thought to be where the current theories needed input most[13]. Analyzing powers were measured to study the role of spin effects in elastic scattering. Both the proton-nucleus spin-orbit amplitude and the spin-independent amplitude contributed to proton-nucleus scattering. As data was obtained, it became apparent when using solutions from fits to spin-orbit and spin-independent proton-nucleon data, the analyzing powers for proton-nucleus data could not be fit[14]. A non-relativistic Kerman-McManus-Thaler[15](KMT) analysis used to fit the data could fit the cross section well but not the analyzing power.

The spin-rotation function Q, defined by in plane spin transfer parameters, ($Q(\theta)=D_{LS}\cos(\theta)_{Lab}+ D_{SS}\sin(\theta)_{Lab}$), was found to be sensitive to a part of the proton-nucleon amplitude different from that of the cross section and analyzing power measurements[16]. Measurements of Q proved different from predictions derived from the best fit corresponding to the cross section and analyzing power data.

It was not until the phenomenological Dirac optical model approach was used that quality fits to both cross section and analyzing power data were able to be made[17]. This relativistic approach used an optical potential based on a Lorentz scalar potential and the time-like components of a Lorentz vector potential.

Early (p,n) studies measured angular distributions and energy dependences of cross sections and analyzing powers.

The isovector nature of (p,n) brought to light important information on GT giant resonances and the general form of their strength functions[18]. This greatly contributed to the description of effective NN interactions.

The (p,n) IAS reaction is in many ways analogous to (p,p') elastic scattering. The new information which will be gained from cross section and analyzing power measurements of (p,n) isovector IAS transitions should provide tests to specific terms of relativistic and non-relativistic models as was done with earlier (p,p') isoscalar data.

The cross section measurement is sensitive to the pseudoscalar versus the pseudovector term of the NN amplitude and can provide information on distortion effects and medium corrections. It gives the relative contribution of the Fermi portion and the Gamow-Teller portion of the transition amplitude. This is important as the spin observables are cross section weighted averages of the Fermi and Gamow-teller contributions.

The analyzing power of a 0^+ transition is predicted to have a large magnitude. Conversely, the analyzing power for a 1^+ transition is predicted to be small. Thus the analyzing power for a mixed transition is dependant upon the ratio of Fermi to Gamow-Teller contributions. By constraining either the Fermi/GT ratio or the analyzing power, the other can be determined (where both strengths are non-zero).

The spin transfer coefficient D_{nn} is sensitive to the spin flip. $\Delta S = 0,1$ at energies below 200 MeV and easily distinguishes between the two cases. It is also sensitive to the pseudoscalar versus pseudovector term in relativistic and non-relativistic models. As the incident energy increases to the 500 MeV region, this sensitivity is lost as new terms of the interaction, such as the tensor (exchange) interaction, begin to dominate[19].

The analyzing power is the easiest spin observable to measure. It can be measured simultaneously with the cross section. As in Appendix A;

$$\sigma(\theta,\phi) = \sigma_o(\theta)(1 + p_i A(\theta)\cos\phi) \qquad (1)$$

where p_i is the polarization of the incoming beam and $\cos\phi$ = 1(-1) for particles scattered to beam left (right) for a beam polarized normal to the scattering plane. Thus by reversing the spin polarization, a stationary detector can measure $\sigma(\theta,\phi)$ for spin states normal ($\sigma_N(\theta,\phi)$) and reverse ($\sigma_R(\theta,\phi)$):

$$\sigma_N(\theta,\phi=0°) = \sigma_N(\theta) = \sigma_o(\theta)(1 + p_i A(\theta))$$

$$\sigma_R(\theta,\phi=180°) = \sigma_R(\theta) = \sigma_o(\theta)(1 - p_i A(\theta))$$

and

$$\sigma(\theta) = \frac{\sigma_N(\theta) + \sigma_R(\theta)}{2} = \sigma_o(\theta) \ . \qquad (2)$$

The analyzing power is then;

$$A(\theta) = \frac{\sigma_N(\theta) + \sigma_R(\theta)}{2\, p_i\, \sigma_o(\theta)} \ . \qquad (3)$$

The cross section, analyzing power and spin transfer coefficients D_{ij} are defined in appendix A. For spin normal beam, the spin observables are related by:

$$p_j = \frac{P(\theta) + p_i D_{nn}(\theta)}{1 + p_i A(\theta)} . \qquad (4)$$

It has been shown that by measuring a complete set of spin observables for the charge exchange IAS g.s.⇒g.s. transition, progress can be made in untangling parts of the reaction though significant gains can be made through measuring cross sections of beam polarized in the transverse direction and cross sections of beam polarized in the longitudinal directions, analyzing powers and D_{nn}[6]. A $0^+ \Rightarrow 0^+$ IAS transition has $\Delta J = 0$ which implies that the scattering matrix, M, is equal to the identity matrix, I; M=I and for $D_{nn}(\theta)$ normalized to unit cross section, $D_{nn}(\theta) = Tr(\sigma_n \sigma_n) = 1$. At 0°, left/right asymmetries as defined by $P(\theta)$ and $A(\theta)$ are undefined so that $P_j(0) = A(0) = 0$ and $p_j = p_i(\theta) \cdot D_{nn}(0) = p_i$. The incoming polarization at 0° is equal to the outgoing neutron polarization making it a practical "source" of polarized neutrons for polarimeter calibration. By imposing time invariance on an IAS g.s.⇒g.s. transition, a mirror transition, we can write:

$$Tr(MM^{\dagger}\sigma_i) = Tr(M\sigma_i M^{\dagger}) . \qquad (5)$$

where σ_i are the Pauli spin matrixes. This is model independent to the extent that isospin is conserved and kinematic effects are minimal. As shown in appendix A, $P(\theta) \equiv A(\theta)$ for such a transition.

The IAS transitions can be studied most readily in light nuclei. In light nuclei, the separation between energy levels of the transition of interest and their nearest neighbors is generally large enough to be resolved by the apparatus at NTOF and IUCF. The resolution available at IUCF allowed study of the $^{14}C(p,n)^{14}N(2.31\ MeV)$ transition, the $^{13}C(p,n)^{13}N(g.s.)$ transition

and the $^{15}N(p,n)^{15}O(g.s.)$ transition. Results of earlier studies at IUCF showed that the cross section of the ground state of the $^{13}C(p,n)^{13}N$ reaction and the 2.31 MeV state of the reaction $^{14}C(p,n)^{14}N$ had greatly reduced as the incident energy raised from 80 MeV to 160 MeV. This combined with the fact that the resolution available at NTOF could not always adequately resolve the carbon states with the available temporary 85 m flight path. indicated that the only useful data which could then be obtained at 500 MeV at NTOF was from ^{15}N.

The $^{14}C(p,n)^{14}N(2.31\ MeV)$ transition is different from the others mentioned in that the $0^+ \Rightarrow 0^+$ IAS transition is a pure Fermi transition so that $P(\theta)=A(\theta)$. The state separation in $^{14}C(p,n)^{14}N$ requires the overall resolution be at most 1 MeV. This limits experimentation with ^{14}C to thin targets and longer flight paths and consequently, longer running times.

The $^{13}C(p,n)^{13}N(g.s.)$ transition is a mixed Fermi-GT transition. As it is an IAS transition, $P(\theta) \cong A(\theta)$. In the simplest shell model picture, it can be described as a $1p_{1/2}$ state with a closed shell core. It has been shown that the spin structure of the IAS transition amplitude for this transition is identical to that of the $^{13}C(p,p')$ elastic scattering amplitude where isospin invariance is assumed and the kinematic differences between the initial and final states is assumed[20]. The spin observable description is then analogous to those used in $^{13}C(p,p')^{13}C$ elastic scattering. The resolution required for $^{13}C(p,n)^{13}N$ is of the order of 1 MeV which makes data analysis more difficult.

The $^{15}N(p,n)^{15}O(g.s.)$ IAS transition is also a mixed Fermi-GT transition where $P(\theta) \cong A(\theta)$. The same physics of interest here can be obtained from the $^{15}N(p,n)^{15}O(g.s.)$ transition as well as the $^{13}C(p,n)^{13}N(g.s.)$ transition. The IAS mirror transitions are simple to calculate as the final and initial wave functions are the same. This minimizes the model dependency of these

functions. The ^{15}N wave function can be described as a closed neutron p shell with a $1p_{1/2}$ proton hole. This simple description makes it a desirable target theoretically. The first excited state seen in $^{15}N(p,n)^{15}O(g.s.)$ is 6.2 MeV above the ground state so that the states are easily resolved.

Distorted Wave Impulse Approximation, (DWIA), and RIA predictions for $^{15}N(p,n)^{15}O(g.s.)$ which predict a strong negative analyzing power, for energies near 500 MeV, just as was seen in similar transitions at 160 MeV and below[21]. At these lower energies the DWIA and RIA describes the data well. A large analyzing power, combined with the energy spread of 6.2 MeV between the ^{15}O first excited state and its mirror transition ground state would make it a good candidate as a neutron polarimeter calibration target using $P(\theta) \equiv A(\theta)$. Thicker targets and shorter flight paths would then make this a desirable substitute for the $^{14}C(p,n)^{14}N(2.31\ MeV)$ transition as a polarimeter calibration reaction.

A reaction's suitability as a polarized neutron production target is determined by the Figure of Merit, FOM, which is defined by $\sigma(\theta)*A^2(\theta)$. The statistical uncertainty of the effective analyzing power, A_ε, measured in the calibration of a polarimeter can be approximated by:

$$\delta A_\varepsilon = \frac{1}{P_f\sqrt{N}} \qquad (6)$$

where N is total number of neutrons detected and P_f is the final polarization of the neutrons leaving the production target. For the $^{15}N(p,n)^{15}O(g.s.)$ transition, $P(\theta) \equiv A(\theta)$. The cross section is directly proportional to N so that:

$$\delta A_E \propto \frac{1}{\sqrt{A_E^2 \sigma}} \propto \frac{1}{\sqrt{F\ O\ M}} \quad . \tag{7}$$

Thus, in order to minimize δA, the FOM must be maximized.

Due to the simple description, the required resolution and the predicted FOM, ^{15}N was chosen as the target with which the study at 500 MeV would be done.

III THE PRESENT EXPERIMENTS

This work is a measurement of $(\vec{p},n)$ cross section and analyzing power for ^{15}N, ^{13}C and ^{14}C at 200 MeV and ^{15}N and ^{13}C at 494 MeV. The first experiment was done at IUCF with an incoming polarized 200 MeV proton beam. It was done in May of 1986 using time of flight techniques for measurements covering an angular range of 0° to 18° in approximately 3° steps. The experiment had an average beam polarization of 72 ±2% and an average beam current of 40 nA. The second experiment was part of the commissioning activity for the new NTOF Facility. It utilized an incoming polarized proton beam energy of 494 MeV, an average beam polarization of 74 ±3% and an average beam current of 4 nA. This phase of the study was run from November 18-27, 1987 and covered and angular range of 0° to 16°.

The NTOF swinger vault, detector system, electronics and software were completed. A temporary short flight path of 82 meters was needed to commission the facility, test the ^{15}N reaction for suitability as a polarimeter calibration target and produce useful physics while the long flight path was being constructed.

CHAPTER 2

EXPERIMENTAL SET UP

Experimental hardware and software will now be discussed. The discussion will include the polarized beam, its transport to the NTOF target, the transport of the neutron beam to the detectors, the detectors and the NTOF experimental electronics. It will include the NTOF calibration and acquisition software and be followed by a similar discussion of the IUCF facilities.

I NTOF HARDWARE

I A THE LAMPF POLARIZED ION SOURCE

The polarized beam of protons is provided by the Polarized Ion Source. The Polarized Ion Source at LAMPF is a Lamb Shift source[22].

The beam production process starts as the duoplasmatron produces H^+ ions. The H^+ ions are pulled to a cesium cell by a grid electrode. Once in the cesium, some of the ions undergo charge exchange to produce neutral hydrogen atoms. The residual positive and negative ions that are stripped with a magnetic field as they leave the cesium cell.

Approximately 43% of the neutral hydrogen atoms are in the 2S state as they proceed to the spin filter where they are subjected to a magnetic field. This splits the $2S^1/2$ and $2P^1/2$ levels of hydrogen as shown in Figure 1. The hyperfine structure becomes readily apparent in the magnetic field. The hyperfine splitting of the $2S^1/2$ states are labeled alpha and beta states in Figure 1 and of the $2P^1/2$ states are labeled e and f.

The $2P^1/2$ states have a half life of 1.6 ns and quickly decay to the ground state. The $2S^1/2$ state has a .1 s half life and remains. In order to strip the beta states of the $2S^1/2$, it is noted that the $2S^1/2$ beta and the e state of $2P^1/2$ are degenerate in an external magnetic field of 575 gauss. These states can be mixed by the Stark effect by applying a small transverse static electric field. Thus the $2S^1/2$ beta states are leached to the $2P^1/2$ and decayed to the ground state.

One of the two remaining alpha states must also be quenched to leave an unambiguous polarization. This is achieved by inducing one of the alpha states to decay to a beta state (and subsequently $2P^1/2$ and ground state) by pumping photons of the same energy as the energy separation between the beta state and the requisite alpha.

Both quenched ground state and polarized $2S^1/2$ state atoms proceed to a cell of argon. Here, the atoms in the $2S^1/2$ state preferentially capture an electron as do a small fraction of the ground state atoms. An axial magnetic field is maintained in the cell to keep the $2S^1/2$ state atoms from depolarizing as they capture an electron. This gives a beam whose polarization is orthogonal to the direction of propagation and over 70% aligned in the direction transverse to the direction of propagation. Reversing this field reverses the polarization of the the beam. Spin precession during transport to the target is compensated for so that the beam will arrive polarized in the desired (vertical)

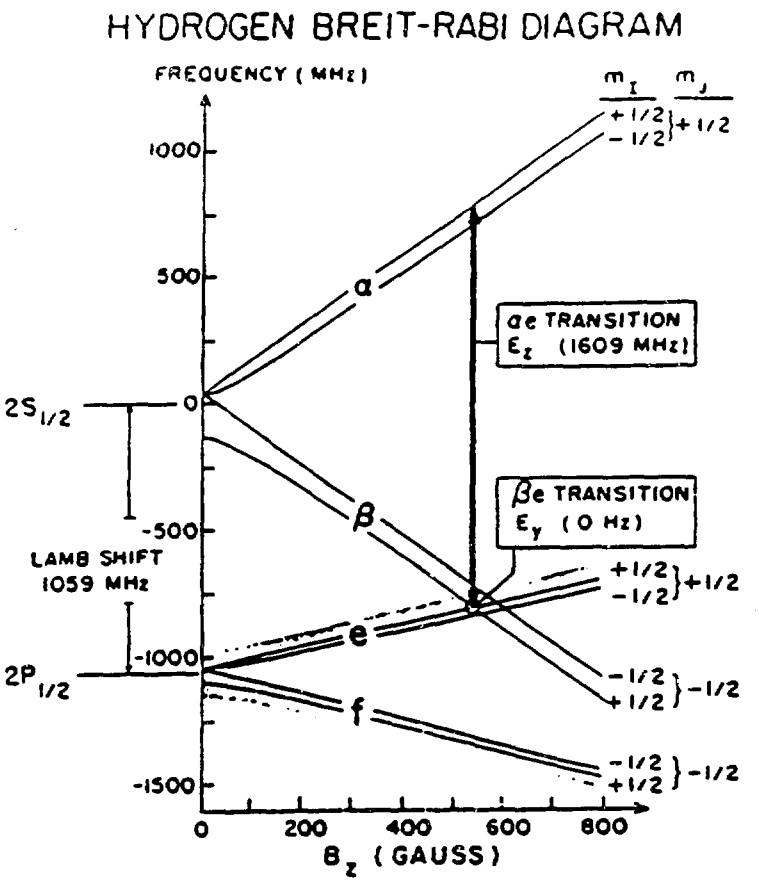

Figure 1 Hydrogen Breit-Rabi Diagram showing the hyperfine level splitting of the $2s_{1/2}$ and $2p_{1/2}$ states in a magnetic field as used in the Lamb Shift Source.

direction. In this experiment, the polarization was reversed once a minute to cancel systematic errors during the A measurements.

I B BEAM ACCELERATION AND TRANSPORT

There are three sources which provide different beams to the accelerator. The source and beam mentioned in all NTOF discussions will be those used in this experiment; the P^- source and beam. The beam from the ion source is accelerated to 494 MeV and bunched with normally unused LINAC modules. The beam is then steered into the NTOF line through the standard line X beamline devices. Once in the NTOF cave, it is directed to hit the target at the desired angle with the NTOF swinger magnets. Protons from the target are swept to a beam dump by a sweep magnet while the neutrons head down the flight path. Neutrons emitted at the selected angle proceed down the flight path to the detectors in the detector hut. The ions are bunched so as to have the micropulse of neutrons arriving at the detectors focused in time, that is, at the same time in energy-time phase space.

I B 1 LINAC

In between the ion source and the main accelerator are elements which make up the P^- Buncher. The source pulses at 120 Hz. The buncher pulsed the polarized beam from the ion source at a frequency of 201.25 MHz or about every 5 ns. These "buckets" are supplied to the buncher, which collects up to 20 RF cycles into a single bucket every 100 ns. The 100 ns signal

imposed on the beam here is also sent to the counting house as a relative time signal showing when the beam pulse is expected. The buncher puts approximately 50% of the DC beam into the LINAC acceptance once every 100 ns with a ramped E field. The remainder of the protons are out of the LINAC acceptance and are lost from the beam.

The first section of the LINAC is a Alvarez design drift tube LINAC. The four chambers of this section contain 165 drift tube acceleration chambers to accelerate the beam from the injector's 750 keV to 100 MeV. The beams being accelerated are phased with the RF resonance of the accelerating cavity when they are injected so that they are exposed to the RF E field with the correct directional vector for the polarity of the beam, i.e., the H^+ and H^-/P^- are injected 180 degrees out of phase. During the times when the beam is out of phase with the RF, it is in the drift tubes which shield the beam.

The main section of the LINAC is a series of side-coupled cavities[22,23] as shown in Figure 2. In this system, each successive cavity is coupled to the next by a small coupling cavity. These coupling cavities supply the main accelerating cavities with their RF power. Careful physical distortions of the coupling cavities allow for fine tuning of the shape of the accelerating field so that each cavity has a $\pi/2$ phase shift from the preceding cavity. This coupling eliminates the need for drift tubes.

As the beams accelerate, the cavities must naturally become longer. The 4800 cavities of the LINAC are grouped into 48 modules for control and power supply purposes. Each module has separate voltage amplitude and phase controls. This is crucial to the rebunching scheme discussed in the next section.

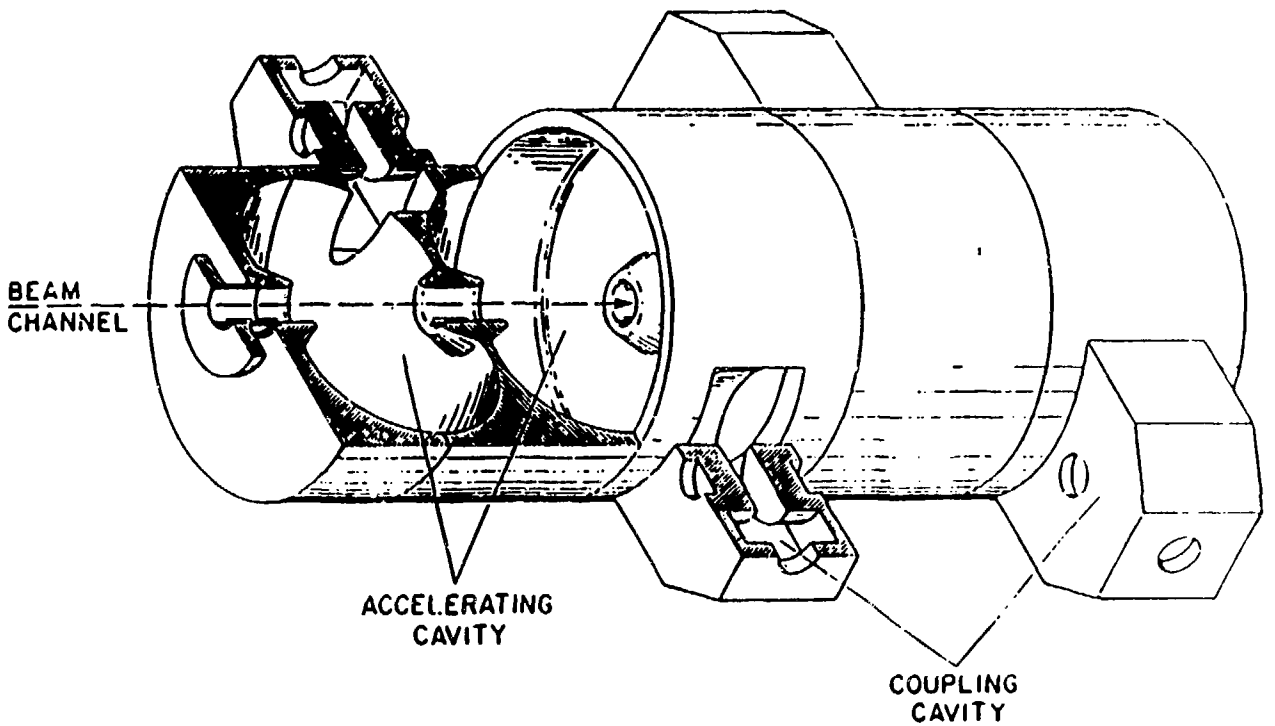

Figure 2 Side Coupled Cavity. cutaway view.

The power supplies provide 805 MHz RF power. This periodicity can send a group of protons (a bucket) through the LINAC approximately every 1.2 ns. The beam was limited by the periodicity of the source and the timing needs of the experiment to one bucket every 100 ns. The 100 ns pulse in the LINAC is also known as a micropulse while the 120 Hz source structure which contains the micropulses is known as a macropulse.

These acceleration cavities produce a finite time resolution and energy resolution from the last accelerating module (LAM). At 500 MeV, these resolutions are typically 1 MeV and 60 ps. This distribution in energy causes the micropulse to further spread in time as the higher energy particles out run the mean energy particles and the lower energy particles fall behind. This drift contributes to the time resolution according to;

$$\Delta t_E = \frac{M_p^2 l_p \Delta E_o}{P_p^3 c} \quad . \tag{8}$$

Here, M_p is the proton mass, P_p is the mean proton momentum, ΔE_o is the full width, half maximum of the energy spread out of the LAM and l_p is the distance from the LAM to the target.

Acceleration modules are used only up to the point where the required beam energy has been reached. After that point, all remaining modules are turned "off" as the beam passes through them. That is, the RF allows that beam to pass unchanged while still operating on the other beams being accelerated at different times as needed.

I B 2 REBUNCHER

The protons' drifting can be used to the advantage of the experimenter for energies below 800 MeV by means of the High Energy Rebuncher (HER).

As each micropulse travels through the accelerator, the energy spread causes another contribution to the timing resolution. The proton beam is steered with magnetic fields and the path through a magnetic field is dependent on the velocity of the proton. Therefore, protons of different energies have different path lengths and times of arrival from the LAM to the target. It can be shown that this path length difference is given by

$$\Delta t_{path}^2 = \frac{1}{\beta_p^2 c^2} \sum_i \left(\frac{\partial l}{\partial \alpha_i}\Delta\alpha_i\right)^2 \quad \alpha_i = X_o, Y_o, \theta_o, \phi_o, l_o, \delta \ . \qquad (9)$$

Here, β_p is the mean velocity of the proton divided by the speed of light and α_i represents the relative initial position of the beam within the beamline with respect to transverse horizontal position, transverse vertical positions, associated angles, path length and the percent uncertainty in the proton momentum, δ.

The initial distribution of particle energies is not correlated to the initial spatial distribution within the packet in any known way. The effects of drift and manipulation upstream of the target are therefore best handled theoretically with a Monte Carlo simulation. A code exists which describes all of the magnets and other elements in the accelerator. This code, called SIMALAC, predicts the energy verses time phase space shown in Figure 3. As the micropulse drifts, this ellipse shears along the axis showing relative time of arrival. The HER reflects the ellipse across this axis by shifting higher energy

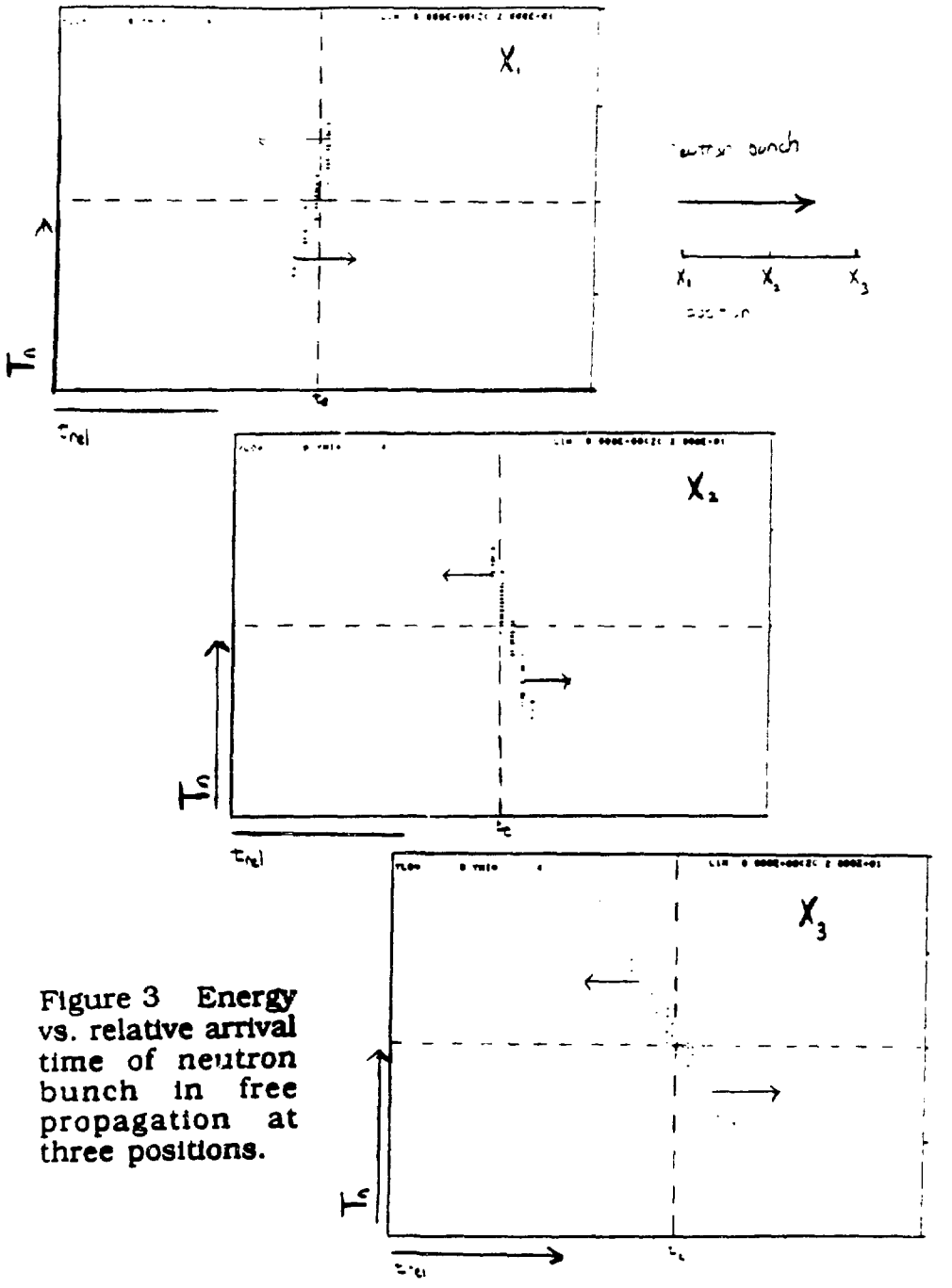

Figure 3 Energy vs. relative arrival time of neutron bunch in free propagation at three positions.

particles to lower energy particles and vice versa. Thus, the particles below the horizontal axis drift to earlier arrival relative times and those above drift to later relative arrival times. It is possible to have them cross at a point where the only time contribution from the accelerator is the intrinsic ellipse width.

As the proton beam drifts through the "off" modules of the LINAC, the micropulse will begin to expand in space and time. This is due to the coulomb repulsion between the protons in free space and the velocity distribution of the individual protons within the pulse. As the proton envelope spreads out in time, the time spread of their arrival time at the detectors also spreads. This directly degrades the timing resolution of the time of flight to the detectors as can be seen in the test results shown in Figure 4.

In an accelerating module of the LINAC, a sinusoidal E field (RF signal) is applied to the micropulse. It is timed so that the protons within the pulse which have a higher initial velocity to begin with receive the lower E field acceleration while the slower protons receive a stronger push. Thus, the pulse is focused in time during acceleration. This process can be altered so that the faster protons are slightly decelerated while the slower protons are slightly accelerated without changing the mean velocity of the beam. This is called bunching and is merely a reapplication of an accelerating module. By switching "on" a module at the desired phase of the beam micropulse as the protons drift through, we can bunch the neutrons so that this minimum in time spread occurs as they reach the detectors. Care must be taken in adjusting the phase as any small maladjustment can change the mean energy of the beam.

For our 494 MeV run, module 36 was used for bunching while module 30 was the last accelerating module. The effects of bunching with module 36 were calculated using the

SIMALAC[24] program and a change in Δt from 1.8 ns to .4 ns was predicted at the detectors. Figures 5 and 6 show tests run at the Weapons Neutron Research area (WNR) at LAMPF with the buncher on and buncher off. Overall resolution due to bunching was thus brought to the level of the detector timing resolution with a final time resolution at NTOF of .5 ns for neutrons. Thus from this WNR data with the high energy rebuncher, timing resolution can be changed from 490 ps to 80 ps typically at 500 MeV for a 240 meter flight path.

The relative timing of the micropulse arrival at the target to the 100 ns buncher signal can change due to a number of things. The relative phase of the HER is crucial as a shift in phase would cause the "zero cross" between decelerating the fast particles and accelerating the slow particles to move away from the mean energy of the beam. Thus, the mean energy of the beam would change as well as the focuses in time. The trigger electronics is phased to the timing signals of the accelerator so that time drifts can occur, thereby degrading the apparent neutron energy resolution.

I B 3 POLARIMETER

Beam polarization was continuously monitored during the experiment. A check that A (0)=0 for the $^{15}N(p,n)^{15}O$ reaction was completed before data was taken with polarizations from two polarimeters, NTP0 and EPP0, one Secondary Emission Monitor (SEM) and one ion chamber called NTER01 and NTER02 respectively. The locations of these elements are pictured in Figures 7-8. Typically, they showed that polarization held steady to within three percent for each target and A (0) was identically zero to within +/- .02. A discussion of the polarimeter

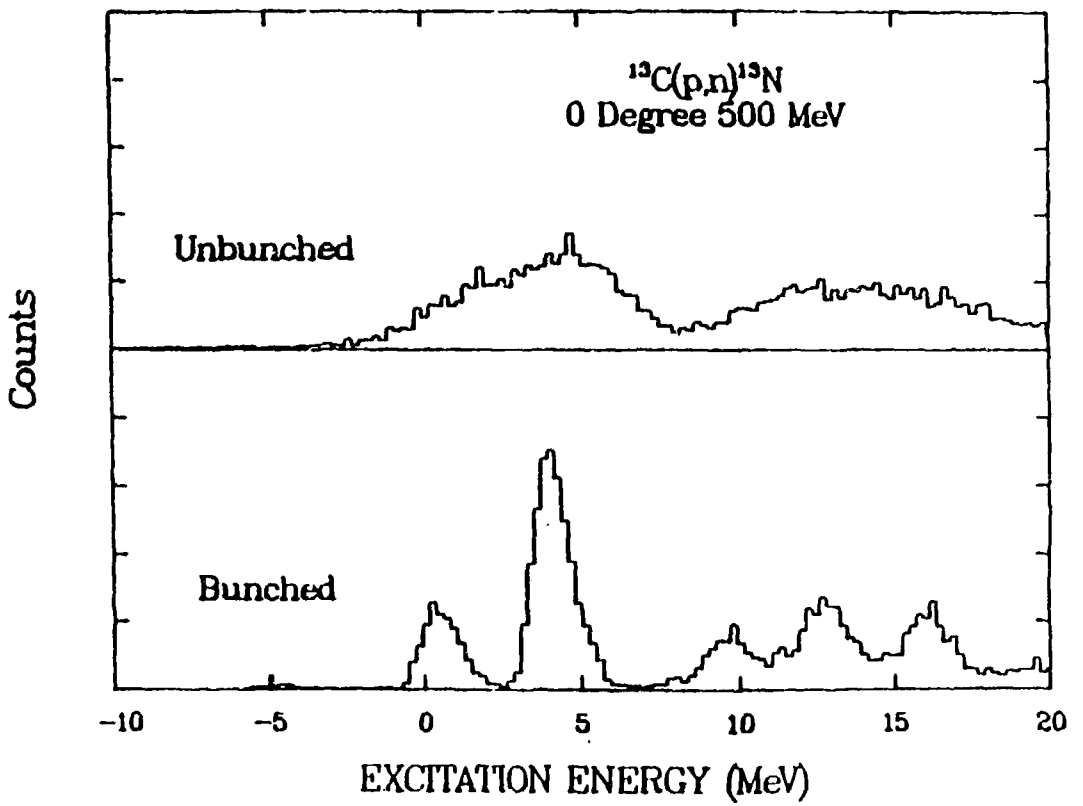

Figure 4 Buncher Developement results taken at WNR[17].

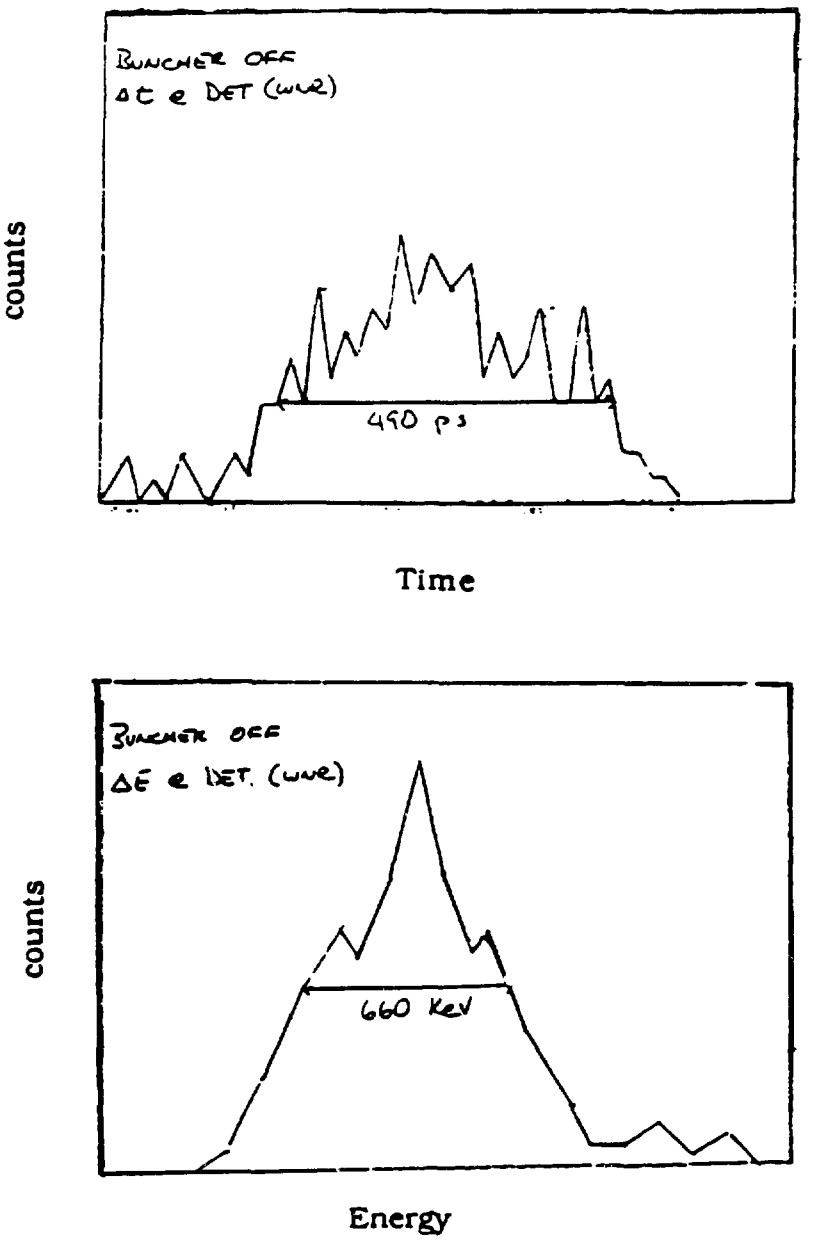

Figure 5 Buncher off resolutions.

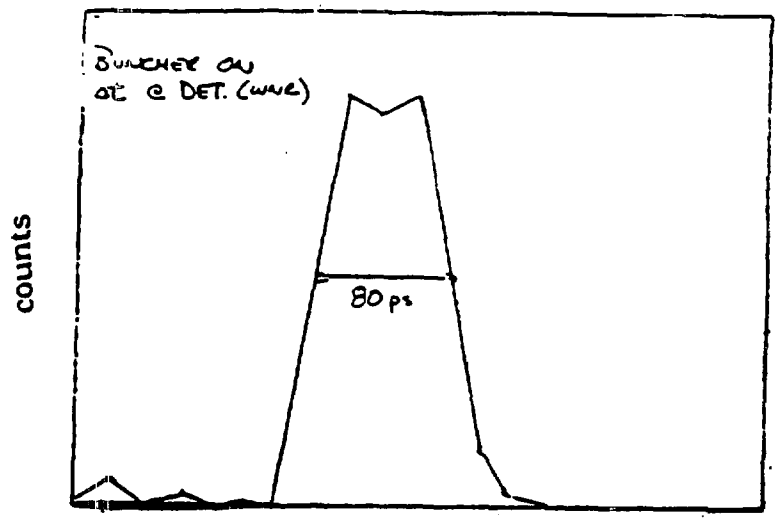

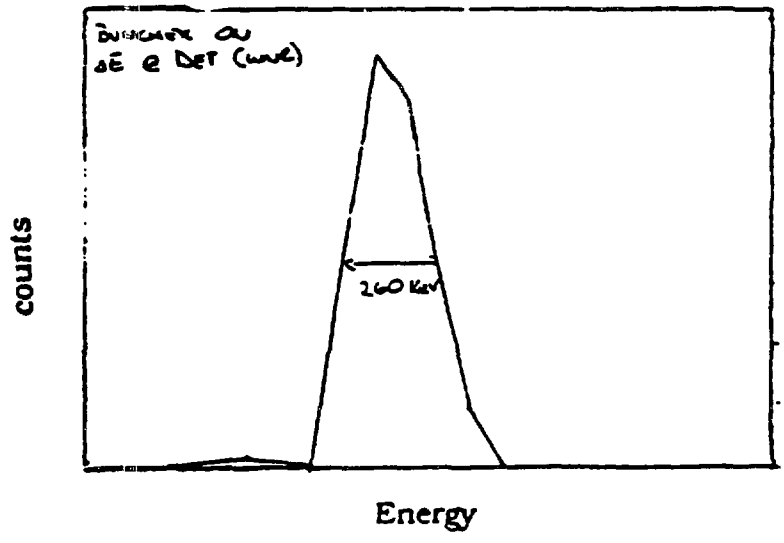

Figure 6 Buncher on resolutions.

analysis follows in Chapter 3, section 1 A. The location of the swinger cave and the NTP0 polarimeter is shown in Figures 7 and 8.

NTP0 was a new polarimeter being tested for the NTOF beamline. It is placed just downstream of the External Proton Beam (EPB) area switcher magnet while EPP0 is upstream of the switcher. The beam was polarized in the n direction. As the switcher magnet's field was also in the n or vertical direction, (neglecting fringe fields), the polarization direction did not precess and EPP0 measured the same polarization as NTP0.

The forward, 17° arm of NTP0 consists of two small scintillators forming a telescope aligned to limit the solid angle available to the polarimeter target. The rear arm, on the opposite side of the beam, consists of one 1" x 1" scintillator and one 1.25" x 1.25" scintillator telescoped to catch the recoil particle. There are four such pairs, labeled by their forward arms. A hit, or scatter, was defined when both detectors in the forward arm and both detectors in the conjugate arm fired. NTP0 was designed to handle the higher current expected from the high intensity source when it comes on line. The counting rate in a scintillator is proportional to the solid angle it subtends with respect to the target of scintillator[25]. In NTP0, the scintillator volume was designed to be low to accommodate the new high intensity source rates. Instead of large thin detectors, the forward arm was designed with .5x .5x .25 inch thick scintillators. The small size of the detectors made alignment with the target difficult. This was the greatest source of uncertainty in the polarization as measured by this polarimeter. NTP0 was designed to detect a coincidence for a ~17 degrees forward scattered proton and its 68 degrees scattered recoil proton. This corresponds to elastic pp scattering from CH_2 targets at LAMPF energies. The analyzing power of pp elastic

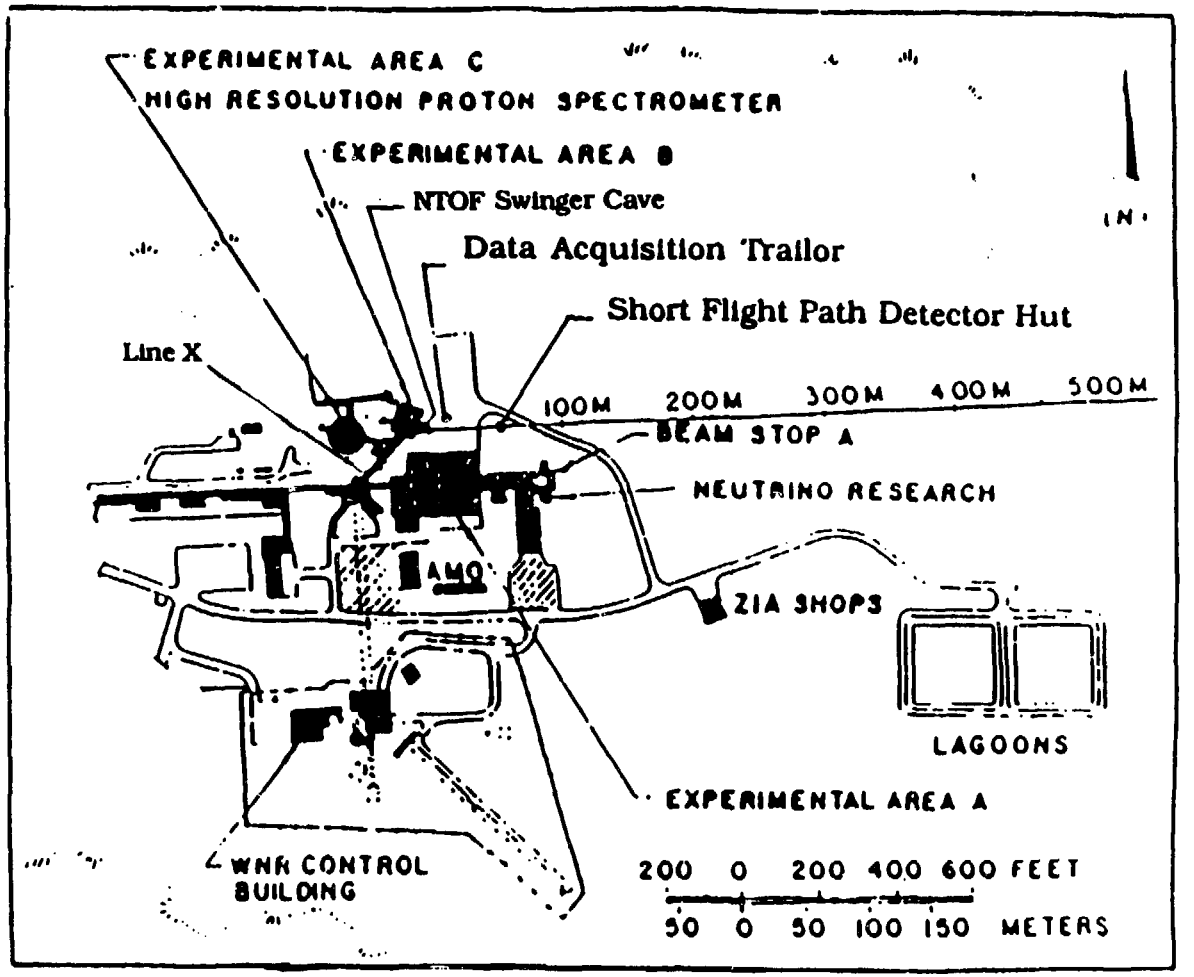

Figure 7 Experimental Area

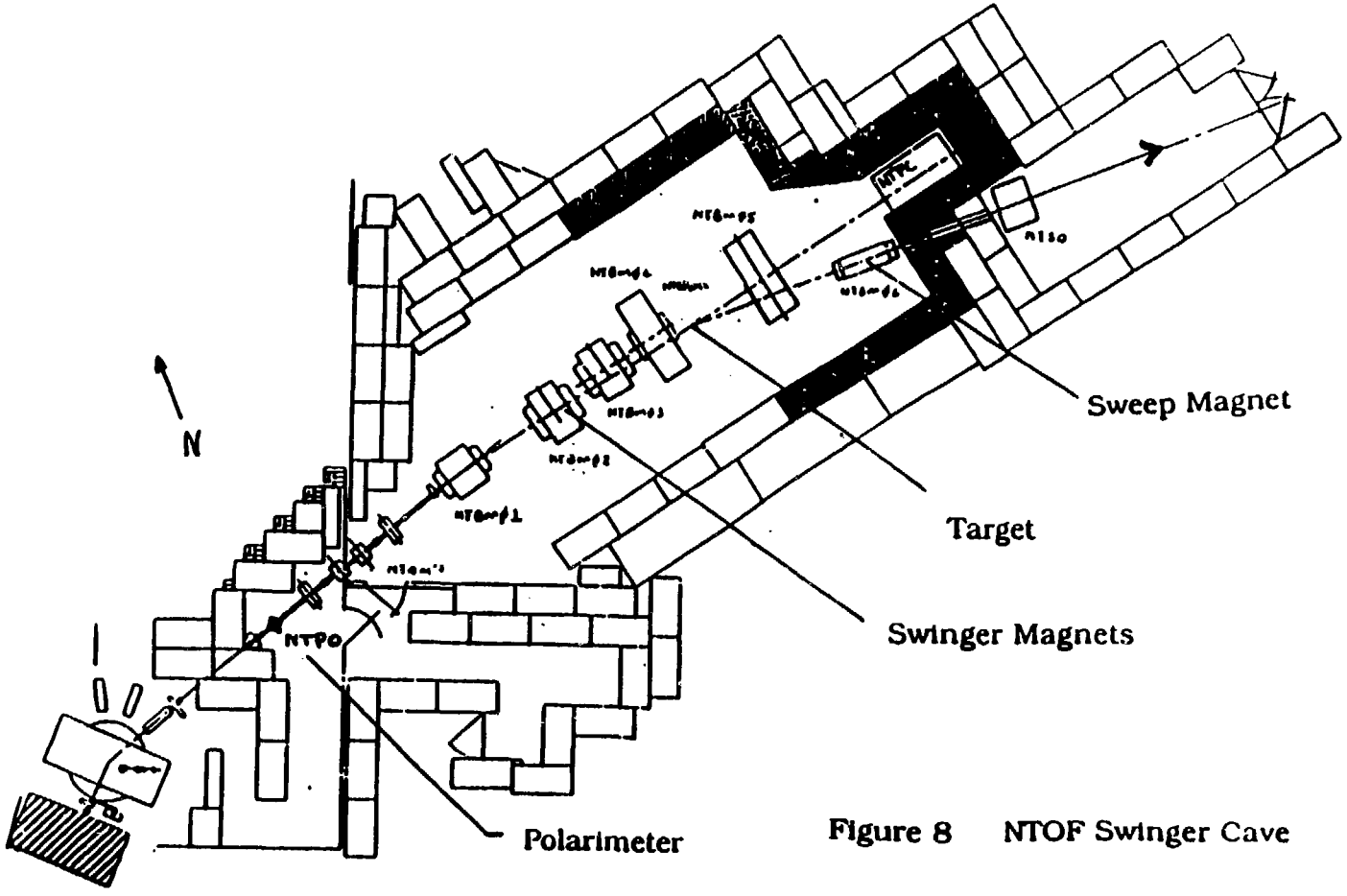

Figure 8 NTOF Swinger Cave

scattering at 500 MeV is known to have a broad maximum near 17°. This maximum extends over the entire energy range available at LAMPF so that the polarimeter geometry has an optimum analyzing power at all energies without being changed. A schematic is shown in Figure 9.

The electronics for the polarimeter were arranged to select good hits and accidental rates from each of the four segments of the polarimeter; left, right, up and down. The timing for the electronics in Figure 9 was arranged as follows. The discriminator outputs were set to 10 ns widths and timed so that detectors 2,3 and 4 lined up to within 1 ns and detector 1 trailed by 3-4 ns. In this way detector 1 determined the timing. The discriminator thresholds on detectors 1 and 2 were set to 200 mV, below the 250-300 mV elastic band pulse heights while the thresholds of detectors 3 and 4 were set to 100 mV, also below the elastic band which spread from 200-350 mV.

The effective analyzing power for NTP0 was set by referencing work done by McNaughton[25] to fully understand beam polarization and polarimeters used at LAMPF. Problems arose when we tried to measure polarizations with NTP0. It was discovered that although the individual forward and conjugate arms had the polarimeter targets within their acceptance, the required 17° and 68° opening angles were not within the acceptance so coincidences were not seen. An error was found in the machining of the NTP0 mounting plates and corrected. However, the corrected plates were not surveyed precisely and the design does not include any direct way for the polarimeter arms to align with the polarimeter target. These factors resulted in a high accidental rate for NTP0 and it was found necessary to adjust the effective analyzing power slightly, (from

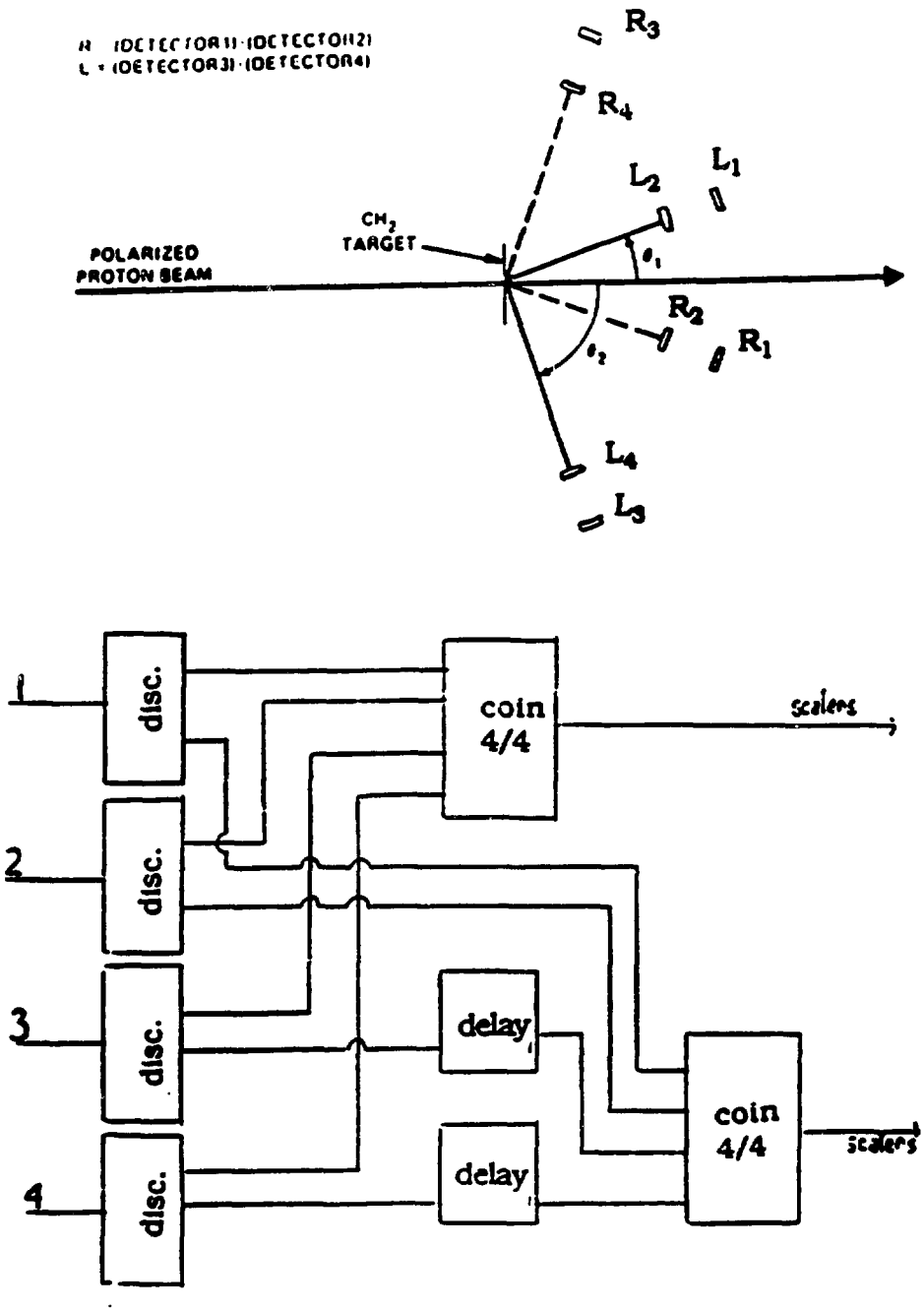

Figure 9 NTP0 layout and electronics logic.

.484 to .479), to obtain polarizations comparable to those from EPP0.

Timing signals from the single left arm of the polarimeter, NTP0, were sent as stops to TDCs and the accelerator RF signal was used as their start. These values were used to generate time profile histograms of the beam. It is possible for some of the beam to slew over into an adjoining bucket and still be accelerated. When this happens, "sidelobes" appear in the beam structure as seen by the monitor's spectrum; that is, small beam bursts before or after the main beam burst appear. This is a problem as the sidelobes have a different arrival time with respect to the RF from the main bucket. It can be corrected by retuning and accommodated in the final results with careful cuts on the arrival times. These profiles were used to track the beam quality, buncher efficiency and for software cuts on the sidelobes of the beam which might be integrated by the SEMs. The width and centroid of the beam profile were also tracked as a means of checking the HER performance. The width is naturally a direct indication of the HER's focusing the beam in time while the centroid monitors if the beam has jumped a bucket or wandered with respect to the RF.

Polarization for the 494 MeV run was read from both NTP0 and EPP0. Signals from each polarimeter were sent to scalers so that raw counts of left scatters, right scatters, up scatters and down scatters were available. Before being sent to scalers, the signals were fanned out. The duplicate signal was delayed 100 ns to put it in the same time frame as the proceeding beam spill. It was then checked for coincidence with signals from the proceeding beam spill of the same arm in a separate coincidence. These accidental counts were also sent to scalers. The accidentals gave us a measure of background hits which in turn, gave us a measure of experimental uncertainty. Accidental

hits contributed less than three percent of the polarization uncertainty.

The calculations used to turn these quantities into polarizations will be discussed in the next chapter.

I C TARGET

The ^{15}N target used in the experiment was ^{15}N-enriched-melamine, $^{12}C_3H_6{}^{15}N_6$. This target was chosen because the higher Q values of the reaction with carbon and hydrogen lowered any observable states to an energy below the region of interest in ^{15}N. Also melamine is a plastic and is easier to handle than a gas target or a liquid target.

The solid plastic target was prepared by hot pressing the powder-like raw melamine into a carbide well mold. This method produced two disks one inch in diameter, 350 mg/cm^2 and 354.6 mg/cm^2 thick. The two disks were mounted face to face to make one target 704.6 mg/cm^2 thick.

It was discovered, nearly too late, that powdered melamine has a shelf life of 4-6 months beyond which it can not be successfully hot press molded. Our target was made near this limit and was delicate in that it tended to crumble. Careful handling of the target prevented any serious loss of material so that this did not impact the experiment. Six month old non-enriched melamine targets pressed at the same time did not have this problem.

The experiment used four targets of interest. They are listed in Table 1.

The energy lost in the target gives another contribution to neutron energy resolution. A proton passing through matter will loose energy through electromagnetic interactions while a

Table 1

Target	Target Thickness
^{7}Li	50 $^{mg}/_{cm^3}$
^{12}C	185.5 $^{mg}/_{cm^3}$
$^{13}C + CH_2$	205.8 $^{mg}/_{cm^3}$
^{14}C	26.5 $^{mg}/_{cm^3}$ + 265. $^{mg}/_{cm^3}$
Melamine	77. $^{mg}/_{cm^3}$
$^{12}C_3H_6{}^{15}N_6$	226.8 $^{mg}/_{cm^3}$

neutron will not. As there is no way of knowing where in the target the (p,n) reaction takes place, the amount of material passed through before the interaction and hence the final energy of the particle as the interaction is made can change from zero to the full energy loss possible when the proton interacts at the back of the target. This energy resolution contribution is given by:

$$\Delta t_{TGT} = \frac{\Delta x}{c}\left(\frac{\beta_p - \beta_n}{\beta_p \beta_n}\right) \quad . \qquad (10)$$

Here, Δx is the target thickness and $\beta_p(\beta_n)$ is the mean proton (neutron) velocity divided by the speed of light.

I D CURRENT MONITOR

One SEM was placed upstream of the target to monitor the beam current. The monitor detects charged particles passing through it. The signals from the SEM were sent to a charge integrator which sent pulses to the scalers. The other current monitor was the ion chamber placed downstream of the target. The ion chamber detects the ionized trail left by the beam passing through and sends a signal to a charge integrator whose output is sent to scalers. The scalers were gated by (RUN.N.P) and (RUN.R.P), that is, polarized beam present and a data acquisition run in progress. This current monitor was used as a relative monitor of beam current. Absolute counting was not needed due to the normalization discussed in the next chapter. This SEM, NTER02, was also used to check the new Faraday cup, NTFC, in the beam stop. NTFC actually consisted of a mass of graphite electrically insulated forming the beam stop for protons and connected to a charge integrator. The charge

integrator showed a current leak so that the information from NTFC was disregarded.

I E FLIGHT PATH

A temporary short flight path was used for this experiment while the long, permanent NTOF flight path was still under construction. It consisted of approximately 52 cm of vacuum chamber and an open air flight path of 80.72 meters for production angles equal to or greater than 11°. For angles less than 11°, an additional vacuum chamber .5 meters long was inserted adjacent to the scattering chamber to keep the proton beam from interacting with the air and confusing the readings as another source of neutrons. The flight path terminated in a concrete block house built for this experiment. With this 82 m flight path, the 6.2 MeV separation between the $^{15}N(p,n)^{15}O$ ground state and first excited state transitions along with usage of the HER achieved adequate resolution for the desired measurements. The concrete of the block house allowed construction to continue during data taking.

As in the beam transport to the target, the drifting of the neutron to the detector also causes a spread in timing resolution. A 1 MeV energy spread of a beam with a mean energy of 500 MeV over an 82 meter flight path results in a time spread of .19 ns. This is given by:

$$\Delta t = \frac{c}{l}\left(\frac{T+.5+m_0c^2}{\sqrt{(T+.5)^2+2m_0c^2(T-.5)}} - \frac{T-.5+m_0c^2}{\sqrt{(T-.5)^2+2m_0c^2(T-.5)}}\right) \quad (11)$$

where l is the flight path length, m_0 is the neutron rest mass and T is the mean beam energy. This was corrected for by the HER.

The open air flight path presents additional problems. The neutrons traveling along the flight path must pass though air with an average pressure of 585 torr at Los Alamos altitudes and at 20 degrees centigrade. The mass attenuation coefficient for air is;

$$\mu = \Sigma \mu_i = n \sigma , \qquad (12)$$

where n is the nucleus population accounting for atmospheric considerations and σ is the weighted average of the species cross sections at the energy desired, calculations show that air accounts for an overall average attenuation of the neutrons by approximately 10%. This fluctuates throughout the day with the temperature and weather conditions and of course, there is the added matter of precipitation.

At the time of the measurements, nothing had yet been implemented to measure the effects of precipitation during data acquisition, but this needs only be considered for measurements where attenuation cannot vary more than 1%. Calculations show that a 1" per hour rain fall contributes approximately only 43 mg/cm^2 of water to the flight path. This mass is less than half the thickness of the nitrogen in the melamine of the target in the beam line.

None of the effects of the open-air flight path were explicitly measured for this experiment. These effects were cross normalized out with ^7Li yield measurements. ^7Li data acquisition runs were taken along with every ^{15}N run, providing normalization as discussed in Chapter 3, section II D. The effects of pressure affected the ^7Li as it did the ^{15}N and were normalized out. As no cyclic fluctuations between beam on target and yield at the detector were seen on the order of one day nor between data taken at the beginning of the run and that

taken at a nearby angle at the end of the run, we believe this technique to be reliable.

I F DETECTORS

The detectors consist of three tanks of liquid scintillator acting as neutron detectors and two planes of thin plastic scintillator acting as charged particle tags as shown in Figure 10. In this experiment, they subtended .67 +/- .004 degrees of the angular distribution at each data point taken.

A particle entering the detector system first encounters the charged particle detector paddles. These five paddles constitute a single plane of plastic scintillator. The three horizontal paddles, numbered 0, 1, 2, top to bottom on the array and +/- beam left/right, measure 15.75" x 41" and are .22" thick. The light guides are adiabatic and are attached to "homogenizing" bars which are attached to the scintillator. This combination insures prompt timing for the particle although some vertical position information is lost for the sake of good mean timing. The two vertical paddles, 51.5" x 3.94" and .12" thick, number 3, 4 beam left/right and +/- on the top/bottom, were made to cover the edges of the tanks not quite covered by the horizontal paddles. Adiabatic light guides were not used because of the paddles' narrow width.

The tanks are 1.05 m x 1.05 m x 10 cm stainless steel tanks divided into 10, 1.05 m x 10 cm x 10 cm cells. The tanks are lined by isolators made of black paper sandwiched between lucite plates. These isolators also separate the individual cells and optically isolated them. Signals are taken from each end of each cell with an Amperex XP2262 photomultiplier tube (PMT) and a CERN base. Each cell gives a position resolution of < 5 cm

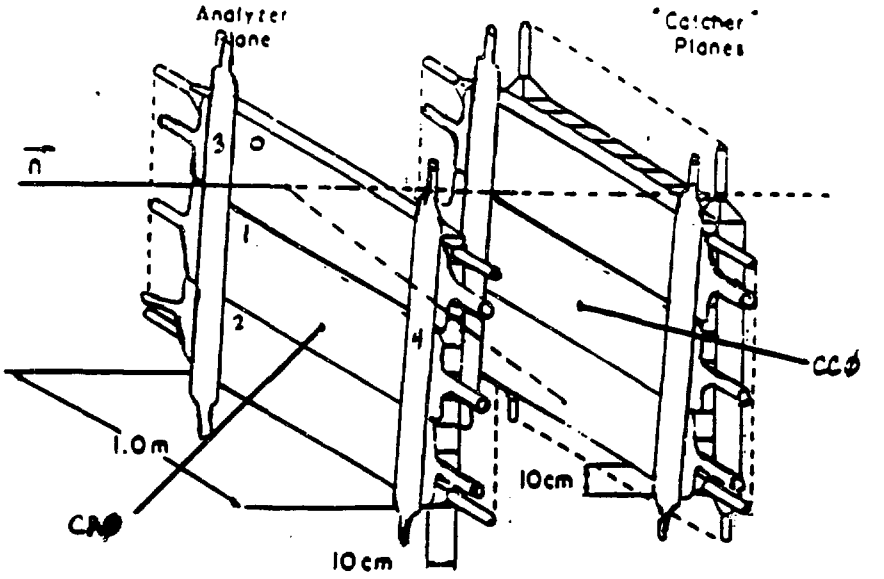

NTOF Detector array showing CPVs.

1.7m

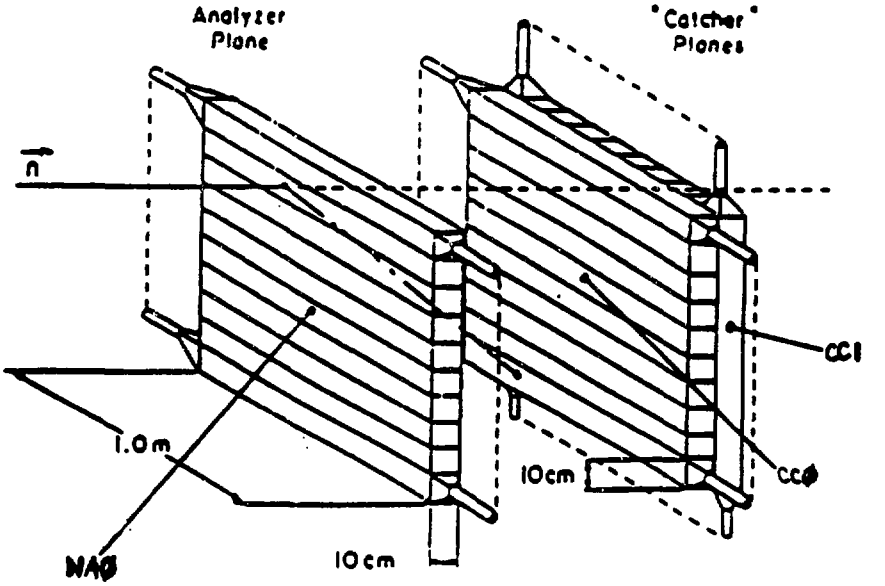

NTOF Detector array with CPVs removed.

1.7m

Figure 10

along its length as measured by a NTOF development run. Position in the other dimension is taken by cell number.

The liquid scintillator used was Bicron-517S. It is a mineral oil based scintillator with an H:C ratio of 1.7:1 and a density of 0.86 gm/cm^3 and an attenuation length of >5 meters. By varying the amount of scintillating material in the mineral oil, it is possible to vary the light output for this type of liquid scintillator at the expense of the H:C ratio. The batch used at NTOF gives 65% of the light output of anthracene. This was chosen because this blend optimized the light output and the H:C ratio. The large H:C ratio is desirable to maximize the probability of events between incoming neutrons and hydrogen rather than carbon.

To avoid contamination of the scintillator by oxygen, dry nitrogen gas is constantly bubbled through the detector's expansion tank. Long term effects of the scintillator on the tank, isolators, and light guides are still being studied. Discoloration of one batch of scintillator occurred to one tank of scintillator stored in the tank over winter of 1986-87. No change in detector response has been noted thus far.

One undesirable side effect of the liquid scintillator in the tank was that the pressure from the liquid caused the walls of the tank to bow out. To combat the problem, nine small metal straps were welded inside the tank from wall to wall along the center isolator. The straps in NA0 broke their anchoring weld when the tank was over-pressured with N_2 during filling and are still in the tank but causing no noticeable loss of efficiency. Steel bars are now clamped around the outside of the tank which controls the bowing but does not eliminate it. Studies have not been done to check the exact effects of these bars on efficiency though no large effects have been noted.

At the time of construction, solid scintillator could not be produced in 10 cm thickness with an attenuation length

approaching that of liquid scintillator. Bicron 517S was less expensive and has an attenuation length of greater than five meters. As solid scintillator attenuation lengths are improving and the cost of the support system for the liquid brings it to he range of the cost of solid scintillators, that reasoning may no longer hold.

The tank is segmented into 10 cells to divide the instantaneous rate among 10 PMT pairs. Studies done at EPB for NTOF development in November, 1986, have shown that individual cell ends (or individual CP ends) should not be run at an average rate of greater than 1 kHz for this beam bunch spacing.

The optical isolator panels are made of black paper sandwiched in between two layers of .0625" thick lucite. These 10 cm x 1 m panels slide into the tank through the end. The black paper is layered between the sheets of lucite which are then bonded together at the edges. Glue is not applied to the paper so that it is not wetted. Wetting the paper destroys the total internal optical reflection of the paper at the interface.

Black paper was chosen over white paper because the black paper allows only total internal optical reflection while white paper provides absorption and reemission. Total internal reflection limits the angles accepted and thus the optical path length variation in the detector. For absorption and reemission, light is reemitted in all directions. More total light can thus be collected with white paper, but the pulse carrying this information has a generally softer leading edge and can extend for more than 100 ns. Black paper was used at NTOF because prompt timing was the most important consideration, as the energy of the incoming particles is derived from the time of flight.

The light guide design is critical. After extensive testing and computer simulation by Reese and Carey[26], it was decided that the light guides be of the non-imaging type angled to pass only light reflected three or less times. The light as it arrives is not focused to a point but is spread to illuminate the full face of the PMT.

The PMTs used at NTOF, Amperex XP2262, have a time delay difference for photons hitting the center of the PMT and photons hitting the edge of 700 ps. This difference is due to the path length difference that the liberated electrons follow while forming the pulse. By illuminating the full face of the PMT, the contribution of the PMT to the time resolution is reduced to that due to fluctuations in the average arrival time. This resolution has been measured to be 275 ps by placing two PMTs face to face with a thin scintillator between them. A source was placed alongside the scintillator which was strong enough to 'illuminate' the whole scintillator. A time spectrum was taken by using the anode signal of one PMT to generate a start pulse and an anode signal from the other PTM to generate a stop pulse such that the width of the time spectrum measured the uncertainty of the arrival time of the photon due to propagation along the tube.

Allowing light pulses which have been reflected up to three times, adds to the total light detected and the reflected pulses contribute to the output pulse as shown below. The more often the light is reflected, the later and broader the peak. These reflections thus contribute primarily to the tail of the pulse.

The reaction mechanisms for neutrons in the liquid scintillator are many and varied. Kellogg[27] has given 65 separate neutron-induced carbon breakup channels and their cross sections for 90 MeV neutrons via cloud chamber experiments. As the neutron energy increases to the 200-500 MeV range, yet more channels open. In computer codes which try to simulate

the detector response, the interactions are limited to the set discussed below.

Experiment has shown that at low energies, the n+p elastic reaction is dominant but as energy rises, the carbon channels become more important. A recoiling carbon nucleus will give off less detectable light so that the problem cannot be simplified. Most energy is deposited at the end of the recoil particles' paths, but as a neutron can interact anywhere in the volume this energy is not always detected. This serves to further mask reaction mechanisms. Even with these difficulties, Sailor, Byrd and Yariv have come within 10% of predicting the efficiencies of the NTOF detectors with a Monte Carlo code called TRACE[28].

The main reaction mechanisms are forward peaked, thus there exists a thin region at the back of the detector where, if the neutron interacts in this region, the path of the recoil is not long enough to generate sufficient light to cross the threshold of the discriminators set on the detector anode signal. As our discriminator thresholds were typically set to 50 mV, this region was on the order of 6 mm deep and effectively lost to the detectors.

The detector system is designed as a neutron polarimeter with the front plane an active "analyzer". The back two tanks are the catcher planes. The catcher plane is separated into two planes to achieve the required timing resolution while maintaining a suitable efficiency. For this experiment, the polarization of the outgoing neutrons was not measured. However, due to the background from "wrap-around" neutrons, i.e., slow neutrons from a previous micropulse which enter the detectors simultaneously with the neutrons of interest, data were taken in coincidence mode and the time of flight measured between planes as well as along the flight path. By measuring these times over known distances, the velocity of the particle

was calculated and the slower wrap-around neutrons removed from analysis by the software. Where wrap-around neutrons are not a significant factor, all planes can be used to measure the incoming flux of neutrons.

The detector thickness contributes to the timing resolution because we are not sensitive to where within the thickness of the detector the neutron interacts. These timing resolution contributions are given by:

$$\Delta t_D^2 = \Delta t_d^2 + (\frac{\Delta D}{\beta_n c})^2. \qquad (13)$$

Here, Δt_d is the intrinsic time resolution of the detector and ΔD is the detector thickness.

Timing fluctuations within the cables and electronics were measured and found to contribute a negligible 30 ps. The intrinsic resolution of the detectors includes the PMT uncertainty and the cable and electronics uncertainty. These contributions fold together to yield typically 350 ps overall.

I G COMBINED ENERGY RESOLUTION

All of the contributions to the resolution can be brought together to give an estimate for the expected resolution of the system. This is useful in determining the needed target thickness and flight path needed to separate states of interest and still achieve an acceptable estimated rate of data acquisition. This expression given in terms of energy is[29]:

$$\Delta E_x^2 = \left\{\left[\left(\frac{P_n}{P_p}\right)^3\left(\frac{M_p}{M_n}\right)^2\frac{I_p}{I_n}\left(1-\frac{\gamma_p^2\partial I}{I_p\partial\delta}\right)\right]^2+1\right\}\Delta E_o^2$$
$$+\Delta E_{TGT}^2+\left(\frac{P_n}{P_p}\right)^3\left(\frac{M_p}{M_n}\right)^2\frac{I_p}{I_n}\left[\Delta t_I^2+\Delta t_o^2+\right.$$
$$\left.\Delta t_d^2+\frac{\Delta x}{c}\left(\frac{\beta_p-\beta_n}{\beta_p\beta_n}\right)^2+\left(\frac{\Delta D}{\beta_n c}\right)^2\right]. \qquad (14)$$

where Δt_o is the intrinsic time resolution of the beam coming out of the LAM, $\Delta t_I = \Delta t_{path}$ where $\alpha_i \neq \delta$, ΔE_{TGT} is the energy a proton looses passing through the target and γ_p is derived from β_p.

I H ELECTRONICS

The electronics hardware determines when a valid event occurs in the detectors or related monitoring systems and allows the data of the event to be recorded by the computer. The electronics recognizes valid events of six general trigger types: monitor, cosmic, neutral-neutral, neutral-charged particle, charged particle-charged particle, and neutral single.

We start by examining the logic for each plane of the system which determines if a valid event occurred in that plane, and the monitor logic which determines if a valid event occurred in the beam monitor. The trigger logic takes the information from the plane and monitor logic and determines the type of trigger and starts the digitization of the data. The FERA and CAMAC subsystems used to read the data into the NTOF uVAX will then be considered.

I H 1 PLANE LOGIC

The Plane Logic is shown in Figure 11. The pulse from the PMT of a neutron cell is fed to a power splitter. One of the splitter outputs is sent through a 10 db attenuation and a 220 ns delay to an Analog to Digital Converter (ADC). The delay assures that the signal arrives at the ADC input only after an event has been previously triggered and the attenuation keeps the pulse height to within the range of the ADC. The other signal from the splitter is used for initiating an event for the corresponding plane. This signal is sent to a Constant Fraction Discriminator (CFD Ortec 934), which was chosen over a leading edge discriminator (LED) to improve timing characteristics. The CFD splits the signal, inverts and delays one half and adds it to the first half which has been attenuated. The resulting bipolar signal's zero crossover is nearly independent of the amplitude of the incoming signal. This insures that the module is fired at the same relative time for all input signals.

The thresholds of these CFDs were set to 50 mV. One output was delayed 220 ns and sent to the Time to Digital Converters (TDCs) as the stop for that cell end. Another CFD output was sent to a mean timer (MT) along with the CFD output from the other end of that cell. The mean timer puts out a NIM pulse at the mean time of the two cell end times (plus a fixed delay). The output of the MTs of the cells of a plane are fanned into a logical OR. A single hit from a cell allows this OR to send a signal to the plane's logical coincidence unit which checks for coincidence between this OR, a "not present" signal from the cosmic logic and no veto by the CPV. This determines a hit for the trigger logic.

Special linear outputs from the MTs of all of the cells in a plane are summed by a linear fan-in. The outputs of the fan-in

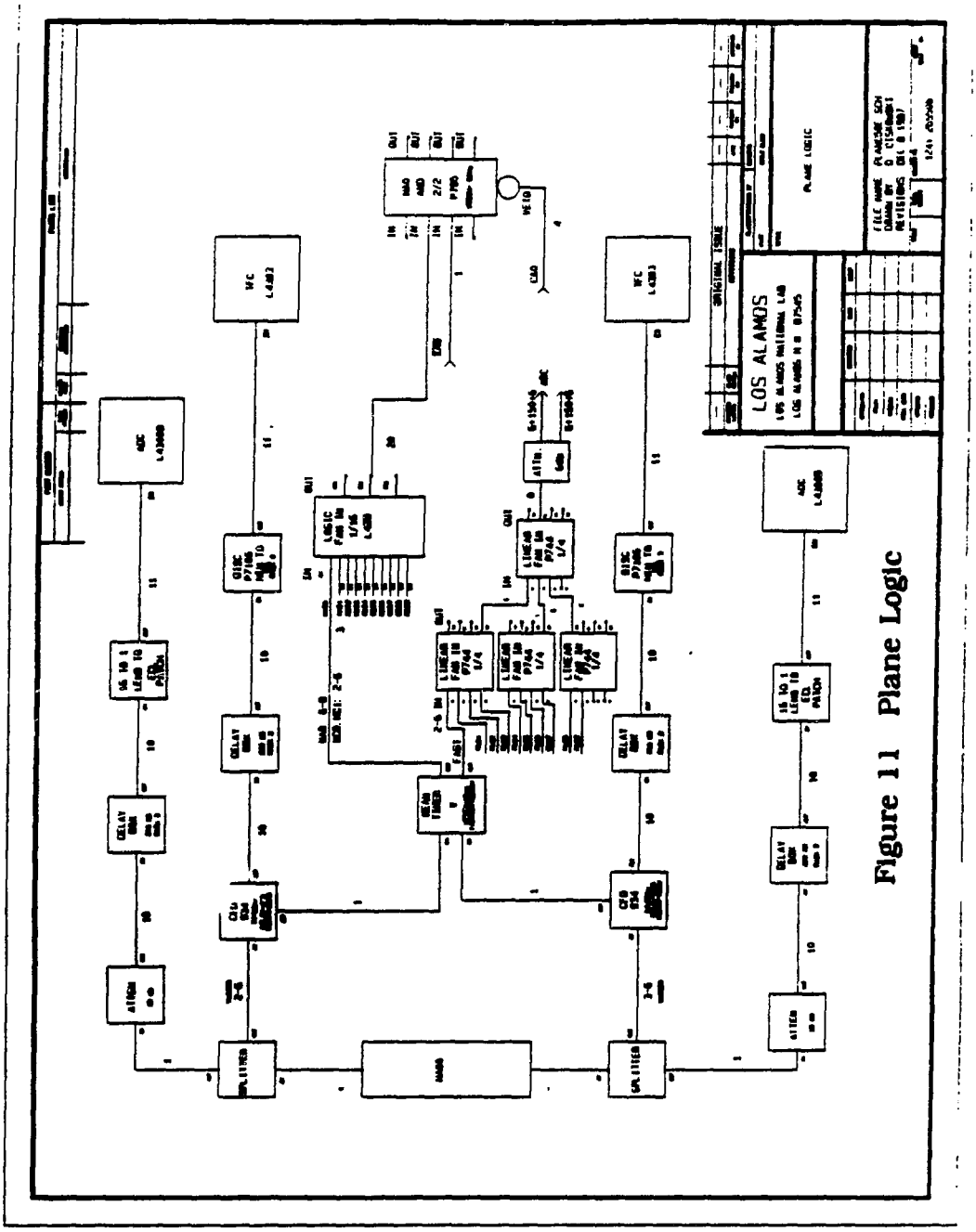

Figure 11 Plane Logic

are attenuated by 6 db and sent to an ADC as a multiplicity measure.

I H 2 COSMIC LOGIC AND MONITOR EVENTS

A cosmic event trigger (KOS) is defined as the top and bottom cells of a plane (or the left most and right most in the vertical tank,) both firing. It assumes an event is caused by a cosmic ray traversing the whole tank and allows us to interpolate a cosmic ray path which will pass through every cell. This is useful in that it allows us to check cell efficiencies and position resolution along the cosmic track continuously during data taking. Firing of this trigger is conditioned by vetoing cosmic events which coincide with the plane's charge particle veto plane firing. This eliminates showers entering from the side of the tank.

Cosmic tracks were used to set and check relative timing offsets. Cosmic data was taken between all beam pulses as a running calibration check. The logic diagram for Cosmic events is shown in Figure 12.

A monitor event (MON) is defined as an event from a single arm of the polarimeter as shown in the logic diagram in Figure 9. By referencing its time to that of the RF TDC stop, we were able to make a beam time profile. This allowed us to track the beam drifting with respect to the RF and drifting with respect to the HER which would degrade the resolution. A typical monitor spectrum is shown in Figure 13.

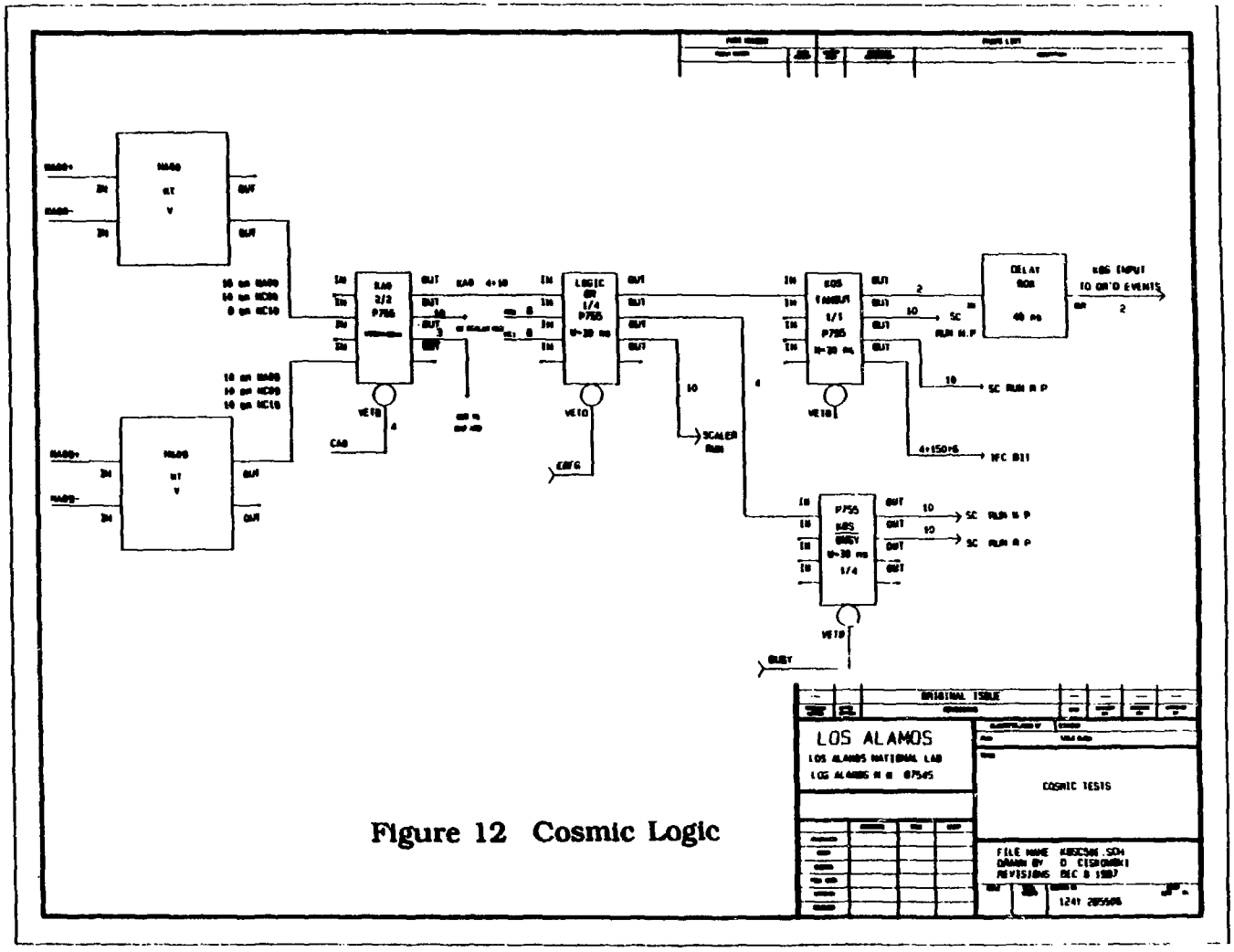

Figure 12 Cosmic Logic

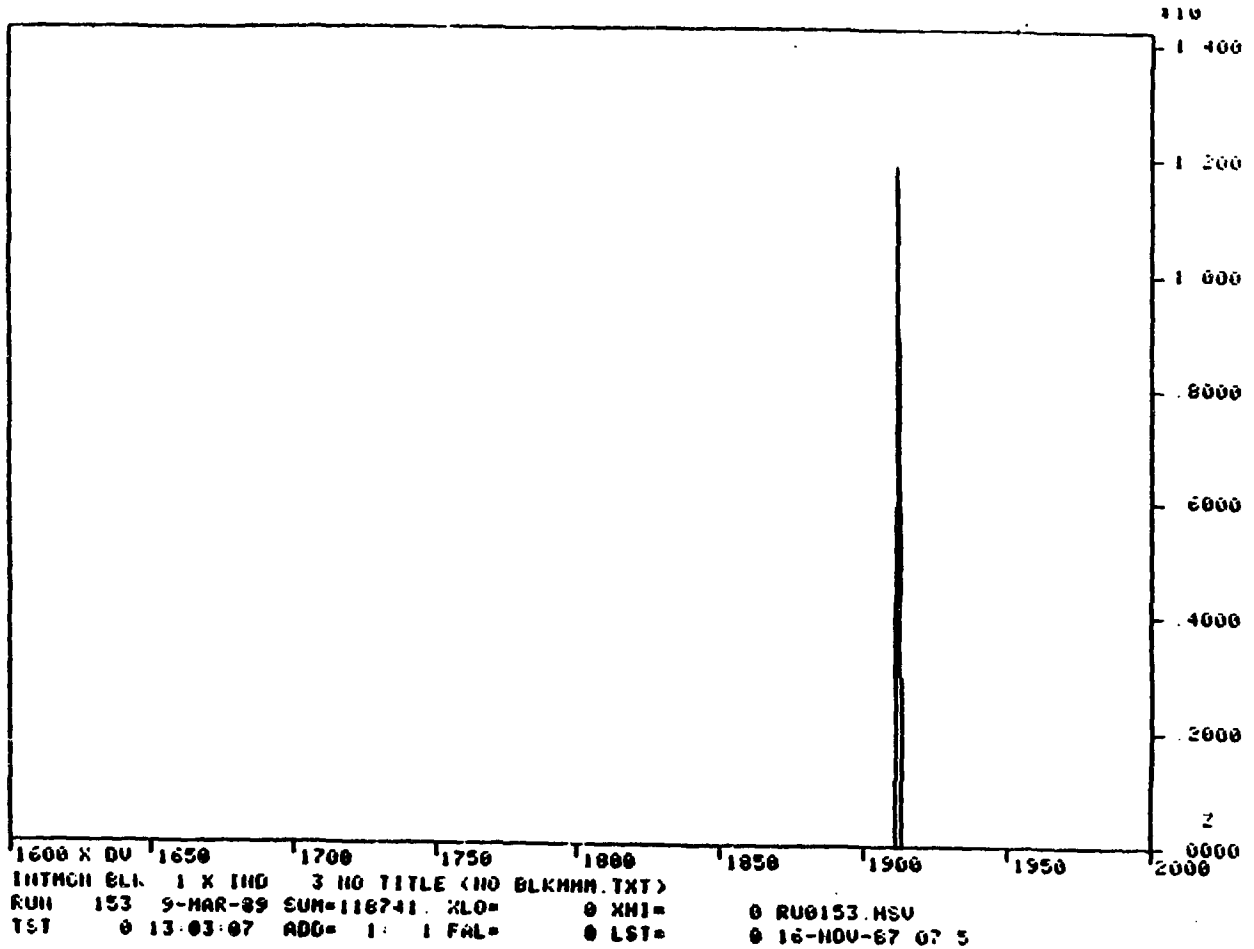

Figure 13 NTP0 Monitor Spectrum.

I H 3 TRIGGER LOGIC

The logic used to determine the trigger is shown in Figure 14. The logical coincidence units from each plane's individual logic are shown at the left of the figure. These three logic paths come together to form three types of trigger. First, the back two planes NC0 and NC1, are "OR"ed together to show a hit in the "catcher". NC0 and NC1 are again ORed together, in parallel to the first OR, but first passing through gates formed by a charged particle veto, CC0, placed upstream of the planes. This tags the event as a neutral in the catcher, the "gated by CC0" arm, or a charged particle in the catcher, the "ungated" arm. The neutron singles OR, NSING, is formed by an OR of an NA0 hit, gated by CA0, and a gated catcher hit. This OR , vetoed by BEAM*,(not BEAM), was rate divided by 50 to keep the singles events from dominating the acquisition system. It was then fanned together with the RF, the KOS signal from the cosmic logic and the signal from the monitor event. Neutral-Neutral coincidences, NN, were defined by ANDing the NA0 hit with a gated back plane hit. Neutral-Proton events, NP, where neutrons were converted to charged particles in the front plane and the charged particle detected in the back plane, were defined as an "AND"ed NA0 hit and an ungated hit in the back plane. CA0, the charged particle veto for the first plane, though it is used to veto each charged particle entering NA0 from causing a trigger, also anded with CC0 to form the "Charged particle-Charged particle", (PP) trigger. The PP trigger was put through a prescaler set to a factor of 1. The PP trigger, though useful in seeing the gamma flash from the target when pair production occurs from the gammas in or just before the analyzing plane CPV, was included should such events become noteworthy in the future and was used in this experiment only when the gamma flash could not be

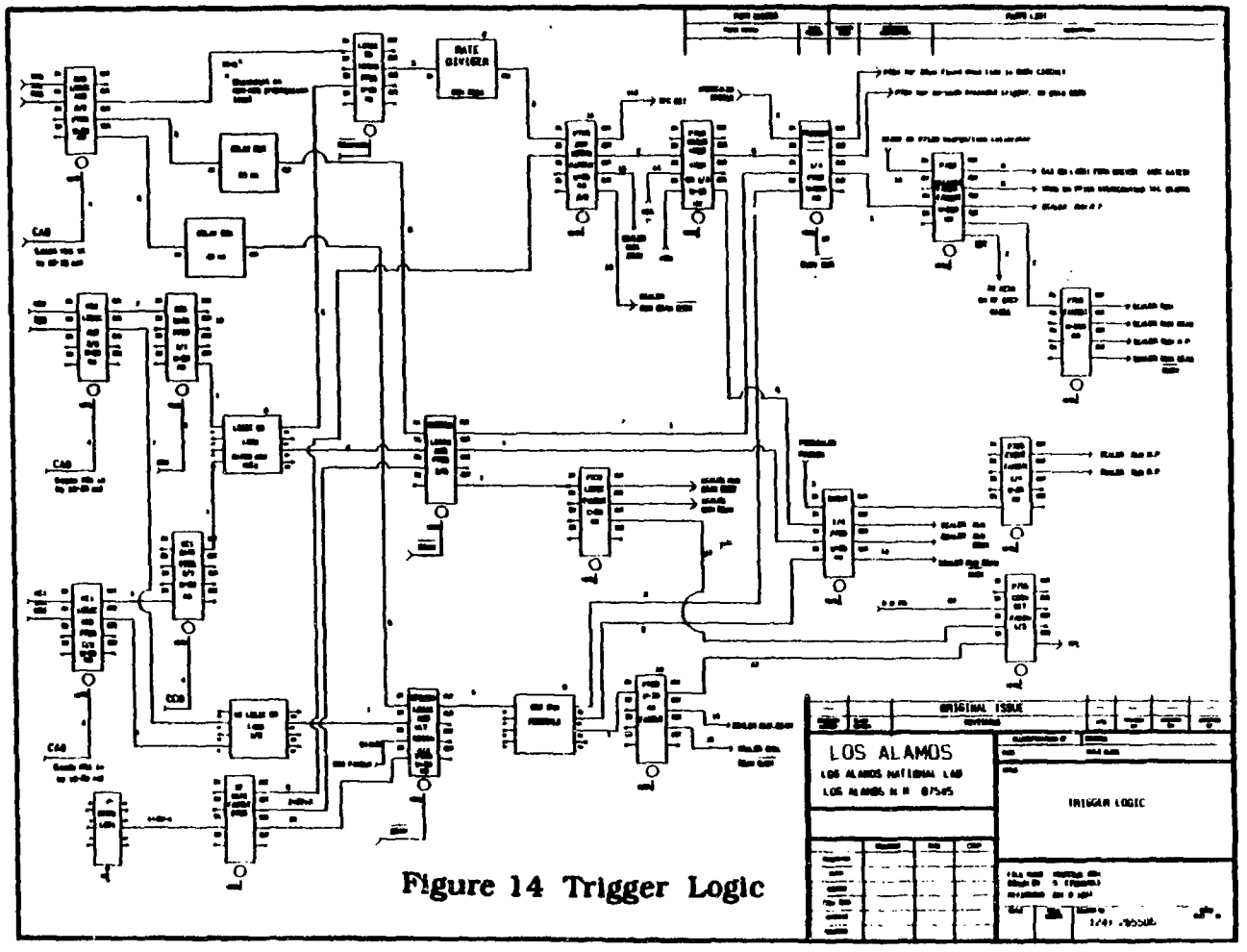

Figure 14 Trigger Logic

seen in other triggers. The prescaler is present in case the fraction of these events of the total become too large so as to detract time from observing other event types.

The (NSING+MON+KOS+RF) are fanned together with the NN, PP and NP events twice in parallel. Towards the top of Figure 14, we see the first fan-in generates the "TRIGGER", which is vetoed by (BUSY.RUN*). It is fanned out to the busy circuit and provides the FERA driver gate, ADC gates, TDC starts and certain scaler inputs for dead-time monitoring. The lower arm of the parallel fan-in shows the fan-in defining "EVENT". It is then fanned out to scalers. Ideally, these two uses would be in series,(TRIGGER = EVENT.RUN.BUSY*), but at NTOF it was done in parallel to shorten the time to the "TRIGGER". This was necessary as otherwise some neutron detector TDC stops were coming too close in time to the starts.

Another important section included in the trigger electronics is the RF gate. This 20 ns wide gate is derived from the RF and used to condition the trigger. As the detected particles are phase locked to the RF within this range, it restricts the range of times accepted into the time spectra. This insures that minimal computer time is spent on events outside the region of primary interest.

The timing of the trigger is arbitrarily chosen to be determined by NA0. It is desirable to have one element determine the timing because of various hardware considerations. NA0 was chosen as the element used to determine the timing as it is present in all trigger types of the detector array except for KOS and NSING from the back plane.

Timing to all coincidences was checked by feeding a fanned out pulser signal into the CFDs of the plane logic for all planes. All delay was kept as short as possible to improve livetime while all signals were timed together. All neutron plane logic widths

were set to 50 ns. NA0 was delayed by 40 ns. This allows for a 10 ns overlap between NA0 and the catcher plane signals in the case of 800 MeV particles going straight (having the shortest propagation time) through the system and up to 40 ns coincidences for the 50 MeV particles going from one corner, diagonally to the farthest corner, (the longest interplane propagation time). This worked the same for the NP trigger as the CC0 discriminator was set to a 60 ns width and timed to overlap the catcher plane with +/- 5 ns on each end. CA0 is set to a 60 ns width and starts along with NA0, thus it overlaps CC0 by 15-45 ns in the PP trigger. Similarly, the NA0 input to the NSING trigger was delayed to coincide with the gated (NC0+NC1) signal. By triggering NSING with a cosmic event, the KOS trigger was timed to coincide with the NSING at the OR'ed EVENT fan-in. Having all triggers start at the same relative time guarantees that time spectra will populate the same TDC ranges for all events, and thus removes one possible source of systematic bias between event types.

I H 4 SLOW LOGIC AND BUSY LOGIC

The spin orientation of the beam which was in effect when an event occurred was determined by the slow logic. The slow logic, so named because it involves timing changes on the order of microseconds or greater, is shown in Figure 15. It takes the logic levels provided from the ion source and sets data words recorded for each event. It also provides gating for the scalers. Signals from the accelerator for RUN GATE, NORMAL SPIN (N), REVERSE SPIN (R), POLARIZED BEAM (P) and QUENCHED BEAM (Q) start on the left of Figure 15 and are converted from TTL to NIM. N, R, P, and Q are then "AND"ed together with

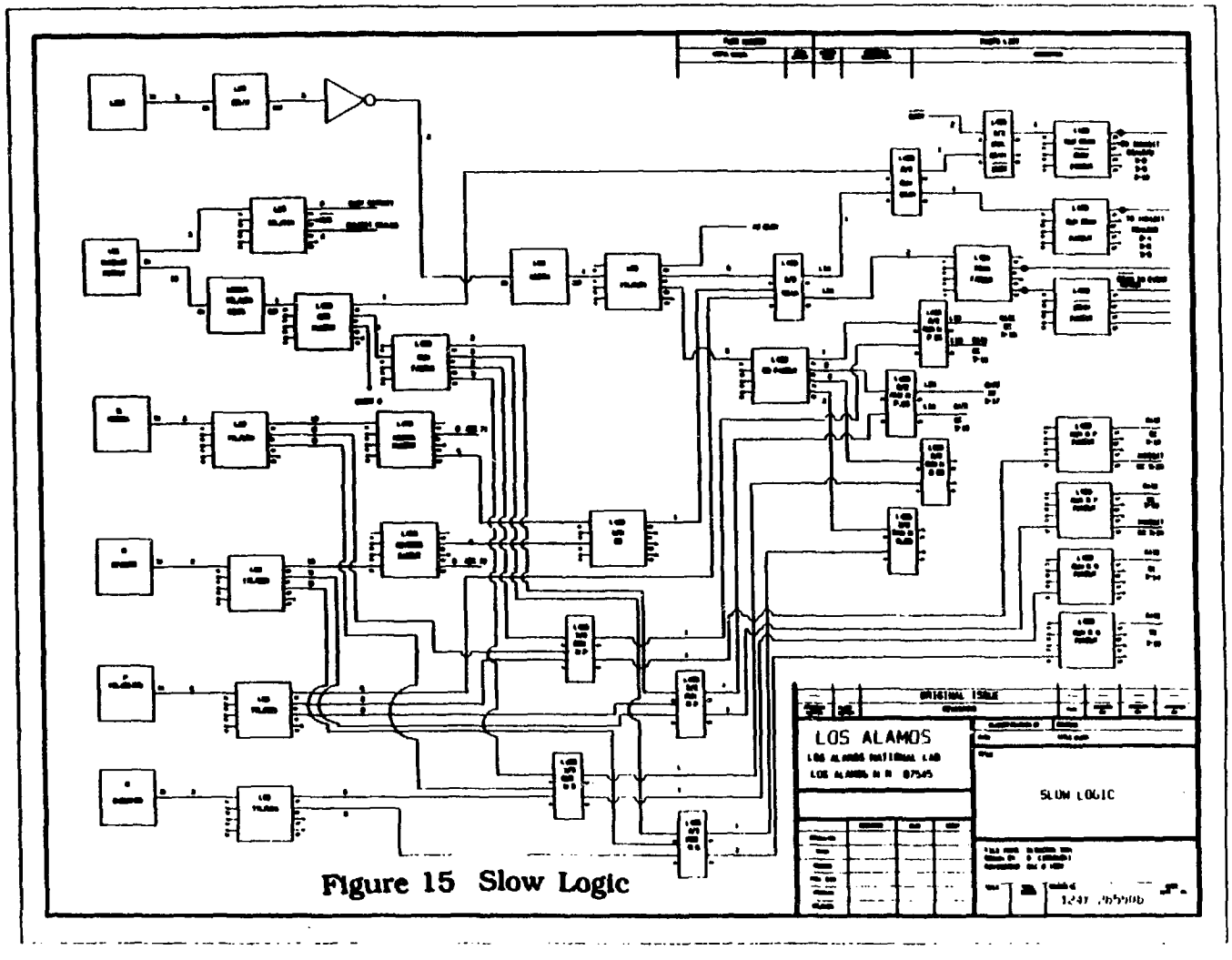

Figure 15 Slow Logic

RUN GATE (RUN) and BEAM GATE (BG) as N.P.RUN, R.P.RUN, N.Q.RUN, R.Q.RUN, and N.P.BG, R.P.BG, N.Q.BG, R.Q.BG. These signals are then fanned out to gate scalers. N.Q.BG and R.Q.BG were not used due to a lack of scalars. BEAM GATE and N OR R, (N+R), are "AND"ed to make BEAM. BEAM becomes BEAM* and is used for event vetos.

The busy logic, shown in Figure 16, is the circuit which disables the trigger when the system is not ready to accept data. One output of the TRIGGER is sent to the busy logic. It is fed to a LeCroy 794 delay and gate generator which generates a 20 μs fixed dead time for each trigger to allow sufficient time for FERA (see below) to finish reading in and prepare for more data. This is combined with the ADC readout request of the FERA driver (showing that the ADCs are busy), a level from an output register indicating the buffer memory is being read out, the memory overflow and RUN*. It forms the BUSY which is then sent to the TRIGGER veto and to form RUN.BEAM.BUSY* and the KOS.BUSY*.

I H 5 CAMAC AND FERA

The data was read into a μVaxII computer using the Computer Automated Measurement And Control[30] (CAMAC) system and the LeCroy Fast Encoding and Readout ADC (FERA) system. The FERA system takes time signals and pulse height signals and digitizes them for input into the computer[31]. To prevent a large dead time with each event, FERA writes the data in a buffer memory via a high speed path independent of CAMAC until the end of the macropulse.

FERA digitizes timing signals much as it does pulse height signals. To do this, it employs a Time to FERA Converter (TFC).

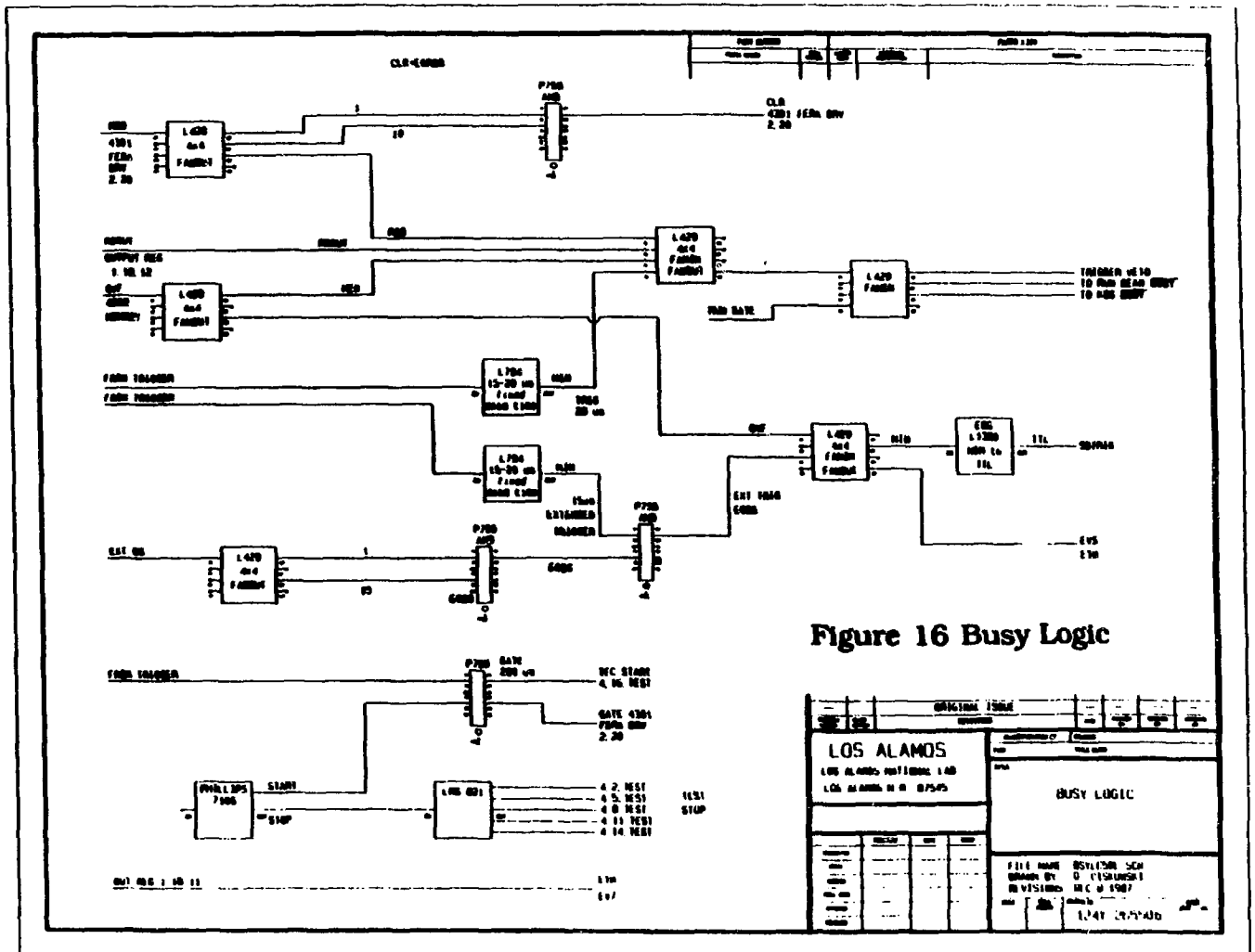

Figure 16 Busy Logic

The TFC turns on a constant current source for each channel when it receives a common start. The source for a given channel is turned off when that channel receives a separate stop, the module receives a common stop, or the channel "times out" i.e. a certain maximum time limit has expired. The currents from these modules are sent to FERA ADCs for digitization and readout.

The ADCs integrate and digitize the current in the same manner as for a PMT pulse height signal. Both time digitized and pulse height digitized data are sent to the FERA buffer. Data waits in the FERA buffer until it receives a signal denoting the end of beam gate or the buffer is full. It then is read by a Micro-programmable Branch Driver (MBD)[32] which acts as a buffer between the CAMAC and the computer. The MBD then sends its data to the μVAX.

The FERA data flow and wiring diagram are shown in Figures 17 and 18.

II NTOF SOFTWARE

II A ANALYSIS SOFTWARE

The data acquisition programs were all run under the LAMPF data acquisition system know as the Q system. The Q system issues commands to the data acquisition hardware, stores experimental parameters, runs the histogramming system and test package, and writes the data to tape. It is the standard data acquisition system used at NTOF, supported by LAMPF, and allows each experimenter to customize software to its own needs by writing its own analyzer.

FERA Data Flow

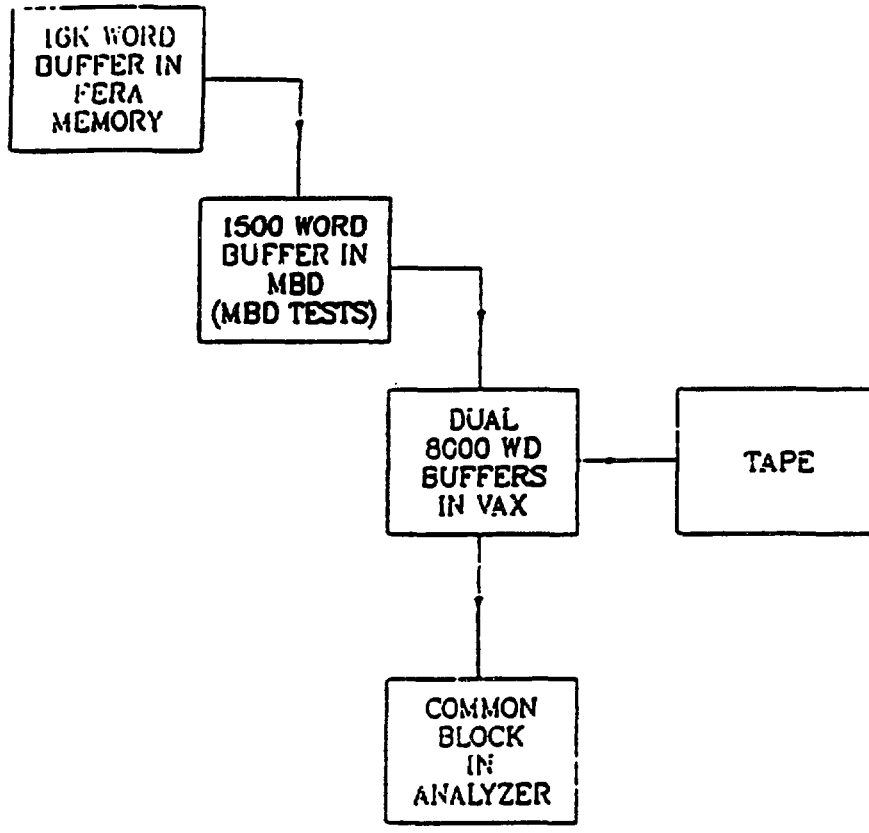

Figure 17

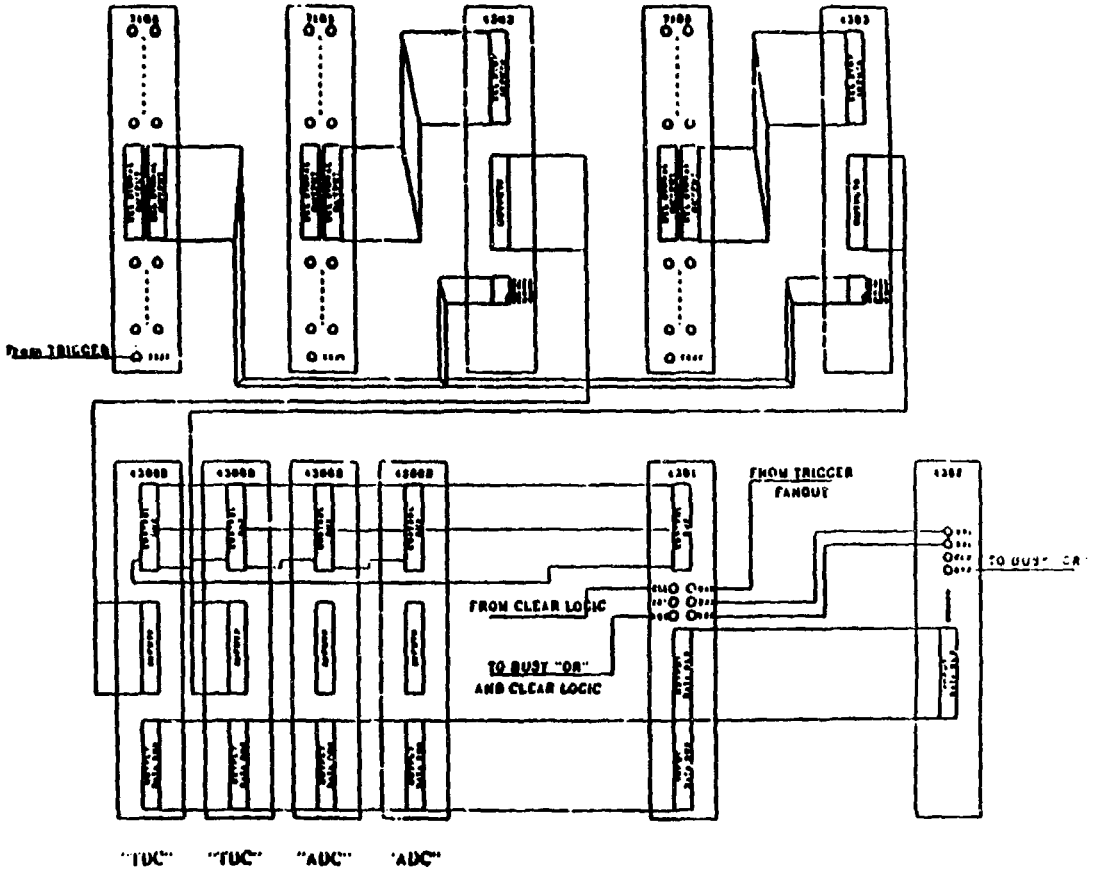

Figure 18 FERA Input Wiring Diagram

The program which processed the events, the analyzer, was used both during data acquisition and during final analysis. The program first read in the beam pulse position in time with respect to the RF, from the beam monitor for any MON trigger. Any significant drift in this time would then be offset by a corresponding shift in the absolute time.

The pulse heights of the individual ends of each cell of the neutron tanks were combined to give a geometric mean pulse height for that cell. The individual ends were also used to calculate a transverse cell position by:

$$x_{ph} = \lambda \cdot .5 \cdot \log\left(\frac{Ph+}{Ph-}\right) + xphoffset \quad . \qquad (15)$$

Here, λ is the effective attenuation length of the scintillator (λ=140 cm), Ph+ and Ph- are the pulse heights taken from the opposite ends of the detector (beam left and beam right, respectively), and xphoffset is the corrective offset to center the position on zero. The offset is used to compensate any systematic inefficiencies in the pulses from one end of a cell and is set to zero as a convenience to analysis.

The propagation time to either cell end for each event in a cell was also used to calculate a position by:

$$x_{tm} = (t_- - t_+) \cdot v2ceff + xtmoffset \quad , \qquad (16)$$

where t_- and t_+ are the timing signals taken from the two ends of the detector, v2ceff is one half of the velocity of light in the scintillator. The mean times for each cell were computed by:

$$MTM = (TMNEG + TMPOS)/2. + MTMOFF(I,J) \quad , \qquad (17)$$

where MTM is the mean time, TMNEG(TMPOS) is the time signal from the negative(positive) end and MTMOFF(I,J) is the predetermined mean time offset for that cell. This mean time was then offset by a constant with respect to the RF and was used as the time of flight for that cell.

The difference between the pulse height generated and the time difference generated positions was monitored with histograms. The width of the "peak" of the difference gave an indication of the intrinsic pulse height resolution of the cell. A sudden widening of this peak was generally a sign that the cell had started leaking scintillator onto the black paper of one of its isolators. This wet surface destroyed the total internal optical reflections within the cell and caused a loss of efficiency for that cell.

When there was only one event within a plane, that event time was designated the time for that plane. Anytime there were events in two adjacent cells within a plane for one trigger, the designated time for the plane was the average time of the two. Triggers occurring with more than two cells firing were excluded from analysis. Relativistic kinematics were then used to calculate the particle's energy from this plane time. Several useful ratios were also computed to be used in tests to eliminate background in the spectra through particle identification and event type selection.

Histograms tested on various quantities were used to monitor the experiment in progress[33,34]. Some of the histograms were as follows:

Multiple hits per plane, which monitored crosstalk between the cells and the relative number of cosmic events.

Cell hit frequency, which monitored the number of times each cell recorded a hit. This tracked the relative efficiency.

Pulse height spectra for singles and coincident hits. This allowed us to watch the gain of the detectors and ascertain the particles of interest in their relative abundance.

Velocity of particles rescattered in the analyzer plane and the velocity ratio of that particle with its predicted velocity, based on kinematics from its locations in the analyzer and catcher planes, which allowed us to make particle identifications and event type selections. The velocity ratio is most useful in that it allows a cut on the slower particles in the system due to wrap-around;

Time of flight and kinetic energy of the neutron, which allowed us to monitor the quality and resolution of the data.

The histogram files are shown in Appendix B. Samples of the above histograms are shown in Figures 19-23.

Most of the tests were used to define event types[35]. This was done in two ways. The first type of definitions were based on trigger types. All of the event trigger types were fanned together into one data word but timed to fall at 20 ns intervals. Gates were then placed around certain parts of the time spectrum defining the corresponding to the event types as determined by this 20 ns interval. The second method was to place a gate around the entire valid region for the pulse height or the mean time and use that gate as a bit test for that cell or device.

Tests were then used to define event types to filter data into the histograms. For example, the energy spectra were tested for a valid NN or NP event, a valid time position and pulse height, the required scattered velocity and velocity ratio.

The test files are shown in Appendix C.

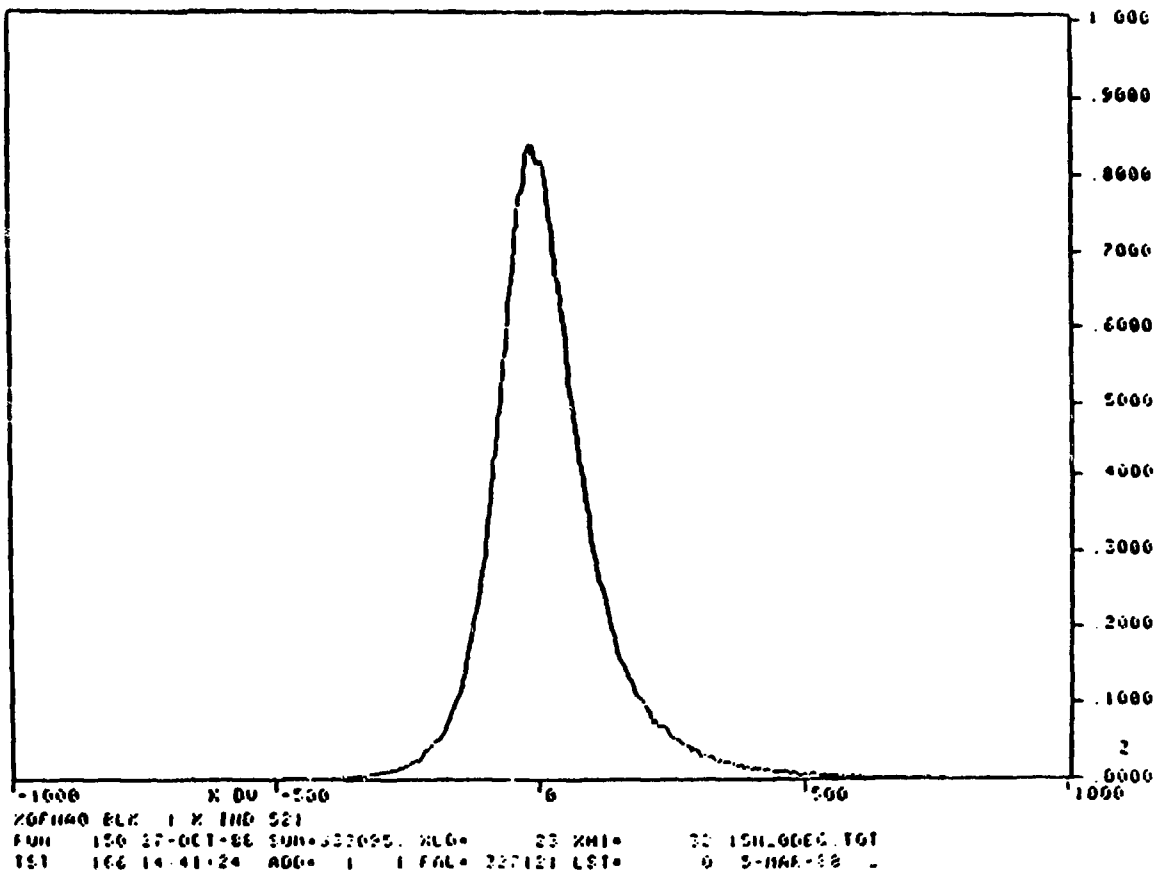

Figure 19 Spectrum of difference between position from pulse height and position from timing.

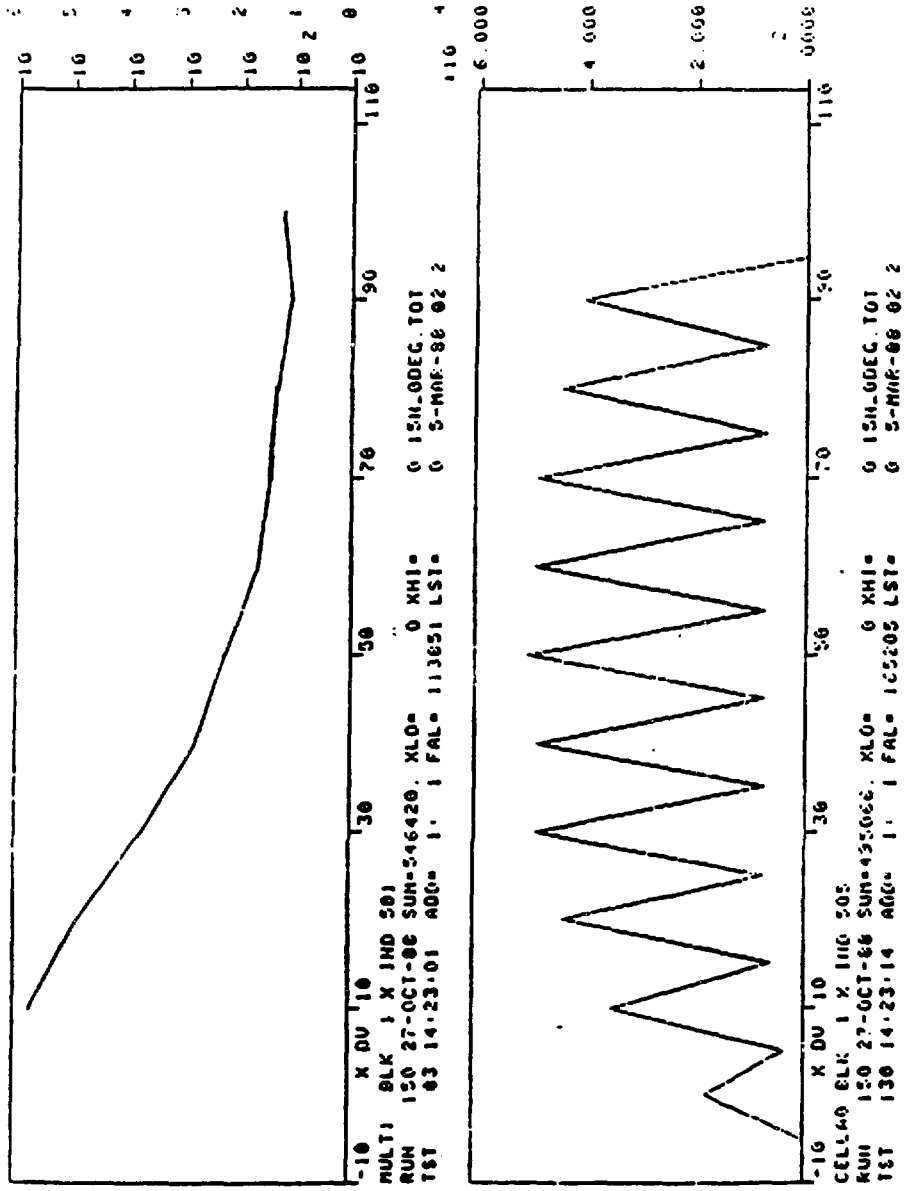

Figure 20 Level of Multiplicity and Counts per Cell.

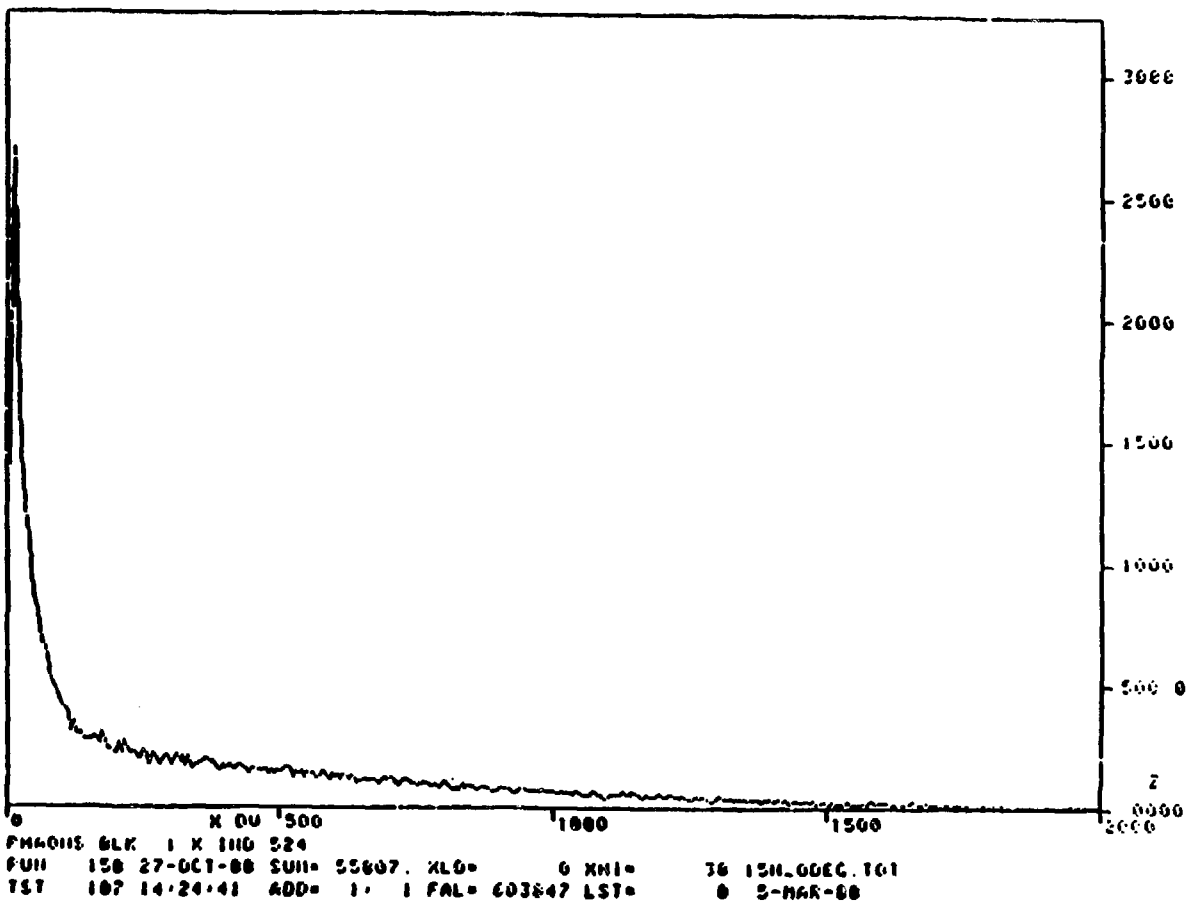

Figure 21 Neutron Singles Pulse Height.

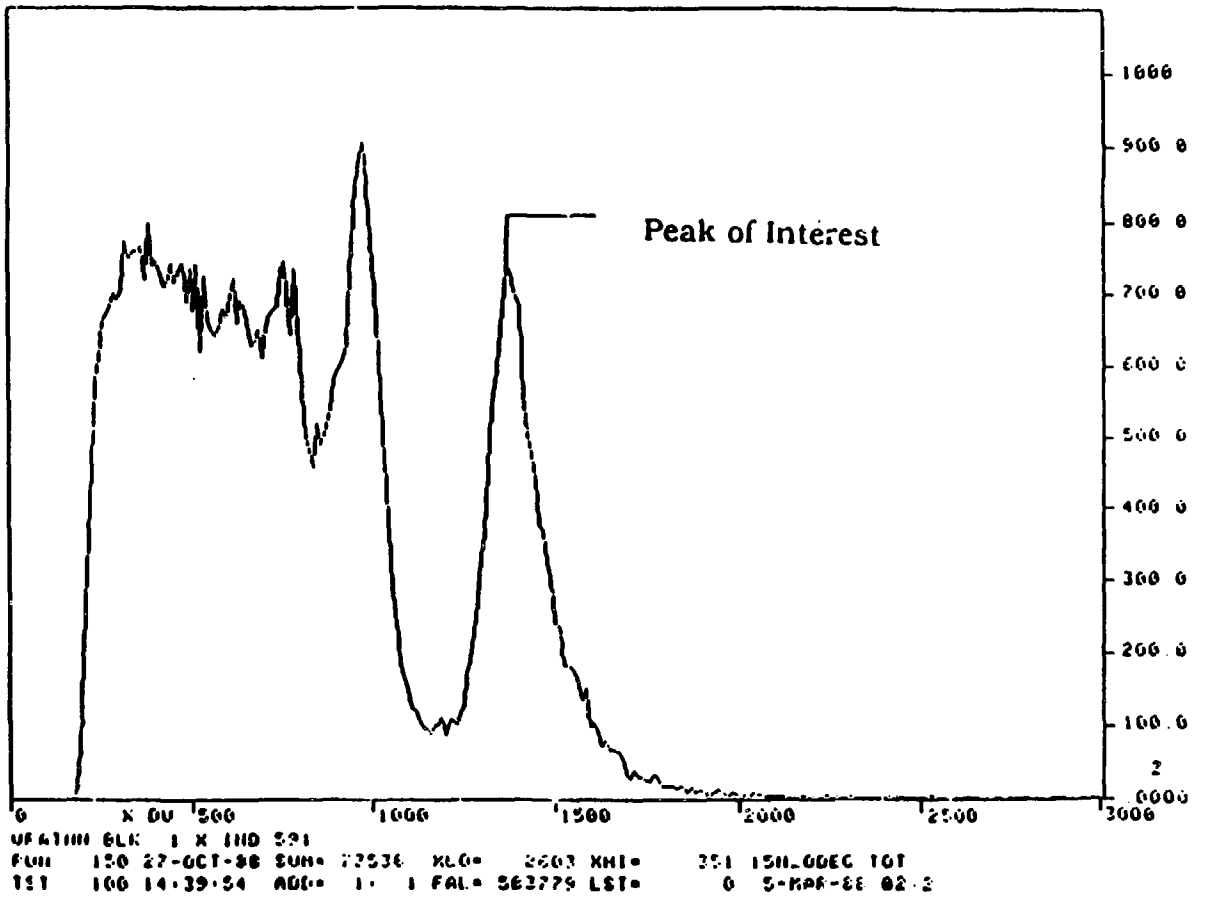

Figure 22 Velocity Ratio of Neutral Events

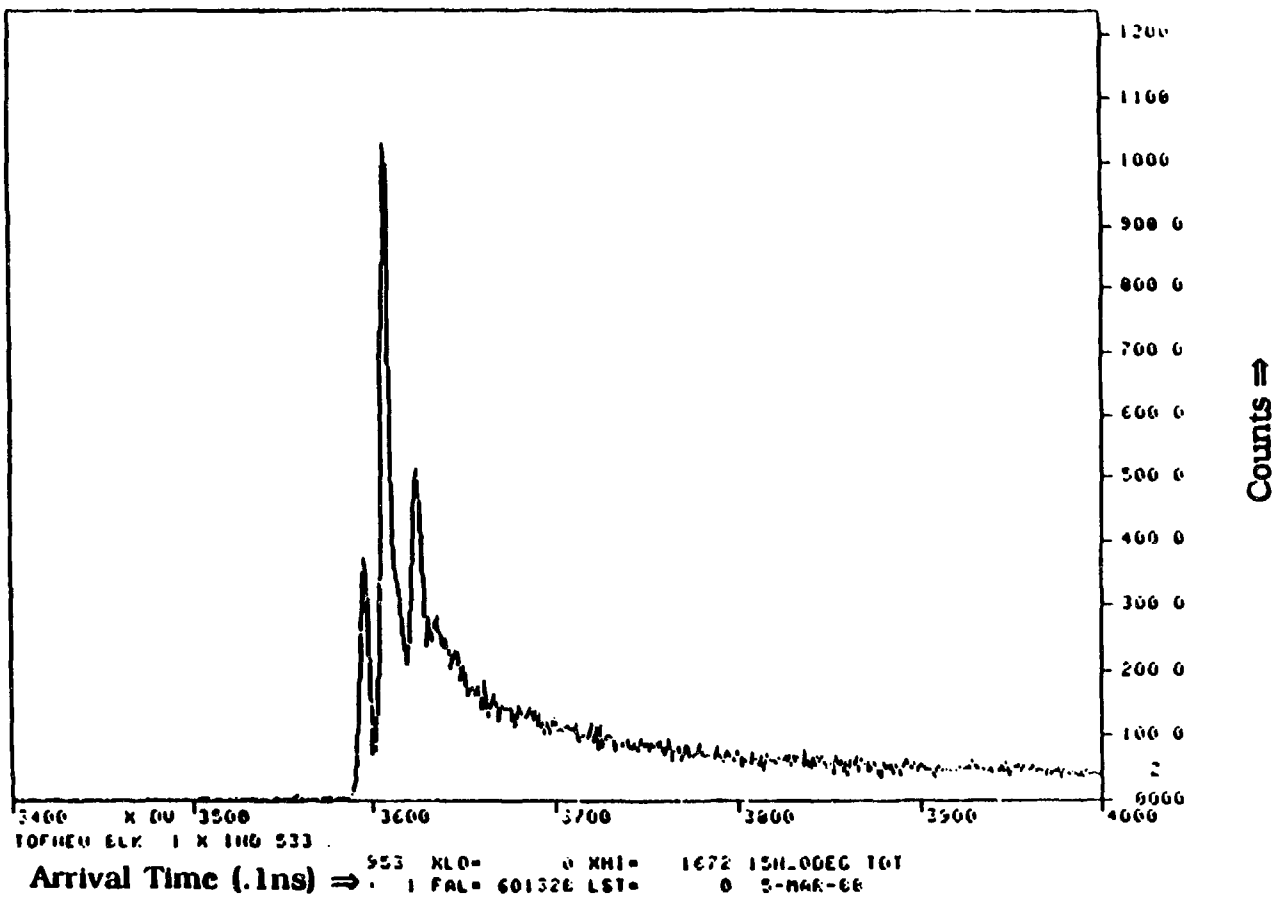

Figure 23 Neutron Time of Flight Spectrum.

II B CALIBRATION SOFTWARE

A system was developed for continuously calibrating the system with cosmic rays exists. It is useful in that it allows the experimenter to shake down and calibrate the gains, relative time and position offsets within the detector system before beam is available. The calibration software is run by the command file CALIBRATE.COM and, with the appropriate histograms and test files installed, takes the accumulated output of a cosmic ray data acquisition run and sets the PMT HV according to gain match factors, the FERA pedestals, the ADC pedestals, the TDC gain conversion factors, the mean time offsets, the pulse height gains, the time of flight offsets, the initial position offsets and the final position offsets. Cosmic rays are used because they are continuously available particles of known energy loss which can pass through all of the cells of a detector tank.

The calibration software consists of the executables CALIBRATE.EXE, XOFFSET.EXE, TOFFSET.EXE, HVGAINMATCH.EXE, HVCNTL.EXE, FERA_GET_PED.EXE, FERA_LD_PED.EXE, LRS4303_CALIB.EXE, along with the histogram, test and command files in the experimental directory CALIBRATE.COM, CALIB.HST, CALIB0.HST, CALIB1.HST and CALIB.TST.

The "pedestals" of the ADCs, or low lying average offsets made by digitizing noise, can be removed from the raw values in two ways. The first is done by subtracting the pedestal in the FERA hardware, the FERA pedestal, and the second by subtracting the pedestal in software, the ADC pedestal. The main differences being that by subtracting the pedestal in hardware, we can zero the channels which have no real signals present and through the FERA zero suppression option, decrease the FERA readout time and decrease the amount of

data written to tape. The purpose in doing pedestal subtraction in software is to subtract from each digitized pulse height a channel which corresponds to the channel of zero signal input. For hardware subtraction, one must eliminate all extraneous noise to allow zero suppression, thus the centroid of the peak and width are pertinent. One must correct in software for this subtraction to return it to the original value.

One of the calibration programs can set the FERA pedestals to be subtracted out as noise. The values are set for subtraction in FERA by the calibration software in the following manner. The high voltage power supplies are turned off so that no real signals interfere. Spectra are accumulated from the noise in the system and read out. The spectrum typically consists of a few channels filled near zero. The program now finds the mean channel of this low lying peak and the root mean square of the width. The pedestal is defined by

$$IPED = XMEAN + 2 \cdot RMS + 2.5 \ . \qquad (18)$$

Here the 2.5 is a small overshoot for security. This number is written into the FERA pedestal register to be subtracted from the raw value held there. PHZERO(*), the pulse height zero offset, must be zero for this selection. The symbol (*) represents the wild card argument for the variable so that the variable has a value for each possible term.

The ADC pedestals are set in a like manner, the difference being that the final values to be subtracted out are the pedestal peak centroid and read into the PRM array as PHZERO(*) to be used by the analyzer. It uses the histogram file CALIB0.HST and should not be used with FERA zero suppression.

The high voltage gain match sections compute new voltages to get the requisite gain but does not install them. Instead it

writes them to a command file, HVGAINSET.COM, which can then be used to set the voltages. The subroutine assumes all these planes are used and generates the starting voltages to be stored in files for each of the neutron detector tanks. To compute gains, the program reads in the old pulse height gains, PHGAIN(*), if available and pulse height offsets, XPHOFF(*). The new gain is queried from the terminal if a specific gain is desired by the experimenter and an array of individual tube voltage exponents can be used with the following equation;

$$HVGAIN = \exp\left(ALOG\left(\frac{PGHAIN}{\sqrt{\exp(2 \cdot XPHOFF/\lambda)}}\right)/NHV(I)\right) \quad . \quad (19)$$

NHV(I) is the specific new high voltage for each tube. The program then sets to unity the PHGAIN(*) and zeros the XPHOFF(*) (so that they must be redone) and writes the command file with the new voltages.

The pulse height gains are set by reading either the core or a saved histogram file pulse height spectra and the PRM values PHGAIN(*) and PHCENT(*), the desired pulse height centroid. The spectra are smoothed and its first derivative taken cell by cell and a centroid found within a window around the desired region. This centroid, CENTROID, of the derivative corresponds to the ΔE edge. The new gains are formed by;

$$PHGAIN = [PHGAIN0(NPRM) \cdot PHCENT(J) / CENTROID \quad (20)$$

and read in the PHGAIN(*) of the PRM array. This section uses CALIB.HST.

The TDC calibration gives the conversion gain from nanoseconds to channels for the digitized time signals. The TFC gains are set by first turning off the high voltage power supplies.

The FERA and data arrays are initialized. Pulses are issued to the TFC to start and stop the TFC. The TFC is read out and the gain calculated by a least squares fit:

$$GAIN = \frac{(N*XY-X*Y)}{(X^2*N-X*X)} \quad , \tag{21}$$

where N is the number of pulses issued, X is the peak centroid for a group of pulses, Y is the number of counts in the centroid channel and XY is X*Y for that peak. The zero is calculated by;

$$ZERO = \frac{(X^2*Y-XY*X)}{(X^2*N-X*X)} \quad . \tag{22}$$

The expected gain is;

$$THEOR = GAIN*XCENT + ZERO \quad . \tag{23}$$

This difference between the calculated gain and the expected gains are output to the screen and a selection is required. If the difference is too large, the gain is reiterated else the gains are written to the PRM variable for use as TMGAIN(*), TRF0GAIN, TEPGAIN and TNTGAIN for the detectors, the 201 RF, the EPP0 timing signal and the NTP0 timing signal, respectively. Results were checked against the 805 MHz for accuracy.

The time of flight offsets can be set from the computer core or a saved histogram as queried from the terminal. The selected source histograms are read in and the centroid found within a window set by the experimenter. These offsets are used in the program TOFFSET which determines the final offset. Two interactions are used. The results are read into PRM as TOFOFF(*). This section uses CALIB.HST.

The mean time offsets are set from a cosmic run with CALIB0.HST and CALIB.TST installed. A mean time spectrum is read in, the MOMENTS subroutine finds the centroid and the values which will offset this centroid to channel 50 is output to the PRM array as MTMOFF(*).

The final position offsets are set with the cosmic calibration software in the following manner: After a cosmic ray data acquisition run is completed with CALIB.HST installed in the histograms and CALIB.TST installed as the test file, the program retrieves the full plane time position histograms, i.e., the sum of all cell position histograms, finds the first moment of the data and reads the centroid's additive inverse into a temporary file. Using this as a correction, the process is repeated for individual cells. The position offsets are then calculated from the pulse height information. The pulse height spectra are read in from CALIB.HST and the old PRM offsets are zeroed. The pulse height position spectra are then smoothed once and the first derivative taken. The first moment is found for each cell and read into another temporary file. The final offsets used in the PRM array are found by reading in the PRM offsets, the temporary files and defining the values as such: (XTMOFF(*), XPHOFF(*), XPLOFF(*)).

III IUCF HARDWARE

We will now look at the Indiana University Cyclotron Facility experimental hardware. This pertains to the data taken at 200 MeV utilizing the neutron time of flight facility at the IUCF.

III A IUCF ACCELERATOR

The IUCF accelerator, Figure 24, is made up of three stages. The beam from these stages is transported to the (p,n) scattering chamber. The neutron flight path then leaves the building to enter a separate neutron detector hut.

The first stage of the IUCF cyclotron is the electrostatic accelerator. It houses a duoplasmic ion source[36]. The source produces $^{1}H^{+}$,$^{1}H_{2}^{+}$,$^{2}H^{+}$,$^{3}He^{+}$ and $^{4}He^{+}$ ions. The $^{1}H^{+}$ ions are selected with slits by a charge selecting magnet. The proton beam is then passed through the terminals of the electrostatic accelerator to reach an energy of approximately .6 MeV.

The .6 MeV beam is then injected into the first isochronous cyclotron. This first cyclotron, the injector cyclotron, is similar to the main cyclotron though smaller. It has four separate magnet sectors. These magnets have a peak field of 15 kG and have windings to correct for constant field to +/- 2% throughout. Two opposite gaps hold independent RF resonators. Each has an autotune circuit to remain on resonance during operation. Though independent, each is customarily set to the same amplitude and equal (opposite) phase shifts for even (odd) harmonics. Extraction from the injector cyclotron is done with an electrostatic deflector.

The main cyclotron is much like the smaller injector cyclotron in configuration. The magnetic field in its sections reach 16.6 kG. Extraction from the main cyclotron is also done with an electrostatic deflector with an additional bending magnet adjacent to the cyclotron.

One beam pulse was supplied to the experimental area approximately every 120 ns with an average intensity of 40 nA.

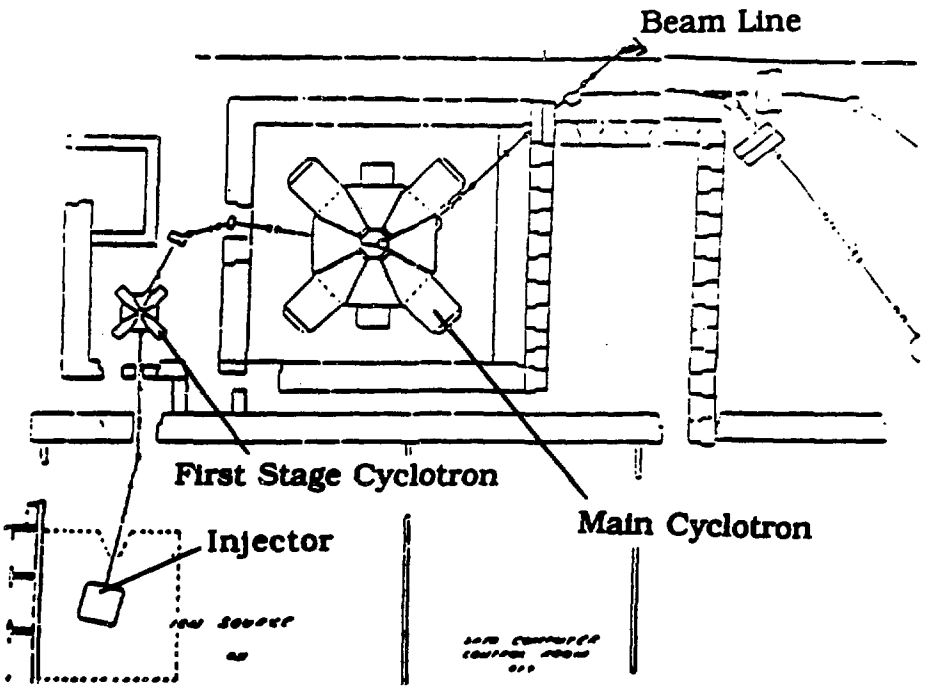

IUCF Source and Cyclotron

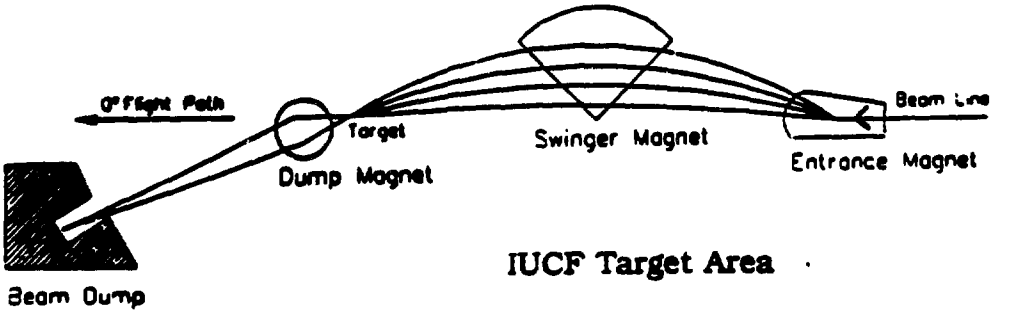

IUCF Target Area

Figure 24

III B POLARIMETERS

Two polarimeters were used for this experiment. The first, the Beam Line 2 polarimeter (BL2), measured the asymmetry from the ^{4}He(p,p')^{4}He elastic scattering reaction at 200 MeV. A He filled gas cell was inserted into the beamline feeding the main cyclotron from the injector between cross section and analyzing power measurement runs. The beam energy loss from inserting the gas cell at this stage was great enough to bring the beam outside the acceptance of the first main stage orbit. To measure the asymmetry, two slits centered the beam on the gas cell. Elastically scattered protons are collimated by two sets of slits for the detectors. There are two detectors, one monitoring scattering to beam left and one to beam right. Spectra from each were recorded and stored separately. Samples are shown in Figure 25. Analysis of these spectra is discussed in Chapter 3, section 1 B.

The High Energy Polarimeter (HEP) at IUCF is mounted in beam line 5 and consists of two pair of NaI detectors. Each pair observes elastically scattered protons from a thin ^{12}C target. The scatters are viewed at 20° in the laboratory system. One pair measured up/down asymmetries and the other pair measured left/right asymmetries. Information from all HEP arms was used to calculate the beam polarization. The method will be discussed in Chapter 3. All of the polarimeter information was taken concurrently with all data runs on an independent data acquisition system. This system used the standard Q system and the standard CAMAC but was run on a separate computer.

The question arises as to whether or not the beam polarization at BL2 was the same as the beam polarization at the target. This question was studied with polarized proton beams

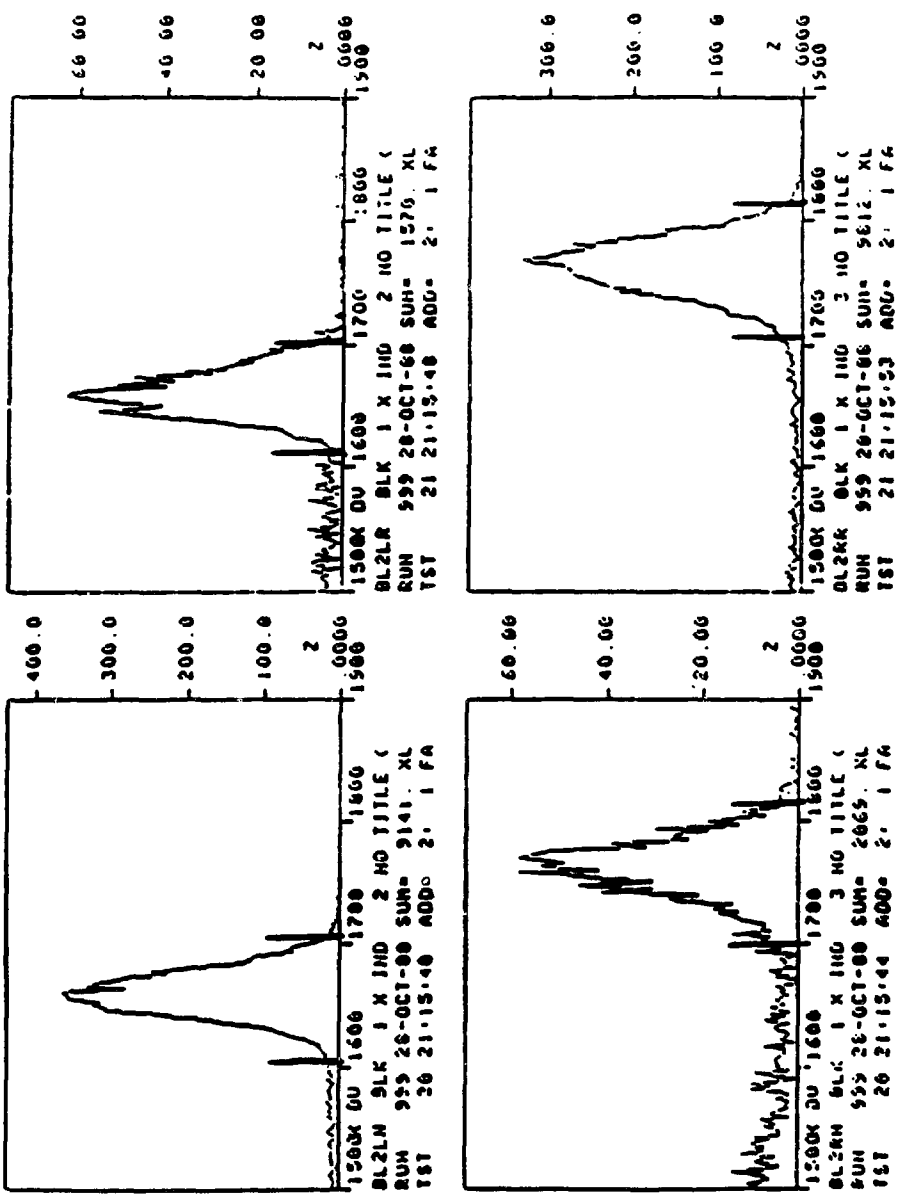

Figure 25 BL2 Polarimeter Arm Spectra.

and polarized deuteron beams at IUCF[37]. For that test, a 180 MeV beam was used and it was found that polarization degraded at most by a few percent. We have assumed that this result remains true for 200 MeV beam and have allowed for depolarization of up to 3% in the analysis.

Polarization changes which might have occurred during data taking runs was monitored via the online results from the IUCF HEP system. Its thin target and position allowed this polarimeter to be used during data runs, though systematic uncertainty for the HEP spectra, as shown in Figure 26, indicated a more precise measurement was possible with the BL2 polarimeter.

III C BEAM PROFILE MONITOR AND TARGETS

The beam was then brought to the (p,n) target. A proton telescope was installed and aimed at the target. It was used to monitor the beam timing profile with respect to the RF. The proton telescope, as shown in Figure 27, was made of a 1" thick scintillator, called the "ΔE" detector, an absorber to range out all but elastically scattered protons from the target and a 4" thick scintillator, called the "E" detector. Kinematic calculations and previous experiments determined the angle of 20° and the absorbers used.

The ΔE detector had two threshold cuts on its pulse height through parallel CFDs as shown in Figure 27. One was to eliminate low pulse heights and the other, high pulse heights. These were "anded" as (Low*Not High) to form a window about those pulse heights for the proper amount of energy deposited by protons elastically scattered from the target and passing through the scintillator.

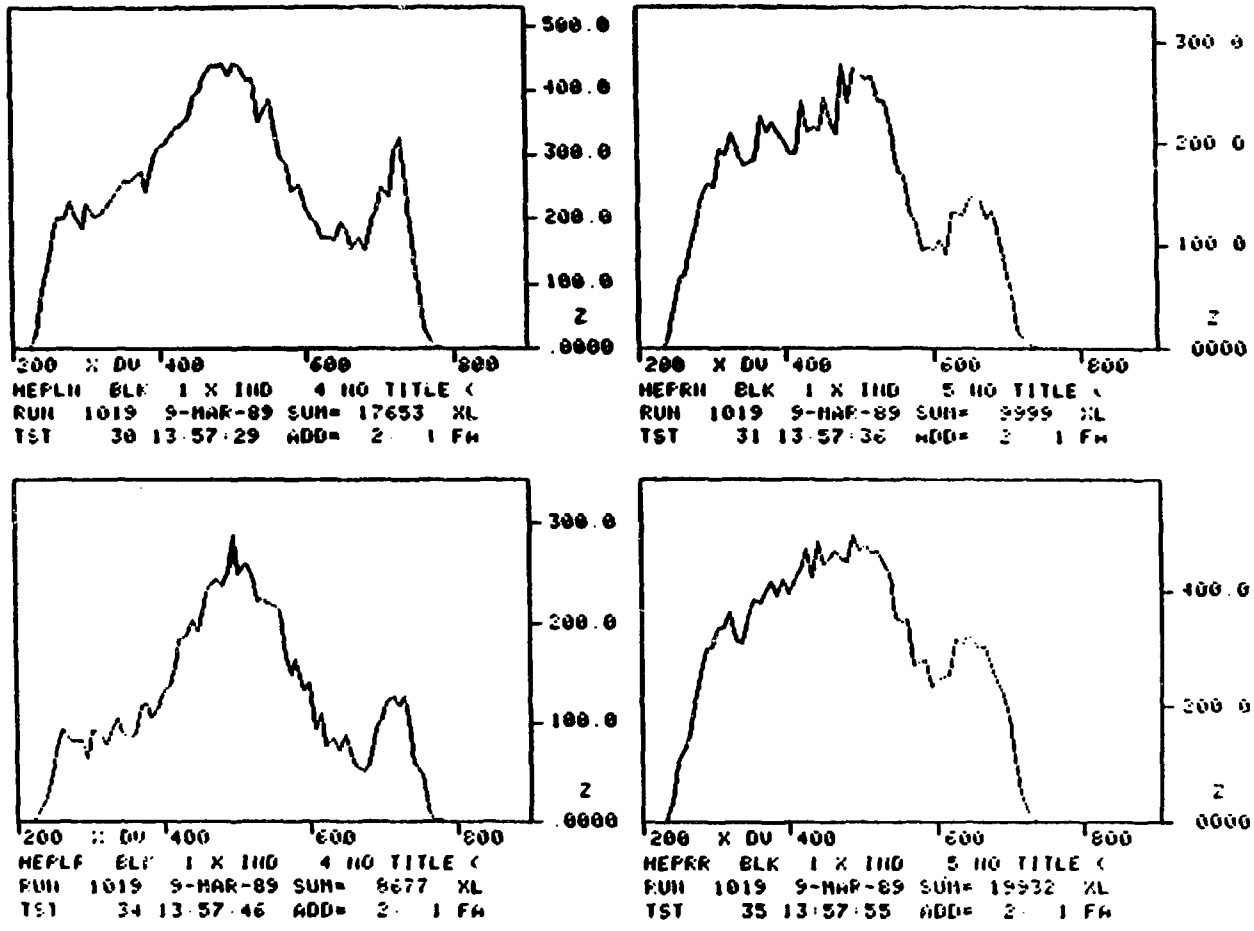

Figure 26 HEP Polarimeter Arm Spectra

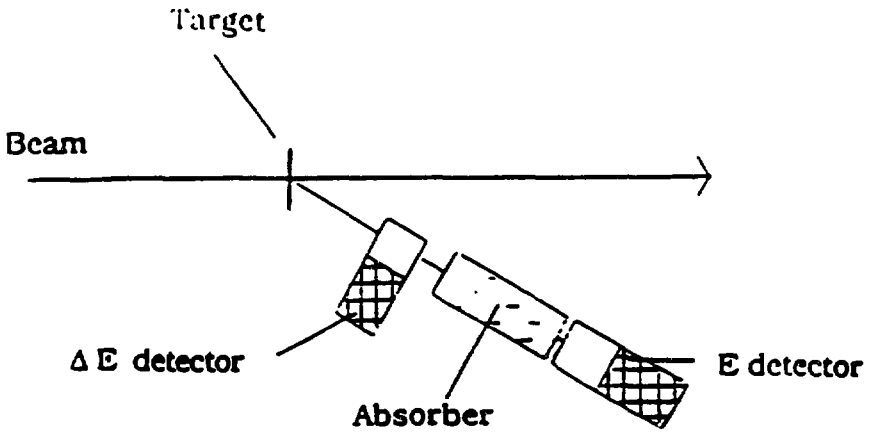

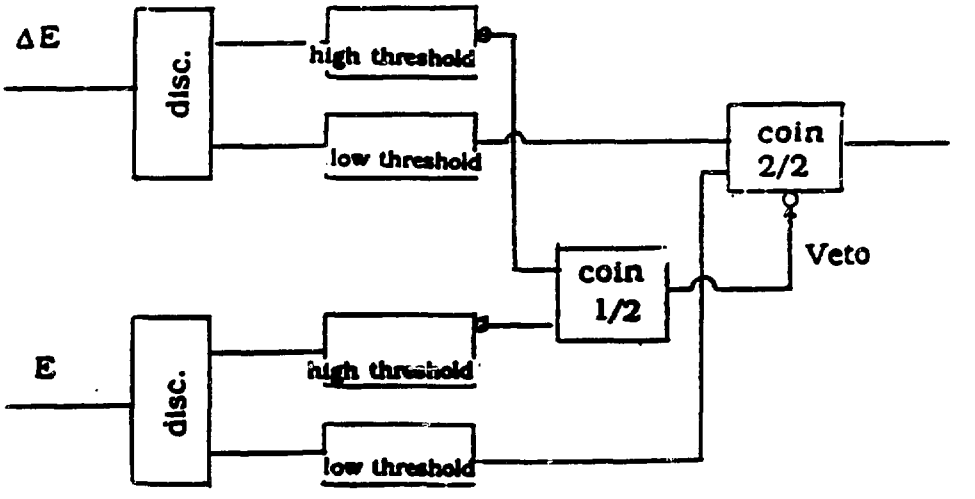

Figure 27 Proton Arm Configuration and Electronics Logic.

The rear scintillator of the telescope had a low pulse height cut and was used to restrict the geometry of the telescope. Hits in both front and back defined an event. Coincidence signals from the proton telescope were sent to the detector hut and included as an event trigger.

Targets used in this experiment are listed in Table 2. The ^{15}N melamine target was a pressed target covered with a layer of CH_2 for protection. Past usage of this target determined that the coating has a negligible effect. The ^{14}N Melamine and the carbon targets were used for measuring contaminations. ^{7}Li was used as an absolute calibration standard. This will be discussed further in Chapter 3, section II D on normalization.

After passing through the target, the beam entered a set of Faraday cups. The Faraday cups, one covering the left half of the beam and one covering the right half, were used for charge integration on this experiment. Charge from the cups was integrated and scaled for analysis. Data analysis utilized the total charge from both Faraday cups.

III D SWINGER AND FLIGHT PATH

The angular distribution was obtained much as it was at NTOF, by varying the angle of the incident beam on target. The flight path was in open air 76 meters in length. The effects of the open air flight path were dealt with in the same manner as the 494 MeV data. The air caused an estimated attenuation of 85.6% and was corrected for along with other matter in the beam path, (detector hut wall, detector covering, etc.) through ^{7}Li normalization.

III E DETECTORS

The detectors consisted of four bars of plastic scintillators 10 cm x 15 cm x 100 cm, stacked perpendicular to the flight path. Photomultiplier tubes, Amperex XP2262, and CERN bases gathered light from both ends of each bar. Each bar was wrapped in black paper for total internal reflection and to keep each bar optically isolated. Position resolution of these bars is ~5 cm along its length for neutrons at 200 MeV. The arrangement is shown in Figure 28.

A second plane of detectors was stacked .55 meters behind the first with a charged particle veto paddle set in between them. The second plane and the veto paddles were included in hopes of analyzing NN and NP coincidence events. The added material from the front plane degraded the resolution of the second plane to a point that necessitated the exclusion of the NP data from the final calculations. Low statistics in the peak of interest excluded the use of NN data in the final analysis.

III F ELECTRONICS

The fast electronics for the 200 MeV run followed the same logic as that of 494 MeV. The actual modules varied according to availability. Naturally, delays, gate widths and thresholds were commensurate with 200 MeV neutrons at 76 meters. The logic diagram is shown in Figure 29.

The system used to relay the information from the electronics to the computer was different from that used for the 494 MeV data. The 200 MeV data were taken with CAMAC and were being read out by an MBD. The ADCs and TDCs used with CAMAC were read out after each event. The MBD is capable of

Table 2

Target	Target Thickness
^{7}Li	1 cm
^{12}C	358. $^{mg}/_{cm^3}$
^{13}C	96. $^{mg}/_{cm^3}$
Melamine $^{12}C_3H_6{}^{15}N_6$	704.6 $^{mg}/_{cm^3}$

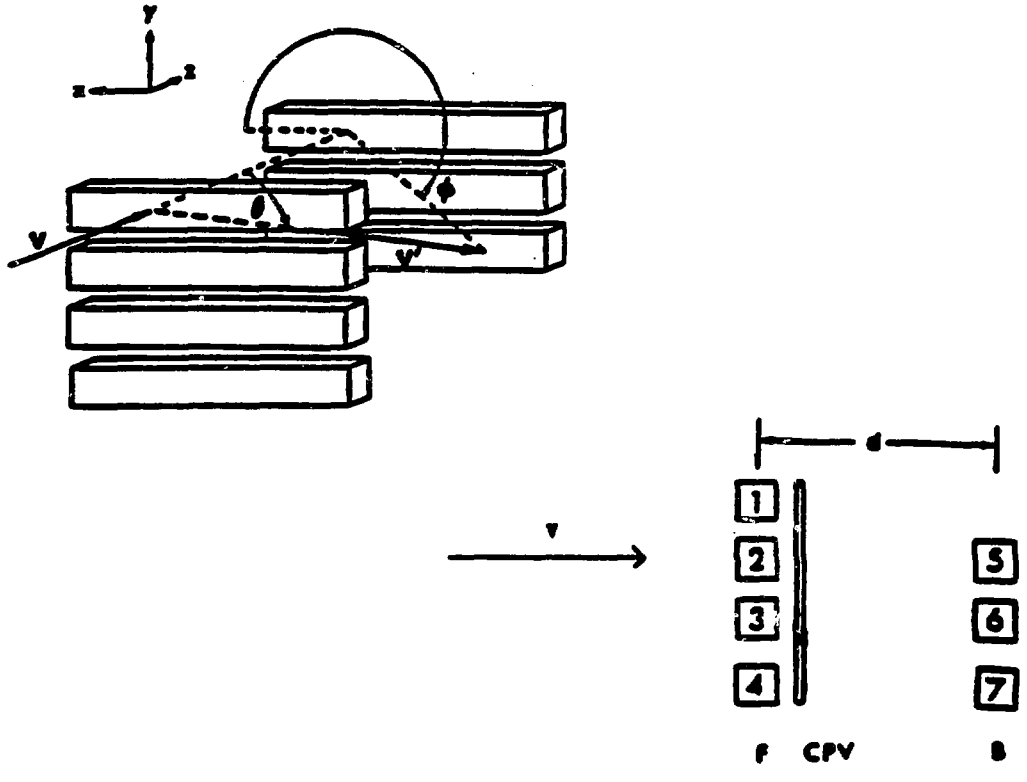

Figure 28 IUCF Detector Configuration

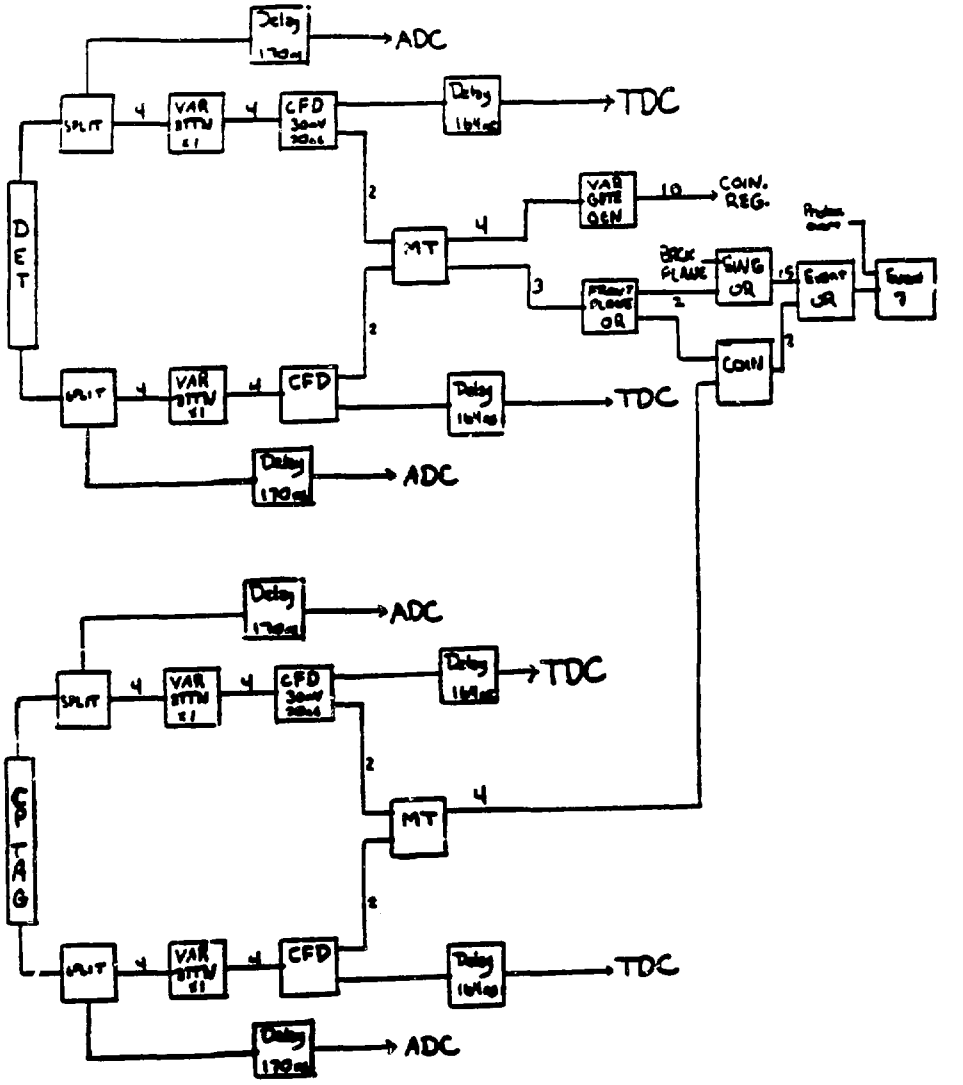

Figure 29 IUCF Electronics Logic

performing early cuts on the data, which can reduce the amount of data actually analyzed by eliminating undesired events sent to the computer and ultimately recorded on tape. No MBD cuts were used during this experiment.

III G SOFTWARE

The analyzer used was an abbreviated form of the analyzer used for the 494 MeV data run. The number of planes and cells looped over in the program were changed to reflect the IUCF arrangement. The front plane was selected for the final results by using only those spectra from the histogramming system. The events with acceptable positions and pulse heights were used to make the time of flight calculations to determine the energy of the incoming neutron in the same manner as the 494 data analysis.

CHAPTER 3

DATA ANALYSIS

The 494 MeV data consisted of measurements taken at laboratory angles 0°, 1°, 2°, 3°, 4°, 5°, 7°, 9°, 10.2°, 11°, 12.5°, 14°, 16°, and 18°. Up to 160 data words per event were recorded to tape along with scaler sums which were read out every ten seconds. Data words included pulse height and timing signals from the detector array, beam polarimeter and current monitor information, and beam spin status information.

The 494 MeV analyzer, or program used to analyze the raw data, was basically the same program used to sample data on line. One change was implemented. A section of code was included which would find the centroid of the peak of the beam monitor time of flight spectrum. It finds the centroid within a window placed around the peak representing the primary beam bunch. It finds the deviation of the peak from the value calculated from beam energy and continuously (every 100 events) change the RF time offset to keep the centroid in the specified channel. This kept the times of flight calibrated.

At 200 MeV , data were taken at laboratory angles 0°, 6°, 9°, 12°, 15° and 18°. Over 20 data words for each event were

recorded on tape including detector pulse height and timing signals from the detector hut as well as monitor event signals from the proton arm. All beam polarimetry data was processed on line and stored as histograms for analysis.

The 200 MeV analyzer was the same basic program used to analyze data on line. A similar change to the 494 MeV process was used here. It allowed us to track the mean energy of the beam with the proton arm. This helped to compensate for sudden shifts and drifting in the timing signal with respect to the RF signal. This improved overall stability to 80 ps at the ground state of ^{15}N.

All good hits were processed by the analyzer to be made available for spectra. A gate was placed around the entire mean time spectrum for each cell or CPV plane. "Trues" in these mean time tests were combined to define the various trigger types and determine multiplicity. In the final data analysis, all triggers involving more than one event per plane were ignored. This is because multiple hits in a plane would only confuse the true track of the particle. The remaining data was formed into a time of flight spectrum which was converted into an energy spectrum with standard relativistic kinematics.

I MEASURED QUANTITIES

I A POLARIZATION - 494 MEV

Polarization information was present from three sources. Online analysis compared the two polarimeters, EPPO and NTPO, in the beam channel for consistency to each other as well as compared them against the High Resolution Spectrometer polarimeter (which branches off of the same beamline) for

relative polarization strengths. This polarimeter is simply a polarimeter using the same beam. Though beam transport had precessed the polarization angle, checking the ratio of that polarimeter to EPP0 served as a stability check.

To calculate the polarization we start with:

$$PA = \frac{r - 1}{r + 1} \tag{24}$$

where A is the analyzing power of the polarimeter target, (known from previous measurements), P is the desired beam polarization and r is the measured asymmetry ratio given by:

$$r = \sqrt{\frac{L_N \cdot R_R}{L_R \cdot R_N}} \, . \tag{25}$$

Here, Ln(Rn) is the number of detected elastically scattered protons scattered to beam left(right) while the beam spin direction is normal to the scattering plane. Lr(Rr) is the number of detected elastically scattered protons scattered to beam left(right) while the beam spin direction is reverse to the scattering plane. These numbers are tabulated by the scalers, accidentals were subtracted and the result normalized with computer dead times. The polarizations measured and their uncertainties are given in Tables 3 and 5 at the end of the chapter.

The analyzing power,A, is .510 and .479 for NTP0 and EPP0 respectively at 500 MeV. The 'accidental' coincidences recorded by the scalers as discussed in Chapter 2, give a direct measure of background occurring in the polarimeter during a

beam burst. This lends an uncertainty to the polarization given by[37]:

$$\Delta P=\sqrt{\left(\frac{((L_R\cdot R_N)^4(L_N+R_R)+(L_N\cdot R_R)^4(L_R+R_N))}{A((L_R\cdot R_N)^2+(L_N\cdot R_R)^2)^4}\right)^2+\Delta A\left(\frac{P}{A^2}\right)^2} \quad (26)$$

where ΔA is the effective uncertainty of the analyzing power of the polarimeter as given by McNaughton[25].

1 B POLARIZATION - 200 MEV

Data from each arm of the HEP were stored separately in energy spectra so that polarizations could be determined on line automatically and checked later. The resolution of the HEP turned out to be somewhat less than that of the BL2 polarimeter as seen in Figures 25 and 26. Since the HEP could be used during data taking runs, it was used to monitor polarization for sudden shifts. The (BL2) polarimeter, which is located between the injector and the cyclotron, was used for the absolute polarization measurements.

Yields from the individual arms used to determine polarization at BL2 were taken as the total number of counts in the spectrum within a gate as opposed to scalar readouts used at NTOF. Sample gates are shown in Figure 25. The analyzing power of BL2 at 200 MeV is .991. The beam polarization was computed in the same way as NTP0 and EPP0 at LAMPF, using Equation 24.

The Yields from the stored HEP spectrum in Figure 26, were read at request from the computer memory core. Yield was defined as the total counts within a gate. These gates were reset each run to offset the effects of the beam drifting on the

polarimeter target and the timing drifting with respect to the RF. The analyzing power for the HEP was .893 for 200 MeV. Equation 24 was used to calculate the polarization in the normal direction with the left/right counters and in the "sideways" direction with the up/down counters.

I C YIELDS

To determine the cross section and the analyzing power, it is necessary to extract the number of counts or yield from the peaks of interest in the energy spectrum. Yields were extracted in several ways as resolution degraded and the buncher was mistuned. These methods included fitting the peaks quadratically, (with a parabola), with a least squares fit and fitting a gaussian distribution to the peak (symmetric or asymmetric, with or without exponential tail). The method used for the final results consisted of taking the number of counts in the region of interest and subtracting out the background. The region of interest was defined on the low energy side of the peak as the minimum point between the ground state and the first excited state. On the high energy side of the peak the boundary was the point where the peak met the projected linear background.

The results were checked against yields from more sophisticated programs such as GAUFIT[38] and PEK[39] which fit the data as described above. The results obtained agreed with those from the unbiased yields to well within experimental errors (to be discussed later). The results from the raw counts were then used as they were believed to be the most representative of the peaks i.e.; the were unenhanced. Identical regions were used for both normal and reverse spin states.

Background under the peak was taken by projecting the background from slightly higher in the energy spectrum to underneath the peak of interest. We note that the background in this region is essentially linear. This projection was done with a least squares fit as given by Bevington[37], of a line through the background of higher energy as is shown in Figure 30. Interference from the first excited state of ^{15}O was disregarded as our resolution gave sufficient peak separation in most cases. Everything below this background line was subtracted out.

The 2° and 7° points did pose certain problems. During these runs, the HER was out of tune and significant tails appeared on the beam. The gamma flash spectrum, from 15N(p,p'γ) in the target, is shown in Figure 31. This presented problems not only in that the tail must be included in the ground state yield but the tail from the first excited state must be accurately subtracted out. To solve these problems, the peak shape from the gamma flash spectrum was fitted. This fit was expanded to fit the wider neutron peak of the first excited state and subtracted out. The remaining ground state peak was visually fitted with this shape as a check, after subtracting linear background, and the total remaining counts in the spectrum were used in the final yield. This analysis assumes that the velocity distribution within a bucket of neutrons is approximately uniform for the bucket peak and tail. No information exists as to whether of not this is true, but there is no other measured approximation to the neutron bucket time profile. The peaks subtracted from the 2° spectrum are shown in Figure 32.

The only state from other constituents of the target which could have contaminated the spectrum was the ground state of ^{13}N from $^{13}C(p,n)^{13}N$ in the naturally occurring carbon in the melamine. This peak's contamination of the spectrum was found to be negligible by locating the first excited state of ^{13}N in the

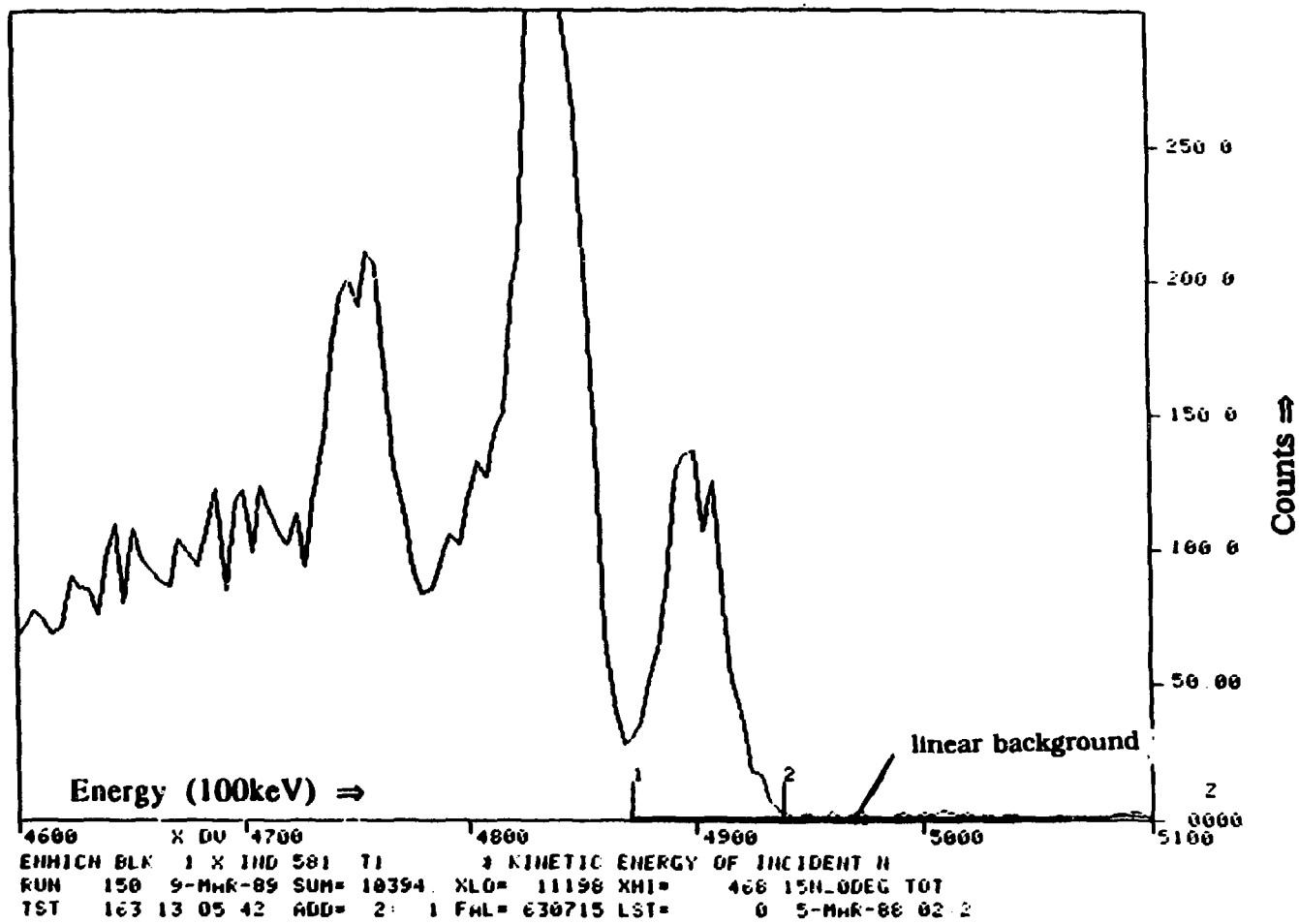

Figure 30 $^{15}N(p,n)^{15}O(g.s.)$ with linear background

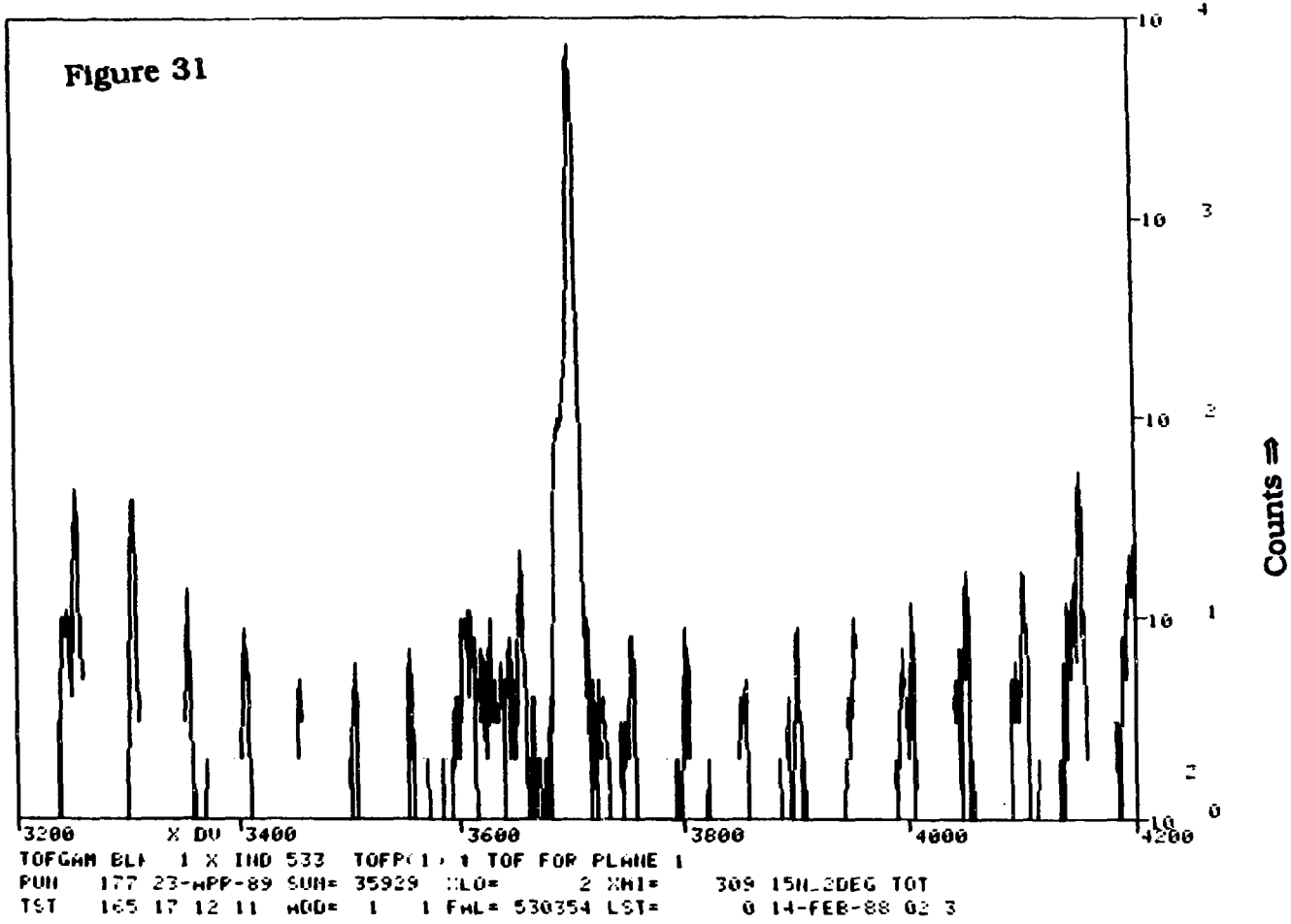

Gamma Time of Flight Spectrum at 2° with mistuned rebuncher.

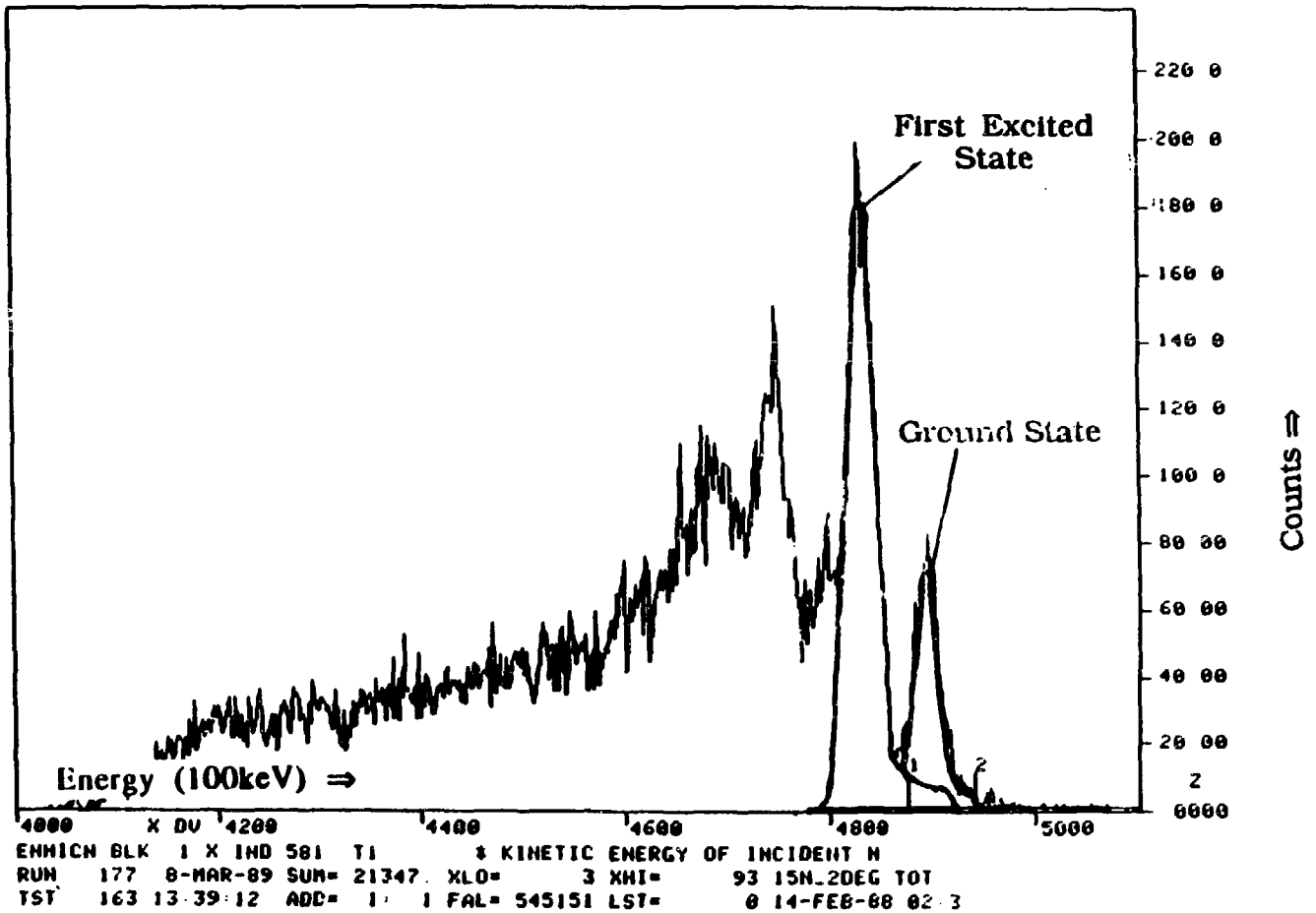

Figure 32 $^{15}N(p,n)^{15}O(g.s.)$ Energy Spectrum at 2° showing peak shapes used to determine yeild.

$^{15}N(p,n)^{15}O$ spectrum. $^{13}C(p,n)^{13}N$ spectra were taken at each angle along with $^{15}N(p,n)^{15}O$ spectra. The relative strengths of the first excited state and the ground state were measured for ^{13}N. By comparing this ratio to the strength found in the ^{15}N spectrum, we saw that the contamination to the ^{15}O ground state by the ^{13}N ground state was a less than one per cent. A $^{13}C(p,n)^{13}N$ spectrum is shown in Figure 33.

II CALCULATED QUANTITIES

II A CALIBRATION

Extensive work was done to maintain calibrations of the system. At the beginning of the run, the ADC pedestal values were measured so they could later be subtracted out in software from the pulse heights. The high voltages to the PMT bases were adjusted to gain match the ends of each cell. Software corrections were included in the program to fine tune the pulse height gains. Timing offsets were added in the software to account for differences in delay from the individual cells. Position offsets corrected the minor differences between the two ends of a cell's timing signals.

During the data analysis, each run was played back individually. All calibration constants were found at the end of the run and used as initial calibration constants for the next run. Some quantities, such as the relative beam timing from the beam profile monitor, were tracked during the run and corrections applied while running. The tracking was achieved by finding the centroid of the peak of the beam monitor spectrum within a predetermined gate. The spectrum used was clean enough so that only the peak of interest had any effect on the calculation.

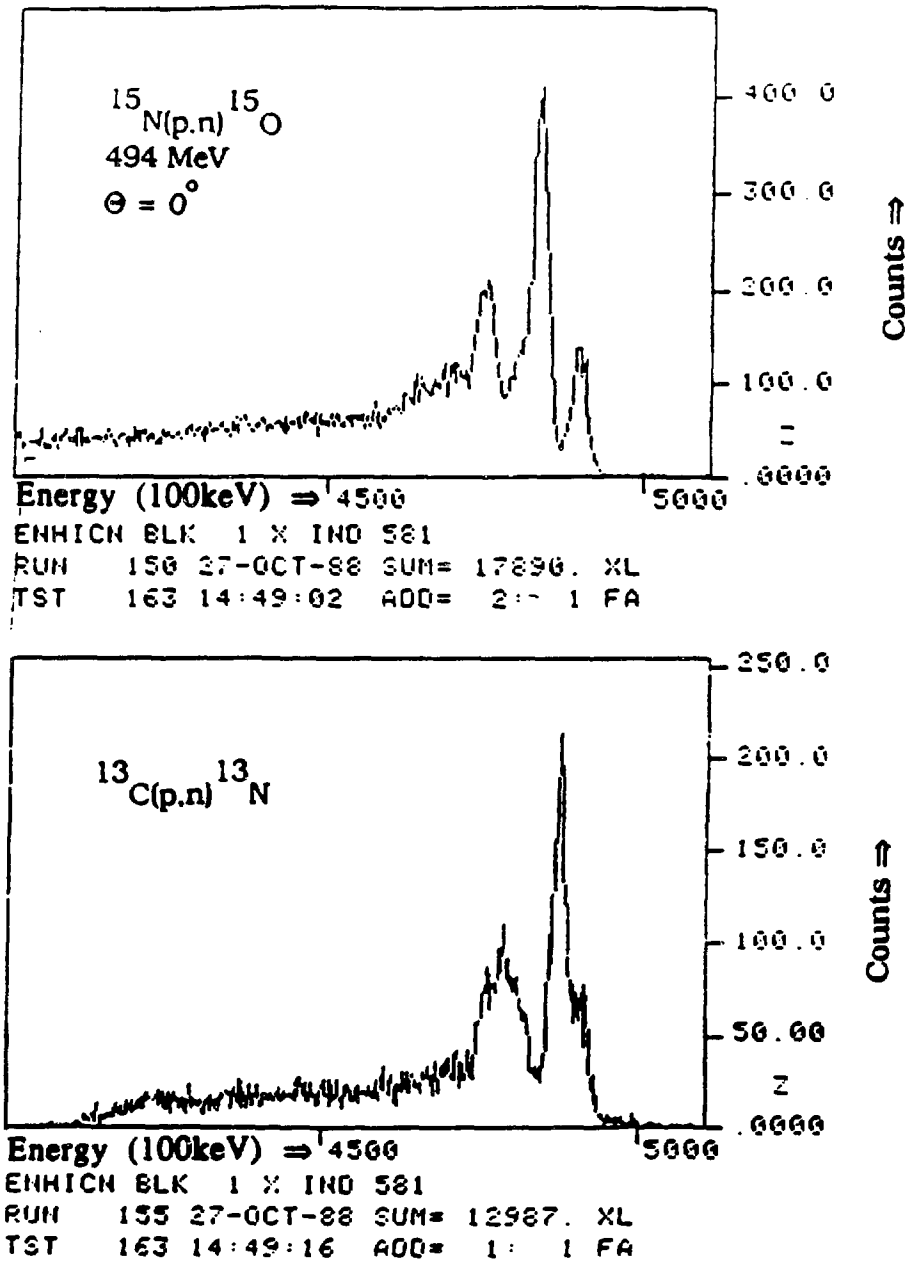

Figure 33 **Energy Spectrum Contamination Spectra**

The centroid was then compared to its last value and adjustments were made to the RF offset. This greatly reduced the impact of the beam's energy or relative timing drifting and also improved resolution. Figure 34A shows an example of a cumulative spectra of the beam profile. The double peak indicates that the beam timing shifted during the data acquisition. Figure 34B shows the same profile after the tracking correction was made.

For each run, the mean time in each cell taken from the gamma flash of the beam hitting the target was offset to zero. The TDC software time conversion factors calibrated the TDCs to .1 ns per bin and the offsets for each plane were then set so that the gamma flash occurred at the calculated time in the spectrum. This was in channels 2735, 2793, and 2802 for the first, second and third planes of the 494 MeV run and channel 2555 for the 200 MeV run. These channels corresponded to the time of flight of the neutrons in .1 ns calculated from the beam energy. All gamma flash centroids were calibrated to less than 40 ps. Position offsets were corrected by cumulative cosmic ray spectra taken between spills as stated in Chapter 2, section I H 2.

The energy of the incoming beam was checked by computing the time difference between the ground state and the 15.11 MeV state of ^{15}N after the TDC gain was set. It was found that any variance in the beam energy of up to 2% in the kinematic equations had a negligible effect upon the yields.

The incoming beam angle from the swinger had an uncertainty of +/- .2%. There was no shift detected between the normal and reverse spin beams.

The effects on the final cross sections of the uncertainty in the ^{7}Li normalization constant as discussed in Chapter 2, sections I E and III D, were less than 1%.

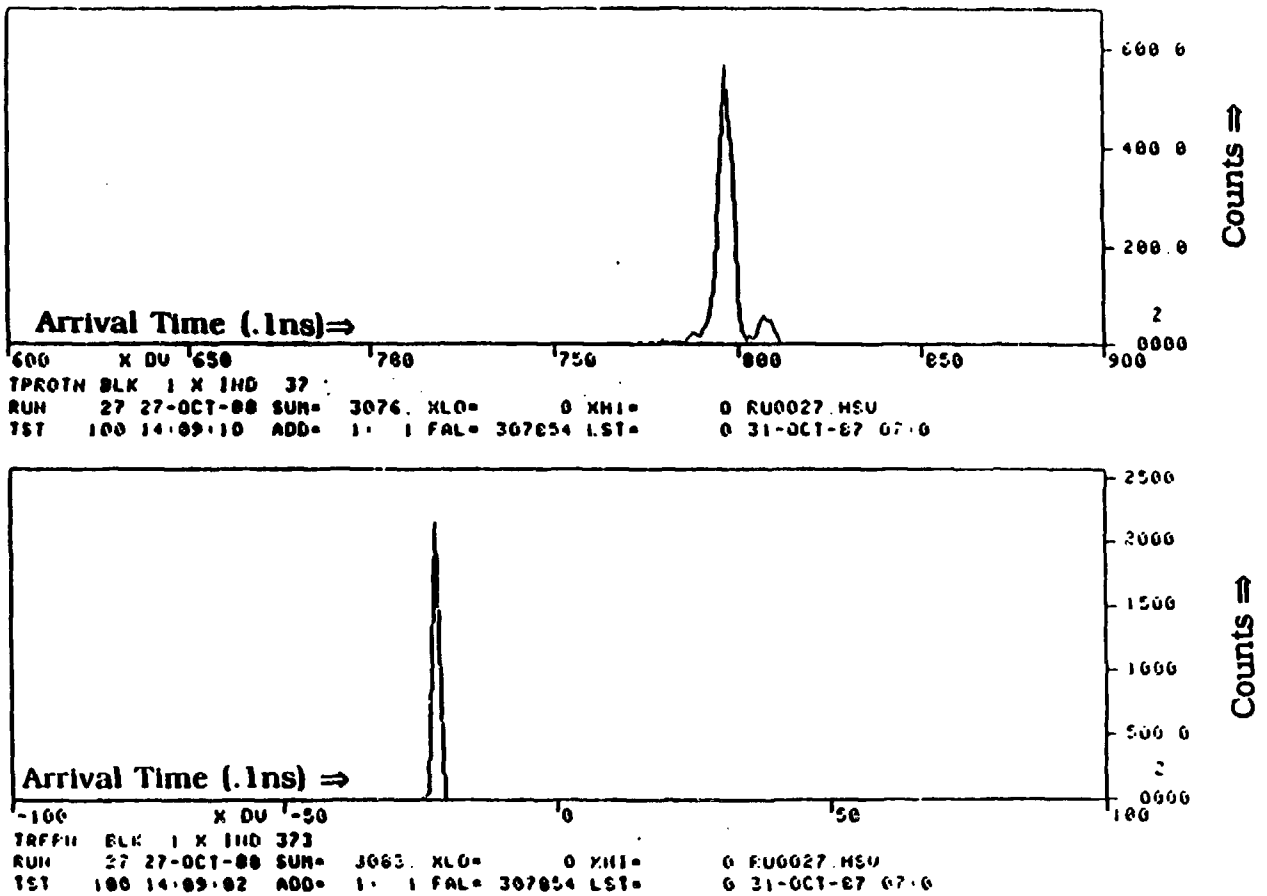

Figure 34 Uncorrected and Corrected Beam Profile.

II B CALCULATION OF CROSS SECTIONS

The calculation for cross section is given by:

$$\frac{d\sigma}{d\Omega} = \frac{1}{2}\left(\frac{Y_n}{Q_n} + \frac{Y_r}{Q_r}\right)\frac{1}{Norm \cdot N_t} \quad , \tag{27}$$

where Yn (Yr) is the yield with the spin in the normal (reverse) direction and Qn (Qr) is the measured current normalization factor with the beam spin in the normal (reverse) direction. N_t was the target thickness with respect to the angle of the incoming beam. "Norm" was the overall normalization constant as determined by the ^{7}Li runs. It accounts for of attenuation, beam duty factor, charge normalization constants and detector efficiency.

We know that all neutrons are not detected. Some neutrons are not counted because the hardware is busy processing another event. We can add a factor to the equation for σ called Lt (livetime) to compensate for the time the computer will not accept events during a beam spill. It is defined as

$$Lt = \frac{\text{TAPED TRIGGERS}}{\text{EVENT 7}} = \frac{\text{\#Recorded Events}}{\text{\#Actual Events}} \tag{28}$$

so that

$$\frac{d\sigma}{d\Omega} = \frac{1}{2}\left(\frac{Y_n}{Q_n \cdot Lt_n} + \frac{Y_r}{Q_r \cdot Lt_r}\right)\frac{1}{Norm \cdot N_t} \quad , \tag{29}$$

where TAPED TRIGGERS, (TAPPED TRIGGERS = EVENT 7 · BUSY*), is the raw number of events which occurred while the system was ready to take data and EVENT 7 is the raw number of events that occurred. Typical live times were around 96% for 494 MeV and 89% for 200 MeV.

II C CALCULATION OF ANALYZING POWERS

The analyzing power is given by:

$$A = \frac{\frac{P_n Y_n}{Q_n \cdot Lt_n} - \frac{P_r Y_r}{Q_r \cdot Lt_r}}{\frac{P_n Y_n}{Q_n \cdot Lt_n} + \frac{P_r Y_r}{Q_r \cdot Lt_r}} \qquad (30)$$

where Pn (Pr) is the polarization strength in the normal (reverse) direction. The yields for normal and reverse spin undergo the same corrections as the yields for the cross sections. Polarization for each angle and target were taken as the average polarization of each run making up that data set, weighted by the current monitor scalar output for that run.

II D NORMALIZATION

We were able to obtain absolute cross sections by calibrating to ^{7}Li cross sections in the following manner:
We know the total cross section is given by[40]:

$$\sigma_{TOT} = \frac{2\pi}{K_1 \cdot K_3} \int_{q_{min}}^{q_{max}} dq \cdot q \cdot \sigma(q) \quad , \tag{31}$$

where

$$q^2 = K_1^2 + K_3^2 - 2K_1 \cdot K_3 \cdot \cos\theta \quad ,$$

$$q_{min} = K_1 - K_2 \quad , \qquad q_{max} = K_1 + K_2 \tag{32}$$

and K_1 and K_3 are the momentum of the incoming and outgoing nucleons respectively. We see in Figure 35 cross sections as a function of q for ^{7}Li for an energy range of 80 MeV to 494 MeV. We note that it is independent of incident energy; that is , all curves coincide to within experimental error regardless of the initial energy. All data in Figure 35, except those for this study, were normalized via activation studies. Thus $\sigma(q) = \text{const.}$ and

$$\int_{q_{min}}^{q_{max}} dq \cdot q \cdot \sigma(q) = \text{const.} \tag{33}$$

We set this constant, to an extent, by noting for known q, 0° is the easiest point to measure and the most exact. This gives:

$$\frac{\sigma(q)}{\int_{q_{min}}^{q_{max}} dq \cdot q \cdot \sigma(q)} = \text{const}_1 \,., \quad \frac{\sigma(0°)}{\int_{q_{min}}^{q_{max}} dq \cdot q \cdot \sigma(q)} = \text{const}_2 . \tag{34}$$

so that

$$\sigma_{TOT} = \frac{2\pi}{K_1 \cdot K_3} \frac{\sigma(0°)}{\text{const}_3 .} \quad . \tag{35}$$

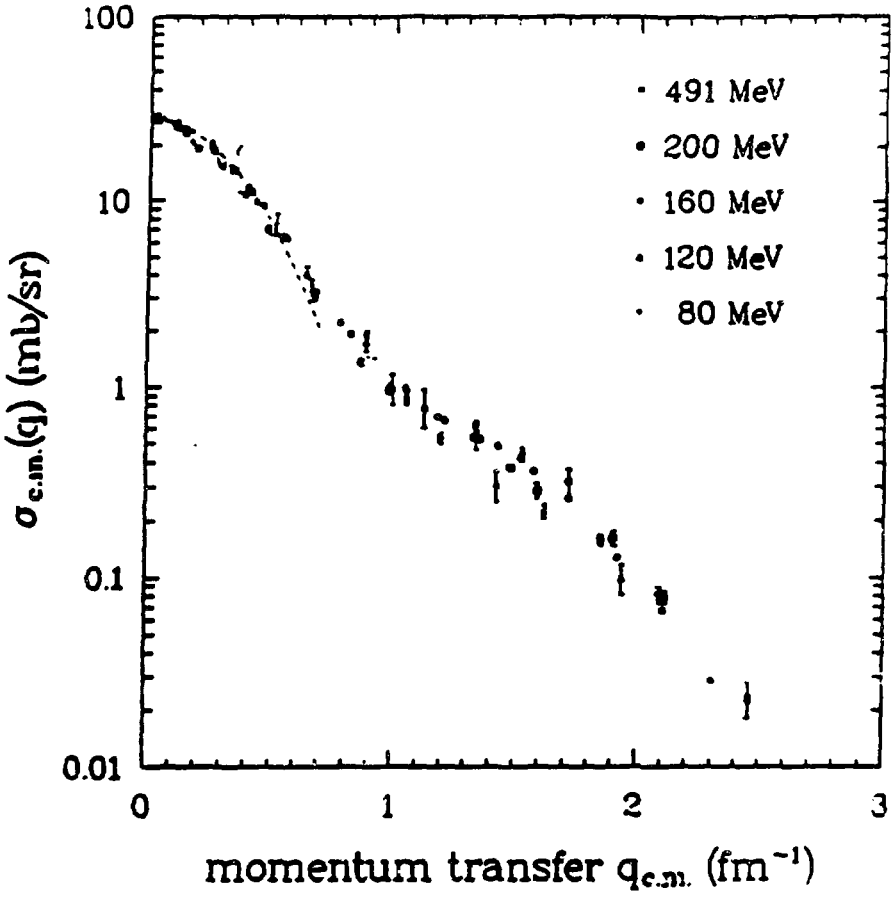

Figure 35 Integrated ^{7}Li Cross Section.

This gives

$$\sigma(0°) = \frac{\text{const.}}{2\pi} (K_1 \cdot K_3 \cdot \sigma_{TOT}) . \qquad (36)$$

Experimental results of cross section verses $K_1 \cdot K_3$ are shown in Figure 36. As well as can be measured, this quantity is seen to be linear. We write:

$$(K_1 \cdot K_3 \cdot \sigma_{TOT}) = \text{const.} \qquad (37)$$

and by putting this into equation 33,

$$\sigma(0°) = \text{const.} \qquad (38)$$

for all energies.

Given this, we measured σ for ^{7}Li and used this value to give a scaling factor to the correct calibration. We also continued to measure cross sections for ^{7}Li as we moved in angle through out the experiment. We used this data as a constant check of Figure 35 and as a diagnostic indicator that our calibration was not drifting. Data points taken during this study are included in Figures 35 and 36.

III ESTIMATION OF ERRORS

The factors included in our evaluation of errors in σ and A are both statistical and systematic. Throughout the analysis, errors were estimated to maximize the quantitative significance

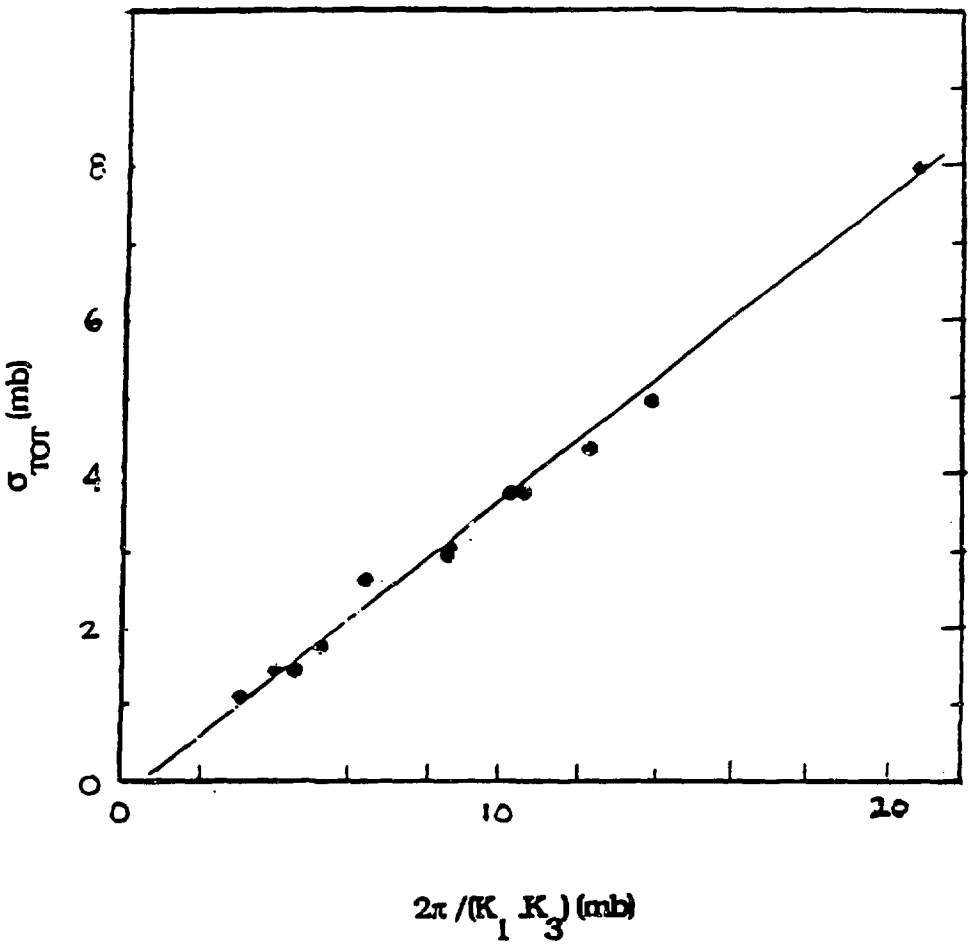

Figure 36 σ_{TOT} vs. $2\pi/(K_1 . K_3)$

level of the final results. This was in addition to systematic errors discussed below.

The estimated errors in the yields include uncertainty in the peak area due to uncertainty in the peak shape or the limits defined for the peak, as well as the uncertainty due to the amount of the background that was subtracted from under the peak. The beam polarization used in the A(θ) calculation was the average polarization weighted by the current monitor scalar, for each of the runs used in each measurement at each angle. The estimated error in the average polarization encompassed all individual polarizations used in the average along with the individual estimated errors. Individual polarizations estimated errors were taken from "accidental" rates as described in Chapter 2, section I B 3 according to this equations;

$$\Delta Ln = \sqrt{Ln + 2*AccLn} \qquad \Delta Rn = \sqrt{Rn + 2*AccRn}$$

$$\Delta Lr = \sqrt{Lr + 2*AccLr} \qquad \Delta Rr = \sqrt{Rr + 2*AccRr}$$

$$\Delta P = \left(\sqrt{\left(\frac{\Delta Ln}{Ln}\right)^2+\left(\frac{\Delta Rn}{Rn}\right)^2+\left(\frac{\Delta Lr}{Lr}\right)^2+\left(\frac{\Delta Rr}{Rr}\right)^2}\right) \frac{r}{(r+1)} \frac{1}{AP} \qquad (39)$$

where r is the asymmetry ratio given in Equation 25.

Other possible sources of error included systematic errors due to the ^{7}Li normalization and uncertainties in the integrated beam current. Systematic errors in the total integrated beam current would have only affected the results for cross sections. These errors were eliminated with the normalization to ^{7}Li as discussed in Chapter 3, section II D. Relative errors in the beam current integration would effect the analyzing power measurements.

Values of the errors used are shown in Tables 3 and 5 in Chapter 4. All factors were combined so that the total errors were computed by

$$d\sigma = \sigma\sqrt{\frac{1}{Y_n}+\frac{1}{Y_r}+\frac{2B_n}{Y_n^2}+\frac{2B_r}{Y_r^2}+\frac{dY_n}{Lt_nQ_n}+\frac{dY_r}{Lt_rQ_r}} \qquad (40)$$

and

$$dA = \sqrt{\left(\frac{A}{1-R}\right)^4(P_n-P_r)^2R^2\frac{d\sigma}{\sigma}+\left(\frac{A}{RP_r-P_n}\right)^2(dP_n^2+dP_r^2)} \qquad (41)$$

Here, B_n (B_r) are the subtracted backgrounds in normal (reverse) spin, dP_n (dP_r) are the error in normal (reverse) polarizations and R is the dead-time and efficiency normalized ratio of the normal and reverse yields. The final uncertainties are shown in Tables 4 and 6 in at the end of the chapter.

The values used to calculate the cross section and analyzing power at 200 MeV are shown in Table 3. Those used for the 494 MeV calculations are shown in Table 5. The final values for cross section and analyzing power are given in Tables 3 and 5 for 200 MeV and 494 MeV respectively.

The 7° point shows the analyzing power value from the highest confidence method of data analysis. The lower limit of the error bar represents the extreme case of background subtraction where peak shape is ignored. The upper limit represents the other extreme i.e., only a small linear background. By noting the energy spectra for $^{15}N(p,n)^{15}O$ with spin in the normal and reverse direction in Figures 37A and 37B along with the two superimposed in Figure 37C, no asymmetry

beyond the noise level is seen in the spectra and as there is no strong disparity in other factors and seen in Table 5, one expects the analyzing power to be near zero. The $^{15}N(p,n)^{15}O$ reaction at 494 MeV will not make a good polarized neutron target as the anticipated analyzing power did not appear.

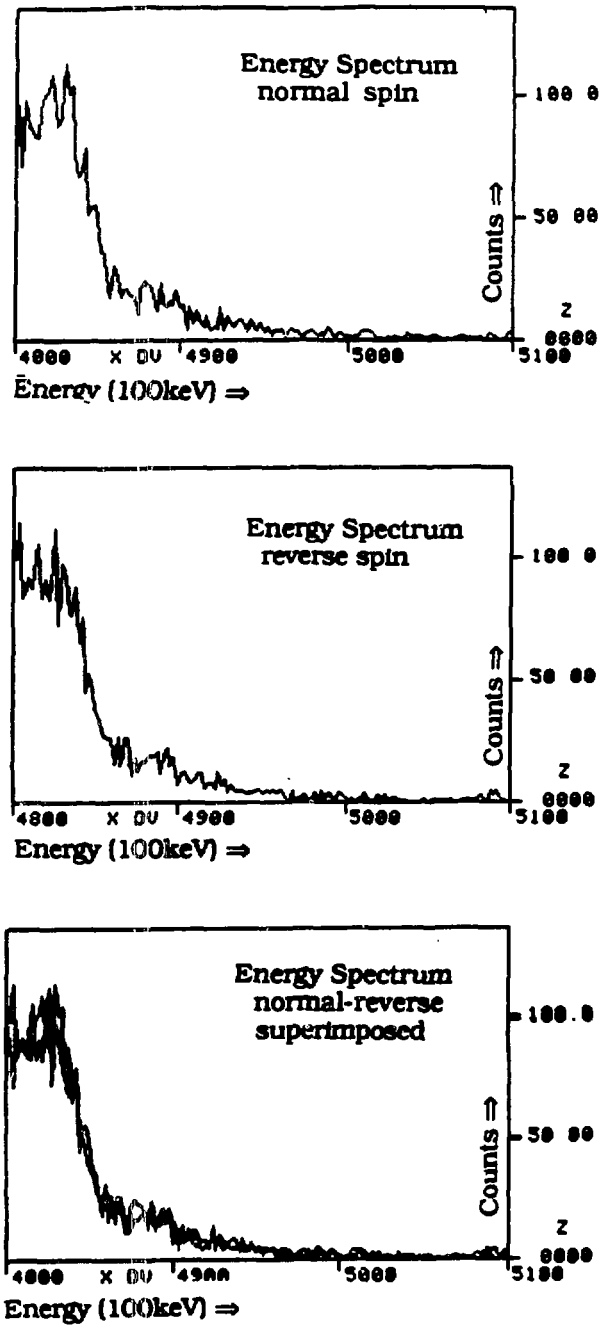

Figure 37
$^{15}N(p,n)^{15}O(g.s.)$ 7° Energy spectra

Table 3

15N(p,n)15O(g.s.)
200.

Θ_{LAB}	$Y_{n/r}$	$\Delta Y_{n/r}$	$B_{n/r}$	$Q_{n/r}$	$\mu_{n/r}$	$P_{n/r}$	$\Delta P_{n/r}$
0.0	5788	82	451	13.49	0.884	0.70	0.02
	4470	72	360	12.96	0.702	-.73	0.02
6.0	13073	125	1635	66.30	0.753	0.73	0.02
	11192	118	1840	64.94	0.678	-.74	0.02
9.3	7771	104	2419	106.9	0.760	0.73	0.02
	6347	98	2556	105.1	0.717	-.74	0.02
12.0	5226	110	6218	241.4	0.861	0.73	0.02
	3900	108	6649	238.9	0.837	-.74	0.02
15.1	623	89	6009	214.2	0.841	0.72	0.02
	972	82	6728	212.5	0.818	-.73	0.02
18.1	403	62	2813	111.2	0.864	0.72	0.02
	782	68	3018	109.1	0.848	-.73	0.02

Table 4

Ep = 200.0 MeV 15N(p,n)15O(g.s.)

thetLAB	thetCM	qCM	sigCM	dsig	Ay	dA
0.0	0.00	0.029	0.114E-01	0.231E-03	0.009	0.015
6.0	6.49	0.342	0.141E-02	0.183E-04	-0.020	0.010
9.3	10.05	0.528	0.345E-03	0.592E-05	-0.086	0.015
12.0	12.97	0.680	0.335E-04	0.727E-06	-0.172	0.028
15.1	16.31	0.854	0.686E-05	0.392E-06	0.326	0.143
18.1	19.54	1.021	0.213E-04	0.147E-05	0.465	0.135

Table 5

$^{15}N(p,n)^{15}O(g.s.)$
500.

Θ_{LAB}	$Y_{n/r}$	$\Delta Y_{n/r}$	$B_{n/r}$	$Q_{n/r}$	$\mu_{n/r}$	$P_{n/r}$	$\Delta P_{n/r}$
0.0	2885	55	117	1.880	0.963	0.72	0.03
	2819	54	89	1.798	0.963	-.72	0.03
1.0	1738	42	17	1.220	0.911	0.71	0.03
	1732	42	12	1.224	0.913	-.71	0.03
2.0	1077	35	69	.9190	0.899	0.71	0.03
	1028	35	73	.9395	0.902	-.71	0.03
3.0	1526	39	22	1.794	0.886	0.71	0.03
	1559	40	19	1.869	0.885	-.71	0.03
4.0	1276	40	105	2.141	0.878	0.72	0.03
	1313	42	129	2.197	0.876	-.72	0.03
5.0	781	30	75	2.215	0.866	0.65	0.03
	707	28	72	2.100	0.870	-.65	0.03
7.0	166	14	41	2.635	0.862	0.67	0.03
	168	14	54	2.476	0.868	-.67	0.03
9.0	70	11	43	6.828	0.898	0.74	0.03
	88	12	41	7.358	0.897	-.74	0.03
10.2	26	6	8	1.715	0.903	0.71	0.03
	36	7	8	1.563	0.902	-.71	0.03
11.0	135	16	108	5.917	0.872	0.78	0.03
	204	17	70	5.952	0.871	-.78	0.03
12.5	225	16	38	7.316	0.865	0.77	0.03
	319	19	43	7.559	0.860	-.77	0.03
14.0	211	17	99	6.662	0.818	0.76	0.03
	268	18	32	6.440	0.818	-.76	0.03
16.0	174	15	56	8.994	0.806	0.75	0.03
	246	18	54	8.211	0.823	-.75	0.03
18.0	86	11	42	6.975	0.898	0.77	0.03
	75	11	44	6.799	0.902	-.77	0.03

Table 6

Ep = 500.0 MeV 15N(p,n)15O(g.s.)

thtLAB	thtCM	qCM	sigCM	dsig	Ay	dAy
0.0	0.0	0.020	0.364E+01	0.122E+00	0.014	0.019
1.0	1.1	0.098	0.345E+01	0.145E+00	-0.006	0.023
2.0	2.2	0.194	0.274E+01	0.157E+00	-0.049	0.032
3.0	3.3	0.289	0.204E+01	0.911E-01	-0.013	0.025
4.0	4.4	0.385	0.145E+01	0.769E-01	0.003	0.029
5.0	5.5	0.481	0.837E+00	0.577E-01	-0.038	0.042
7.0	7.7	0.673	0.159E+00	0.255E-01	-0.163	0.203
9.0	9.9	0.865	0.260E-01	0.711E-02	0.102	0.152
10.2	11.2	0.980	0.444E-01	0.170E-01	0.283	0.226
11.0	12.1	1.056	0.687E-01	0.132E-01	0.252	0.100
12.5	13.7	1.199	0.889E-01	0.105E-01	0.202	0.062
14.0	15.4	1.342	0.942E-01	0.130E-01	0.174	0.075
16.0	17.6	1.532	0.635E-01	0.930E-02	0.267	0.079
18.0	19.8	1.721	0.272E-01	0.723E-02	-0.073	0.144

CHAPTER 4

RESULTS AND CONCLUSIONS

The experimental results will now be examined. The final data shall be put into context with existing data as well as compared with both RIA and non-relativistic DWIA calculations. Conclusions are drawn concerning the theoretical usefulness of the data and the suitability of ^{15}N as a polarized neutron production target.

I RESULTS

I A CROSS SECTIONS

Energy spectra for $^{14}C(p,n)^{14}N$, 0° at 60-200 MeV are shown in Figure 38. These spectra clearly show that the cross section of the 0^+ state becomes smaller with the increase in energy with respect to the 1^+ state cross section. From these spectra, estimates of the relative strength $|J_{\sigma\tau}/J_\tau|$ in this energy range were obtained by Tadduecci[41];

$$R \equiv \left(\frac{J_{\sigma\tau}}{J_\tau}\right) \cdot \left(\frac{N_{\sigma\tau}}{N_\tau}\right)^{1/2} = \frac{E_p}{55.4 \pm 1.4 \text{ MeV}}$$

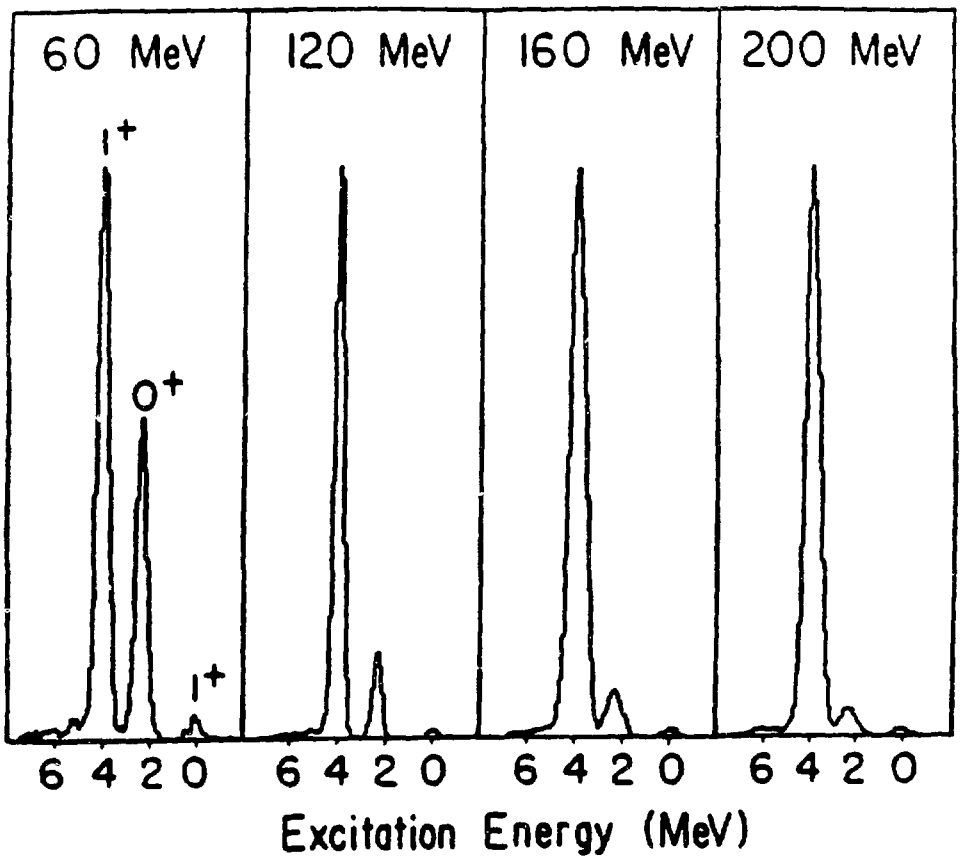

Figure 38 Energy spectra of $^{14}C(p,n)^{14}N$ Gamow-Teller and Fermi transitions at 60 MeV-200 MeV.

where $N_{\sigma\tau}(N_\tau)$ is a distortion factor (i.e., the ratio of distorted-waves to plane-waves cross sections) for the GT (Fermi) transition and E_p is the incoming proton energy. These and other data are compared with a theoretical estimate based on NN phase shifts in Figure 39.

The $^{14}C(p,n)$ 0^+ state and 1^+ state zero degree cross sections are related by[42]:

$$\left.\frac{d\sigma}{d\Omega}\right|_{0^\circ} \propto K(E_p)N_\tau (J_\tau)^2 B(F) + N_{\sigma\tau}(J_{\sigma\tau})^2 B(GT) \quad . \qquad (55)$$

Here, B(F) and B(GT) are the reduced Fermi and GT transition probabilities, respectively. Alternately[41]:

$$\sigma(q,\omega) = \hat{\sigma}_\tau F_o(q,\omega)\, B(F) + \hat{\sigma}_{\sigma\tau} F_1(q,\omega)\, B(GT) \qquad (56)$$

where $F_o(q,\omega)$ and $F_1(q,\omega)$ are the momentum transfer (q) and energy loss profile functions (ω) and $\hat{\sigma}_\tau$ and $\hat{\sigma}_{\sigma\tau}$ are the Fermi and GT unit cross sections. The interaction strengths may thus be derived from the measured ratio of unit cross sections. Love at. al[43] found that such measurements are sensitive to the density dependence of the Fermi term.

For a mixed transition such as $^{13}C(p,n)^{13}N(g.s.)$ and $^{15}N(p,n)^{15}O(g.s.)$, the extraction of the $|J_{\sigma\tau}/J_\tau|$ ratio is complicated but a method proposed by Taddeucci et. al.[41,44] has been successful at energies below 200 MeV. In this way, the $^{13}C(p,n)^{13}N(g.s.)$ and $^{15}N(p,n)^{15}O(g.s.)$ 0° cross sections can be used to constrain the interaction strength in the 500 MeV region.

The differential cross sections found for the $^{15}N(p,n)^{15}O(g.s.)$ reaction at 200 MeV and 494 MeV are shown in Figures 40 and 41 respectively. The dashed line in the figures

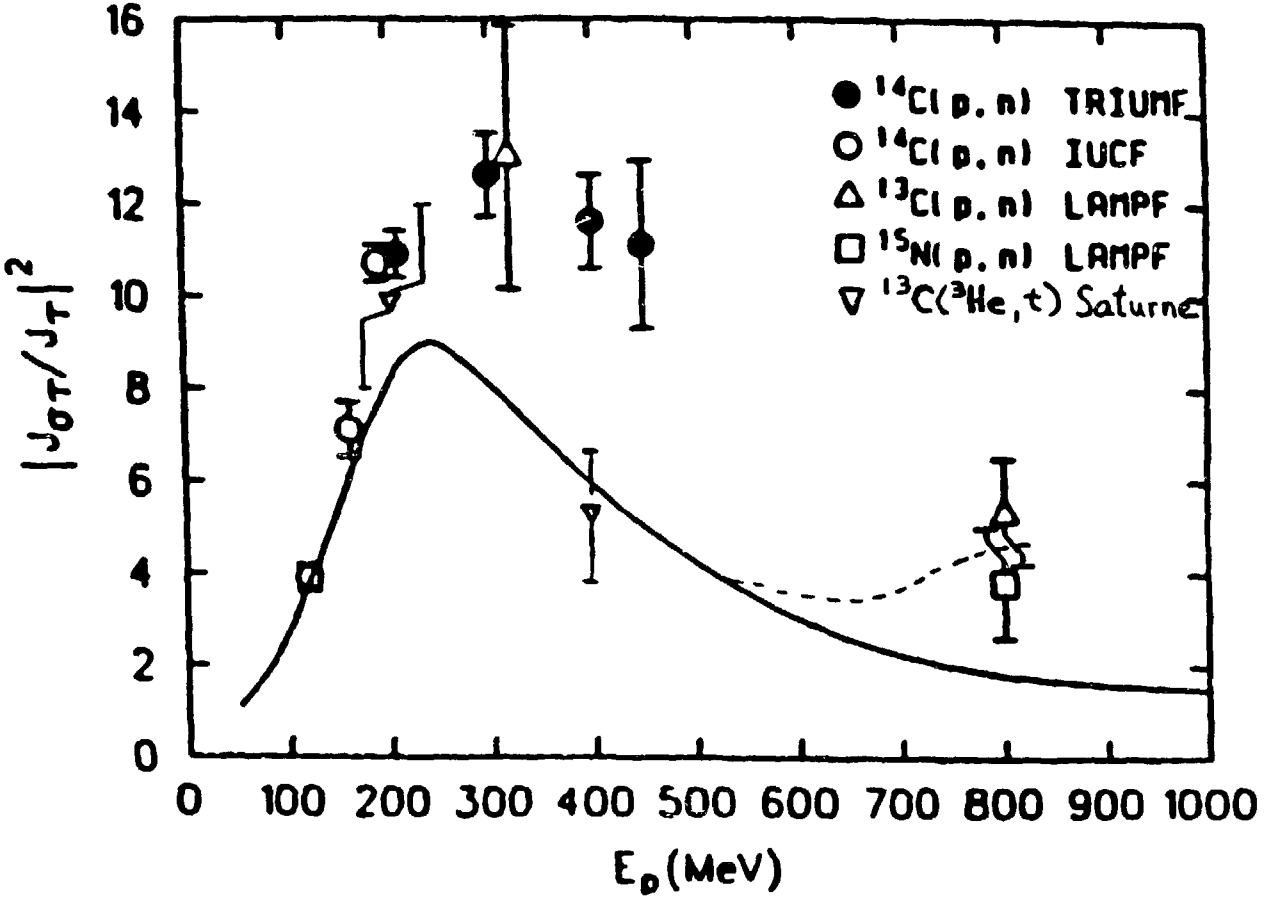

Figure 39. Values of the interaction strength ration deduced from cross section measurments at IUCF, TRIUMF, LAMPF and SATURNE.

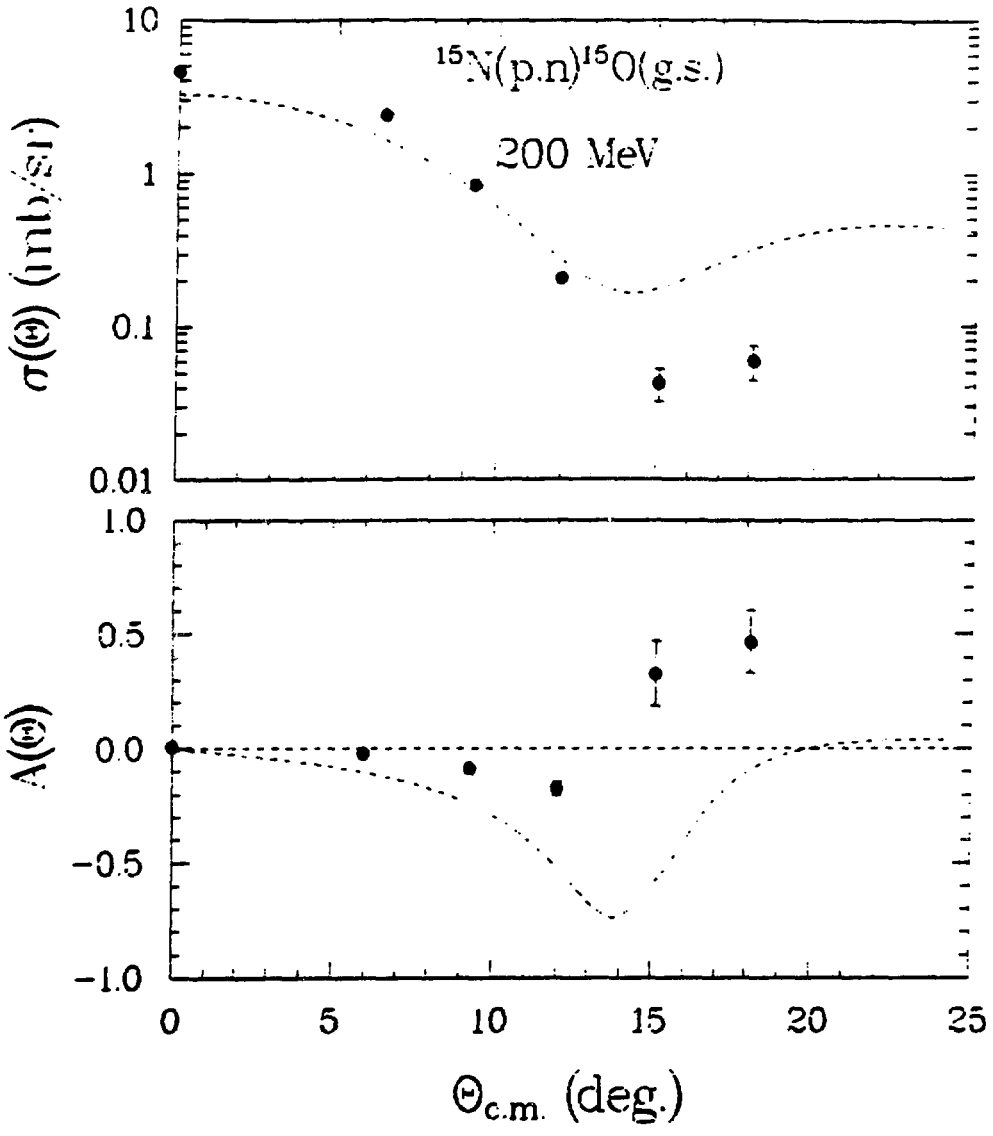
^{15}N(p,n)^{15}O(g.s.)
200 MeV
σ(Θ) (mb/sr)
10
1
0.1
0.01
A(Θ)
1.0
0.5
0.0
−0.5
−1.0
0
5
10
15
20
25
Θc.m. (deg.)

Figure 40

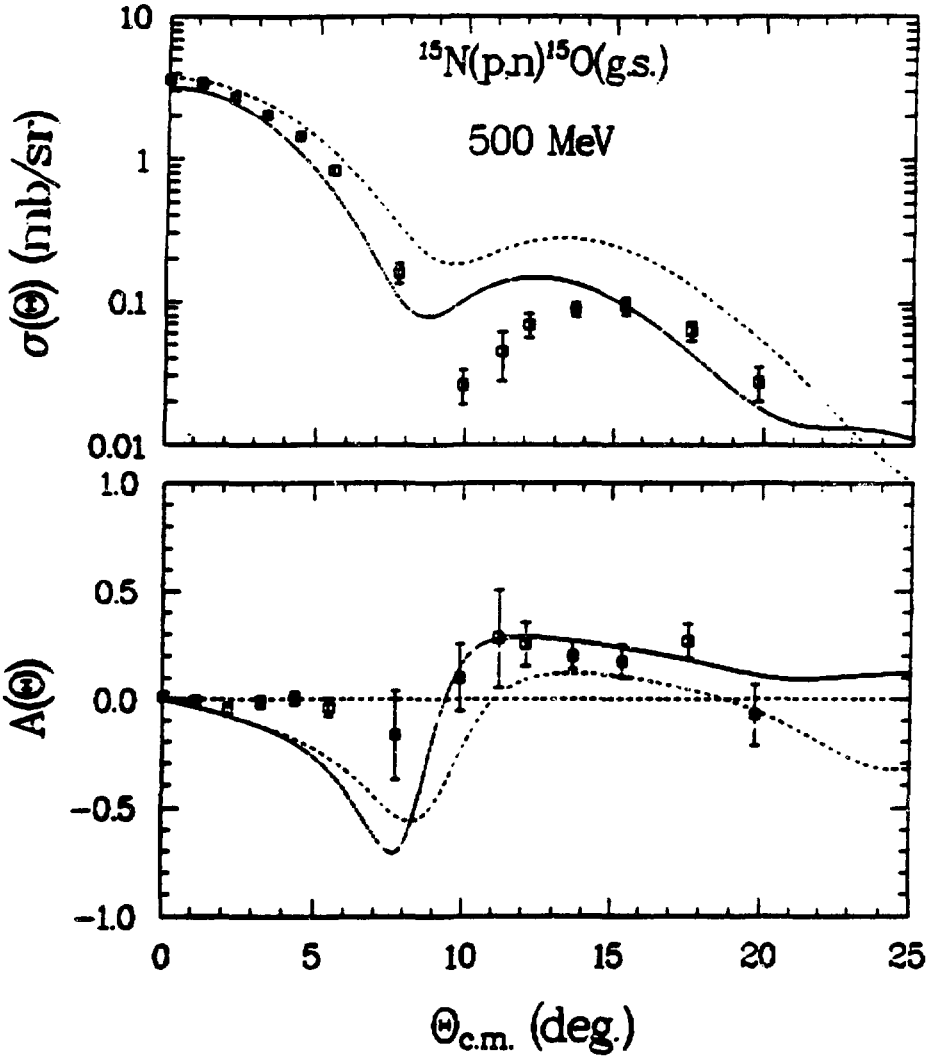
^{15}N(p,n)^{15}O(g.s.)
500 MeV
σ(Θ) (mb/sr)
A(Θ)
Θc.m. (deg.)
10
1
0.1
0.01
1.0
0.5
0.0
−0.5
−1.0
0
5
10
15
20
25

Figure 41.

represents DWIA calculations. The DWIA calculations, discussed below, at 200 MeV and 494 MeV determine the 0° strength fairly well but fail in predicting the minimum and the second maximum. The RIA calculation, provided by Shepard[6,45], in Figure 41 is represented by a solid line. It predicts the 0° strength fairly well, fails to predict the second maximum and over-estimates the angular position of the first minimum by a few degrees. The RIA calculation does come close to an acceptable fit to the slope of the first maximum of the 494 MeV $^{15}N(p,n)^{15}O$ cross section. This is important as a correct prediction helps to provide sensitive tests to distortion effects and medium corrections.

The program used for the DWIA calculations, DW81[46], assumes an explicit form of the NN transition amplitude and calculates exactly a nucleon-nucleus transition amplitude. The potentials consist of radial Yukawa potentials for all but the tensor potential which is an r^2 times a Yukawa potential. The two nucleon interaction strengths were taken from Franey and Love[47]. The optical potential used was a phenomenological optical potential. It was derived for the proton elastic scattering data of Jones[48]. The relative amplitudes for the transitions between single particle orbitals used were derived from Cohen and Kurath[49,50]. The Gamow-Teller transition's contribution to the pure $(^1/_2,^1/_2)$ was renormalized down to fit β decay strengths as shown by Taddeucci et al.[41]. This new normalization and its effects on other states gave the final relative amplitudes used.

I B ANALYZING POWERS

The analyzing powers in Figure 42 are for $^{13}C(p,n)^{13}N(g.s.)$ at 160 MeV by Rapaport et. al.[51], $^{13}C(p,n)^{13}N(g.s.)$ and

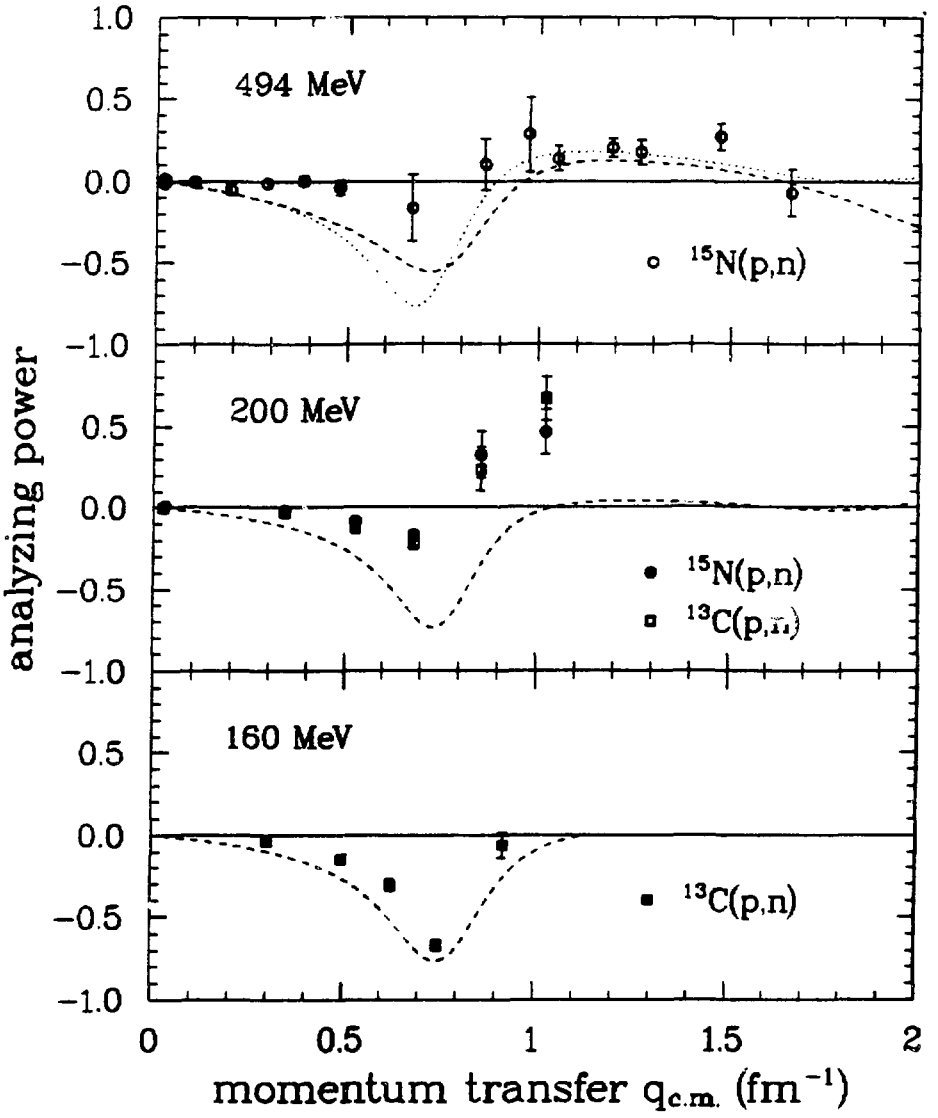
494 MeV
200 MeV
160 MeV
^{15}N(p,n)
^{15}N(p,n)
^{13}C(p,n)
^{13}C(p,n)
analyzing power
momentum transfer $q_{c.m.}$ (fm^{-1})
1.0
0.5
0.0
−0.5
−1.0
0
0.5
1
1.5
2

Figure 42.

$^{15}N(p,n)^{15}O(g.s.)$ at 200 MeV and $^{15}N(p,n)^{15}O(g.s.)$ at 494 MeV. The dashed lines represent DWIA calculations as shown above. The dotted line represents an RIA calculation provided by Shepard[45]. The $^{13}C(p,n)^{13}N(g.s.)$ 160 MeV data are fit reasonably well by the DWIA calculations. The data for the similar transitions $^{13}C(p,n)^{13}N(g.s.)$ and $^{15}N(p,n)^{15}O(g.s.)$ follow the same trend as the energy increases to 200 MeV. The DWIA calculation fails to predict the amplitude of the analyzing power. The analyzing power data for the $^{15}N(p,n)^{15}O(g.s.)$ reaction at 494 MeV are not predicted by the associated DWIA calculation or RIA calculation.

It is noteworthy that the analyzing power goes through a large change from 160 MeV to 494 MeV but the DWIA calculation for this energy range does not. At 200 MeV, the DWIA prediction has failed. This marks the start of the region where DWIA predictions of reactions of this type have broken down. As relativistic processes are generally inconsequential below the 500 MeV region, and above the 800 MeV region other effects such as medium modifications become inconsequential, these intermediate energies are important as transitional regions where some processes are starting while others are stopping.

The failure of the DWIA calculations at energies of 200 MeV and above might have been expected as DWIA calculations failed to predict analyzing powers for proton elastic scattering at medium energies. The fact that the RIA calculation follows the same trend suggests that the failure of these two models is not due to relativistic effects.

The total analyzing power measured has contributions from both the Gamow-Teller and the Fermi transitions. Calculations by Horowitz[52] and by Love et al.[43] have suggested that nuclear medium effects might suppress the Fermi contribution. The

Fermi contribution to the analyzing power was suppressed to fit the data in the .7 fm^{-1} region. A good agreement with the data was achieved when the Fermi term was suppressed to 5% of its original magnitude. This suppression is much larger than can be expected from the proposed density effects which predict a 5% effect. As it suggests a near total extinguishing of the Fermi contribution, this should be considered to be a failure of the model used.

It has been discussed how the (p,n) reaction should show whether the pseudoscalar or the pseudovector form of the portion of the exchange dominated by one pion exchange should be used. Figure 43 shows some sensitivity RIA calculations by Ray and Shepard[5] of the $^{13}C(p,n)$ reaction where the pseudovector term and the pseudoscalar terms are used separately. It also shows a non-relativistic calculation with the pseudoscalar term. The three curves are qualitatively the same, the difference being the relative amplitudes. Recall that Horowitz[7] and Tjon and Wallace[8] received more success with the pseudovector term, but here the relativistic pseudoscalar term has the lower amplitude and would best fit the data. This is due to the relativistic pseudoscalar cross section being significantly larger than the other cross sections and as the analyzing power is divided by the cross section to normalize the asymmetry yields, the relativistic pseudoscalar analyzing power is smaller. As the analyzing power is approximately zero at the forward angles, it is qualitatively different from the predictions and this measurement should not be interpreted as reason to choose the pseudoscalar form over the pseudovector form. As pointed out by Ray and Shepard[5], sensitivity to this difference is more discernable in spin depolarization measurements.

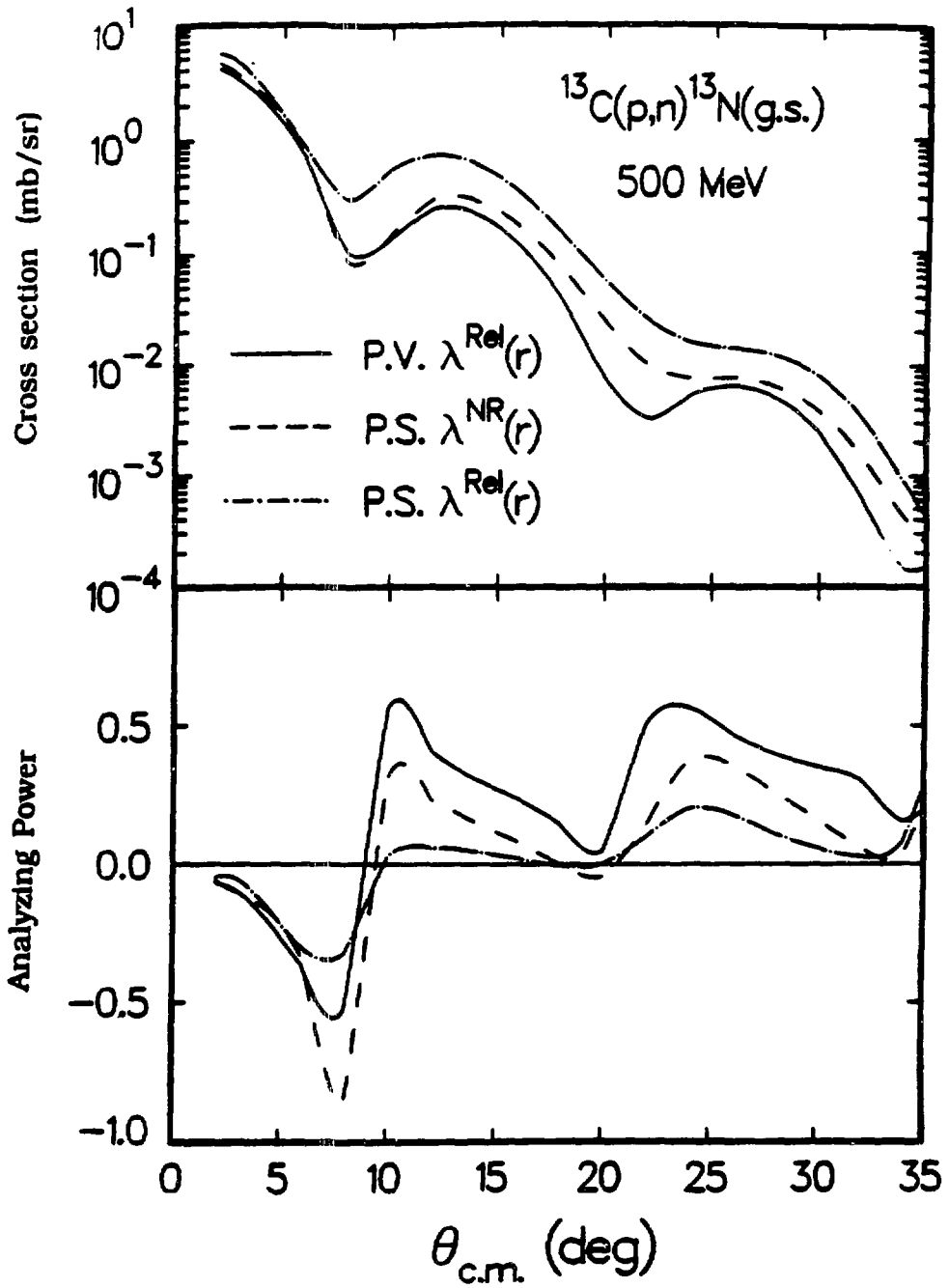

Figure 43 RIA predictions for 500 MeV 13C(p,n)13N(g.s.) differential cross sections and analyzing power using relativistic pseudovector, relativistic pseudoscalar, and non-relativistic pseudoscalar forms.

I C POLARIZED NEUTRON PRODUCTION TARGET

The $^{15}N(p,n)^{15}O(g.s.)$ analyzing power has a low magnitude in the $\vartheta_{cm}=7°$, $q_{cm}=0.7$ fm^{-1} region at 494 MeV. The FOM, as defined in Chapter 1, was calculated with the RIA prediction of Shepard[5]. The calculation is shown along with the measured FOM in Figure 44. The peak in the calculation in the 7° region shows where the target would have been most useful as a polarized neutron production target. The measured FOM in this region is flat. As the absolute value of the analyzing power is minimal in the "flat" region, ^{15}N would not make a suitable polarized neutron production target in the 500 MeV region.

II CONCLUSIONS

The resolution of the energy spectra of $^{13}C(p,n)^{13}N$ and $^{15}N(p,n)^{15}O$ at 494 MeV shown in Figure 33, exemplify the experimental desirability of ^{15}N over ^{13}C. The ground state and the first excited state of the $^{15}N(p,n)^{15}O$ reaction are separate and distinct in the spectrum where as the $^{13}C(p,n)^{13}N$ states are not. The resolution in the $^{15}N(p,n)^{15}O$ reaction spectrum shows that the commissioning of the new NTOF facility was a success in that short flight paths on the order of 82 m and thick targets on the order of $700\ mg/cm^2$ can give acceptable resolution. Even better resolutions can be achieved with longer flight paths and thinner targets.

The cross sections and analyzing powers measured could not be fit by DWIA calculations nor by RIA calculations. Proposed corrections were either too weak to explain the difference between prediction and measurement or too strong so as to be unrealistic.

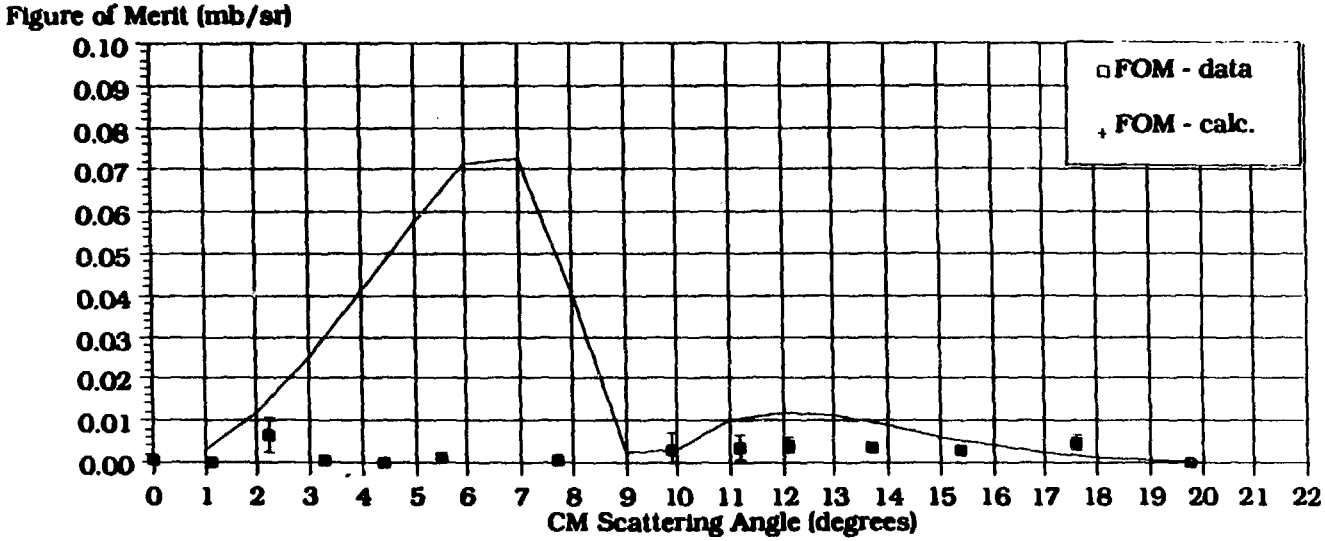

Figure 44 Calculated and measured Figure of Merit

Cross sections and analyzing powers are influenced by many terms within the models. Work in both theoretical and experimental areas needs to be done in order to understand the reactions involved. Spin transfer experiments should be done which will constrain specific parts of the interaction so that the present data can be better analyzed. More realistic interactions need to be included in RIA calculations, such as those given by Tjon and Wallace[53], so that the model can be given in terms which are meaningful.

APPENDIX A

DERIVATION OF OBSERVABLES

APPENDIX A

Derivation of Observables

The scattering of two spin $^1/_2$ particles is described by the scattering matrix;

$$M(\vec{\sigma_1},\vec{\sigma_2},\vec{k_1},\vec{k_2}) \ , \tag{1A}$$

where $\vec{\sigma_1}(\vec{\sigma_2})$ is the spin operator for the first (second) particle and $\vec{k_1}(\vec{k_2})$ is the center of mass momentum for the first (second) particle. By requiring invariance of the scattering matrix under spatial rotation, reflection and time reversal, it can be written as:

$$M = A + B(\vec{\sigma_1}_n \cdot \vec{\sigma_2}_n) + C(\vec{\sigma_1}_n + \vec{\sigma_2}_n) + E\vec{\sigma_1}_q \cdot \vec{\sigma_2}_q + F\vec{\sigma_1}_p \cdot \vec{\sigma_2}_p \ , \tag{2A}$$

where A, B, C, E and F are complex functions of the center of mass energy and the scattering angle. The isovector terms are implicitly assumed. We now define the momentum transfer q^2:

$$q^2 = 2p_{cm}^2 \ (1-\cos\theta_{cm}) \ , \tag{3A}$$

and our coordinate system unit vectors;

$$\hat{p} = \frac{\vec{k_i} + \vec{k_f}}{|\vec{k_i} + \vec{k_f}|}, \quad \hat{q} = \frac{\vec{k_i} - \vec{k_f}}{|\vec{k_i} - \vec{k_f}|}, \quad \hat{n} = \frac{\vec{k_i} \times \vec{k_f}}{|\vec{k_i} \times \vec{k_f}|} \ . \tag{4A}$$

We note that $\hat{p}$ is along the direction of the outgoing nucleon, $\hat{n}$ is perpendicular to the scattering plane, and $\hat{q}$ is orthonormal to both $\hat{p}$ and $\hat{n}$.

The mixture of possible spin states of the two nucleon system is defined by the density matrix ρ:

$$\rho_I = |\chi_n\rangle\langle\chi_n| \tag{5A}$$

and :

$$\rho_S = \Sigma_n |\chi_n\rangle P_n \langle\chi_n| \quad , \qquad \chi = \sqrt{\frac{1}{N}}\Sigma_{j=1}\chi_j \ , \tag{6A}$$

for mixed states where P_n is the relative probability of finding the system in state χ_n. This density matrix describes the system in that it links the initial spin state of the system χ_n with the final spin of the scattering state or;

$$\Sigma_n F_{mn}(\theta,\phi)|\chi_m\rangle = M|\chi_n\rangle \ , \tag{7A}$$

where the scattered state wave function has the asymmetric form of;

$$\Psi \equiv e^{i\vec{q}\cdot\vec{r}}|\chi_n\rangle + \frac{e^{i\vec{q}\cdot\vec{r}}}{r}\Sigma_m F_{mn}(\theta,\phi)\,|\chi_m\rangle \ . \tag{8A}$$

The expectation value for an operator $\mathbf{0}$ of the state χ is written in terms of ρ by:

$$\langle\mathbf{0}\rangle = \Sigma_n \langle\chi_n|\mathbf{0}|\chi_n\rangle = \Sigma\langle\chi|\mathbf{0}\rho|\chi\rangle$$

$$\langle O \rangle = \mathrm{Tr}(O\rho). \tag{9A}$$

The differential cross section, $\sigma(\theta)$, is defined by:

$$\sigma(\theta)_i = dN \frac{r^2}{A} \frac{1}{F_I} , \tag{10A}$$

where r is the distance between the scattering center and the detector, A is the area detected, F_I is the incident flux and dN is the change in particle number such that dN/A is the flux scattered through area A. Differential cross section can be written as;

$$\sigma(\theta)_i = r^2 \frac{F_S}{F_I} . \tag{11A}$$

The particle flux described quantum mechanically as the probability-density current, is given by Merzbacher for position r, wave function φ and reduced mass μ by;

$$\text{"Flux"} = \frac{\hbar}{2\mu i}[\Psi^*(\vec{r})\nabla_{\vec{r}}\{\Psi(\vec{r})\} - \Psi(\vec{r})\nabla_{\vec{r}}\{\Psi^*(\vec{r})\}] , \tag{12A}$$

so that

$$|F_I| = \frac{\hbar k}{\mu} C^\dagger C \phi_{gs}^\dagger \phi_{gs} \chi_i^\dagger \chi_i , \tag{13A}$$

$$|F_s| = \frac{\hbar k}{\mu} C^\dagger C \phi_{gs}^\dagger \phi_{gs} \chi_s^\dagger \chi_s , \tag{14A}$$

where the incident proton spin state is normalized to unity:

$$\sigma(\theta) = \chi_s^{\dagger}\chi_s = |\chi_s|^2 . \qquad (15A)$$

We can combine equations 5A and 15A to give:

$$\sigma(\theta) = Tr(\rho_s) . \qquad (16A)$$

We expand the density matrix in terms of the Pauli spin matrixes and use equation 9A to determine the coefficients for σ_i;

$$\rho_i = \frac{1}{2}(I + \sum_{i=1}^{3} p_i \cdot \sigma_i) = \frac{1}{2}(I + \vec{P_b} \cdot \vec{\sigma}) \qquad (17A)$$

where

$$\sigma_1 = \begin{pmatrix} 0 & 1 \\ 1 & 0 \end{pmatrix}, \qquad \sigma_2 = \begin{pmatrix} 0 & i \\ -i & 0 \end{pmatrix}, \qquad \sigma_3 = \begin{pmatrix} 1 & 0 \\ 0 & -1 \end{pmatrix} . \qquad (18A)$$

Analyzing power is defined as:

$$A(\theta) = \frac{Tr(M\sigma_i M^{\dagger})}{Tr(M M^{\dagger})} \qquad (19A)$$

and for an unpolarized beam;

$$\sigma_o(\theta) = \sigma_o(\theta) = \frac{1}{2}Tr(M M^{\dagger}) , \qquad (20A)$$

which becomes:

$$\sigma(\theta) = \sigma_o(I + \sum_{i=1}^{3} p_i \cdot A_i(\theta)) . \qquad (21A)$$

The final density matrix in terms of the Pauli spin matrixes is defined by:

$$\rho_f = \Sigma_n M|\chi_n\rangle P_n \langle\chi_n| M^\dagger = M\rho_i M^\dagger \tag{22A}$$

or when Tr ρ = 1;

$$\rho_f = \frac{M\rho_i M^\dagger}{Tr(M\rho_i M^\dagger)} \tag{23A}$$

is used to represent the mixture of states. The final spin state is given by;

$$p_f = \frac{\langle\rho_i\sigma_i\rangle}{\langle\rho_i\rangle} \quad . \tag{24A}$$

and using equations 17A and 22A, we have;

$$p_j = \frac{\frac{1}{2}\left(Tr(MM^\dagger\sigma_i) + \sum_{i=1}^{3} Tr(Mp_i\sigma_i M^\dagger\sigma_j)\right)}{Tr(M\,M^\dagger)} \quad . \tag{25A}$$

We define the polarization;

$$P_j(\theta) = \frac{(Tr(MM^\dagger\sigma_i))}{Tr(M\,M^\dagger)} \tag{26A}$$

and spin parameters;

$$D_{ij}(\theta) = \frac{Tr(M\sigma_i M^{\dagger}\sigma_j)}{Tr(M\,M^{\dagger})} \quad . \tag{27A}$$

so that;

$$p_j = \frac{\sigma_o(\theta)}{\sigma(\theta)}\left(P_j(\theta) + \sum_{i=1}^{3} p_i D_{ij}(\theta)\right) \quad . \tag{28A}$$

Where the incoming polarization is normal to the scattering plane, this becomes;

$$p_j = \frac{P(\theta) + p_I D_{nn}(\theta)}{1 + p_I A(\theta)} \quad . \tag{29A}$$

APPENDIX B

HISTOGRAM FILE

```
; SIGAY.HST
;
; TEST DESCRIPTOR FILE: SIGAY.TST
;
; PURPOSE: REPLAY OF NTOFC50 DATA
;          CROSS SECTION AND ANALYZING POWER
;
; LAST MODIFIED: 02-FEB-88 (TNT)
;
/DE:ALL
/BL:1/OV:-1/DF
;
; MULTIPLICITY
;
/X:-10:110/BI:5/DF
;
MULT1/IN:501/TE:83
MULT2/IN:502/TE:84
MULT3/IN:503/TE:85
;
; CELL HIT FREQUENCY -- PH GATED
;
CELLA0/IN:505/TE:130
CELLC0/IN:506/TE:131
CELLC1/IN:507/TE:132
;
; POSITION
;
/X:-1000:1000/BI:5/TE:166/DF
;
XTMNA0/IN:527
XTMNC0/IN:528
YTMNC1/IN:532
;
XDFNA0/IN:521
XDFNC0/IN:522
XDFNC1/IN:523
;
RAD1/IN:586/X:0:1000
;
; PULSE-HEIGHT
;
/X:0:3000/BI:5/DF
;
; NEUTRAL SINGLES
;
PHA0NS/IN:524/TE:107
PHC0NS/IN:525/TE:108
PHC1NS/IN:526/TE:109
;
; NN + NP COINCIDENCES
;
PHA0NC/IN:524/TE:103
PHC0NC/IN:525/TE:103
PHC1NC/IN:526/TE:103
```

```
;
; VELOCITY BETWEEN PLANES
;
/IN:590/X:0:2000/BI:10/DF
;
VSCTNN/TE:100
VSCTNP/TE:101
VSCTPP/TE:102
;
; VELOCITY RATIO
;
/IN:591/X:0:3000/BI:10/DF
;
VRATNN/TE:100
VRATNP/TE:101
VRATPP/TE:102
;
; RAW RF SPECTRA
;
/IN:001/X:0:2000/BI:2/DF
;
RFCOIN/TE:35
RFSING/TE:38
;
; TIME-OF-FLIGHT
;
/IN:533/X:3200:4200/BI:1/DF
;
TOFGAM/TE:165
TOFNEU/TE:162
;
; KINETIC ENERGY
;
/IN:581/X:4000:5100/BI:2/DF
;
; NEUTRAL SINGLES
;
ENP1NS/TE:150
ENP2NS/TE:151
ENP3NS/TE:152
;
ENNS/TE:153
ENNSN/TE:154
ENNSR/TE:155
;
; NEUTRAL COINCIDENCES - HIGH RESOLUTION (.2 MeV)
;
ENHIC/TE:162
ENHICN/TE:163
ENHICR/TE:164
;
; NEUTRAL COINCIDENCES - LOW RESOLUTION (1 MeV)
;
/X:2000:5100/BI:10/DF
;
ENLOC/TE:162
```

```
ENLOCN/TE:163
ENLOCR/TE:164
;
```

APPENDIX C

TEST FILE

```
; SIGAY.TST
;
; PURPOSE:    FOR CROSS SECTION + ANALYZING POWER REPLAY
;
; MODIFIED:  05-FEB-88 (TNT) FOR REPLAY OF C50 DATA
;
/TE:250/BL:2/IB:10/IG:10
;
BLOCK,1
;
;************** TESTS ON RAW DATA WORDS **********************************
;
; POLARIZATION
;
01,GATE,151,500,1500          ;NORMAL
02,GATE,152,500,1500          ;REVERSE
03,IOR,1,2                    ;N+R
;
; RF STOP TESTS
;
05,GATE,01,1060,1230          ;WINDOW ON RAW RF STOP
;
; TRIGGER "BIT" TESTS
;
10,GATE,02,50,1500            ;EPMON  TRIGGER
11,GATE,03,50,1500            ;NTMON  TRIGGER
12,GATE,04,855,1055           ;NNCOIN TRIGGER
13,GATE,04,1114,1314          ;NPCOIN TRIGGER
14,GATE,04,1387,1587          ;PPCOIN TRIGGER
15,GATE,05,461,661            ;COSMIC TRIGGER
16,GATE,06,374,574            ;NSING  TRIGGER
;
; CHARGED PARTICLE PLANE 1 (CA0) "BIT" TESTS
;
20,GATE,07,200,1200           ;CA00 VALID MEAN-TIME
21,GATE,08,200,1200           ;CA01   "
22,GATE,09,200,1200           ;CA02   "
23,GATE,10,200,1200           ;CA03   "
24,GATE,11,200,1200           ;CA04   "
;
; CHARGED PARTICLE PLANE 2 (CC0) "BIT" TESTS
;
25,GATE,12,200,1300           ;CC00 VALID MEAN-TIME
26,GATE,13,200,1300           ;CC01   "
27,GATE,14,200,1300           ;CC02   "
28,GATE,15,200,1300           ;CC03   "
29,GATE,16,200,1300           ;CC04   "
;
; CHARGED-PARTICLE TESTS
;
30,IOR,20,21,22,23,24         ;CA0 HIT
31,IOR,25,26,27,28,29         ;CC0 HIT
32,AND,30,31                  ;CA0*CC0
33,AND,30,31,14               ;CA0*CC0*PPCOIN TRIGGER
;
```

```
; EVENT CLASSIFICATION BASED ON TRIGGER "BIT" TESTS
;
35,IOR,12,13,14              ;COINCIDENCE EVENT (NN + NP + PP)
36,AND,16,35                 ;FALSE "SINGLES"
37,AND,16,-35                ;TRUE  "SINGLES"
38,AND,16,-35,-32            ;TRUE NEUTRAL "SINGLES"
;
; DEFINITION OF GOOD EVENT FOR SELECTIVE REPLAY (I130 = EVTTST)
;
40,IOR,10,11,15,38           ;EPPO + NTPO + COSMIC + NSINGLES
41,IOR,12,13,14,38           ;NN + NP + PP + NSINGLES
42,AND,05,41                 ;          "             * RF WINDOW
;
;************** TESTS ON CALCULATED QUANTITIES ******************************
;
BLOCK,2
;
; PLANE 1 (NA0) "BIT" TESTS
;
50,GATE,321,200,800          ;NA00 VALID MEAN-TIME
51,GATE,322,200,800          ;NA01 VALID MEAN-TIME
52,GATE,323,200,800          ;NA02 VALID MEAN-TIME
53,GATE,324,200,800          ;NA03 VALID MEAN-TIME
54,GATE,325,200,800          ;NA04 VALID MEAN-TIME
55,GATE,326,200,800          ;NA05 VALID MEAN-TIME
56,GATE,327,200,800          ;NA06 VALID MEAN-TIME
57,GATE,328,200,800          ;NA07 VALID MEAN-TIME
58,GATE,329,200,800          ;NA08 VALID MEAN-TIME
59,GATE,330,200,800          ;NA09 VALID MEAN-TIME
;
; PLANE 2 (NC0) "BIT" TESTS
;
60,GATE,331,200,800          ;NC00 VALID MEAN-TIME
61,GATE,332,200,800          ;NC01 VALID MEAN-TIME
62,GATE,333,200,800          ;NC02 VALID MEAN-TIME
63,GATE,334,200,800          ;NC03 VALID MEAN-TIME
64,GATE,335,200,800          ;NC04 VALID MEAN-TIME
65,GATE,336,200,800          ;NC05 VALID MEAN-TIME
66,GATE,337,200,800          ;NC06 VALID MEAN-TIME
67,GATE,338,200,800          ;NC07 VALID MEAN-TIME
68,GATE,339,200,800          ;NC08 VALID MEAN-TIME
69,GATE,340,200,800          ;NC09 VALID MEAN-TIME
;
; PLANE 3 (NC1) "BIT" TESTS
;
70,GATE,341,200,800          ;NC10 VALID MEAN-TIME
71,GATE,342,200,800          ;NC11 VALID MEAN-TIME
72,GATE,343,200,800          ;NC12 VALID MEAN-TIME
73,GATE,344,200,800          ;NC13 VALID MEAN-TIME
74,GATE,345,200,800          ;NC14 VALID MEAN-TIME
75,GATE,346,200,800          ;NC15 VALID MEAN-TIME
76,GATE,347,200,800          ;NC16 VALID MEAN-TIME
77,GATE,348,200,800          ;NC17 VALID MEAN-TIME
78,GATE,349,200,800          ;NC18 VALID MEAN-TIME
79,GATE,350,200,800          ;NC19 VALID MEAN-TIME
;
```

```
; COSMIC EVENTS (MULT=10)
;
80,AND,50,51,52,53,54,55,56,57,58,59     ;NA0 COSMIC
81,AND,60,61,62,63,64,65,66,67,68,69     ;NC0 COSMIC
82,AND,70,71,72,73,74,75,76,77,78,79     ;NC1 COSMIC
;
; INCLUSIVE EVENTS: MULT = 1-10
;
83,IOR,50,51,52,53,54,55,56,57,58,59     ;NA0 EVENT
84,IOR,60,61,62,63,64,65,66,67,68,69     ;NC0 EVENT
85,IOR,70,71,72,73,74,75,76,77,78,79     ;NC1 EVENT
86,IOR,84,85                             ;NC0 + NC1
;
; SINGLE HITS ONLY
;
87,EOR,50,51,52,53,54,55,56,57,58,59     ;NA0 EVENT
88,EOR,60,61,62,63,64,65,66,67,68,69     ;NC0 EVENT
89,EOR,70,71,72,73,74,75,76,77,78,79     ;NC1 EVENT
90,IOR,88,89                             ;NC0 + NC1
;
; VALID SINGLE OR DOUBLE HITS (CSEP = 0,1)
;
91,GATE,509,0,11                         ;NA0 EVENT
92,GATE,510,0,11                         ;NC0 EVENT
93,GATE,511,0,11                         ;NC1 EVENT
94,IOR,92,93                             ;NC0 + NC1
;
; EVENTS INVOLVING VALID SINGLE OR DOUBLE HITS (CSEP = 0,1)
;
100,AND,91,94,-30,-31,12                 ;NN
101,AND,91,94,-30, 31,13                 ;NP
102,AND,91,94, 30, 31,14                 ;PP
103,IOR,100,101                          ;NN + NP
;
104,AND,91,-84,-85,16                    ;NA0 SINGLE
105,AND,92,-83,-85,16                    ;NC0 SINGLE
106,AND,93,-83,-84,16                    ;NC1 SINGLE
;
107,AND,91,-84,-85,-30,16                ;NA0 NEUTRAL SINGLE
108,AND,92,-83,-85,-31,16                ;NC0 NEUTRAL SINGLE
109,AND,93,-83,-84,-31,16                ;NC1 NEUTRAL SINGLE
;
; EVENTS INVOLVING VALID SINGLE HITS ONLY
;
110,AND,87,90,-30,-31,12                 ;NN
111,AND,87,90,-30, 31,13                 ;NP
112,AND,87,90, 30, 31,14                 ;PP
113,IOR,110,111                          ;NN + NP
;
114,AND,87,-84,-85,16                    ;NA0 SINGLE
115,AND,88,-83,-85,16                    ;NC0 SINGLE
116,AND,89,-83,-84,16                    ;NC1 SINGLE
;
117,AND,87,-84,-85,-30,16                ;NA0 NEUTRAL SINGLE
118,AND,88,-83,-85,-31,16                ;NC0 NEUTRAL SINGLE
119,AND,89,-83,-84,-31,16                ;NC1 NEUTRAL SINGLE
```

```
;
;*********************************************************************
;
120,GA,530,-550,550                    ;NAO TIME POSITION
121,GA,531,-550,550                    ;NC0 TIME POSITION
122,GA,532,-550,550                    ;NC1 TIME POSITION
123,IOR,121,122                        ;NC0 + NC1 TIME POSITION
;
124,GA,521,-500,500                    ;NAO POSITION DIFFERENCE
125,GA,522,-500,500                    ;NC0 POSITION DIFFERENCE
126,GA,523,-500,500                    ;NC1 POSITION DIFFERENCE
127,IOR,125,126                        ;NC0 + NC1 POSITION DIFFERENCE
;
128,GA,586,0,500                       ;NAO RADIUS FROM CENTER
129,AND,120,123,124,127,128            ;GOOD COINCIDENCE POSITIONS
;
130,GA,524,40,3000                     ;NAO PULSE HEIGHT
131,GA,525,40,3000                     ;NC0 PULSE HEIGHT
132,GA,526,40,3000                     ;NC1 PULSE HEIGHT
133,IOR,131,132                        ;NC0 + NC1 PULSE HEIGHT
134,AND,130,133                        ;GOOD COINCIDENCE PULSE HEIGHTS
;
140,IGATE,1                            ;VRATIO NN
141,IGATE,2                            ;VRATIO NP
142,IGATE,3                            ;VRATIO PP
;
143,IGATE,4                            ;VSCAT NN
144,IGATE,5                            ;VSCAT NP
145,IGATE,6                            ;VSCAT PP
;
150,AND,107,120,124,130                ;NAO NSING*XTIM*XDIF*PH
151,AND,108,121,125,131                ;NC0 NSING*XTIM*XDIF*PH
152,AND,109,122,126,132                ;NC1 NSING*XTIM*XDIF*PH
153,EOR,150,151,152                    ;NSING
154,AND,153,1                          ;NSING*NORMAL
155,AND,153,2                          ;NSING*REVERSE
;
160,AND,100,129,134,140,143            ;NN*POS*PH*VRAT*VSCAT
161,AND,101,129,134,141,144            ;NP*POS*PH*VRAT*VSCAT
162,IOR,160,161                        ;NN + NP
163,AND,162,1                          ;NN + NP * NORMAL
164,AND,162,2                          ;NN + NP * REVERSE
;
165,AND,102,142,145                    ;PP*VSCAT*VRAT
;
166,AND,103,134                        ;(NN + NP)*PH
```

APPENDIX D

SCALER TITLE FILE

```
; FILE = SLRTIT.TXT
;
; 19-NOV-87 (TAC)
;
; GATING OF SCALERS
;
; RUN  = Output of RUNGAT on LAMPF Gate Gen.
; BG   = Extended Beam Gate
; BEAM = BG * (N+R) * P
; BUSY = 12us BSY + OVFL + RQO + Out Reg. bit 12 + -RUNGAT
; P    = Polarized
; Q    = Quenched
; N    = Normal
; R    = Reverse
;
;Data format
;
;No., CAMAC ADDR, Function, Gating
;       where: CAMAC ADDR = CRATE-SLOT-SUBADDR.
;
;       NOTE: for the scalers currently in use,
;               front panel number = subaddr + 1
;
 1, 3-01-00, 2**18 (BROKEN) (RUN)
 2, 3-01-01, 2**18 (BROKEN) (RUN)
 3, 3-01-02, SUMKOS * -BUSY (RUN)
 4, 3-01-03, SUMMED KOSMICS (RUN)
 5, 3-01-04, KA0 KOSMICS    (RUN)
 6, 3-01-05, KC0 KOSMICS    (RUN)
 7, 3-01-06, KC1 KOSMICS    (RUN)
 8, 3-01-07, TAPED TRIGGER  (RUN)
 9, 3-01-08, NTER01         (RUN)
10, 3-01-09, EVENT   WI KOS (RUN)
11, 3-01-10, TRIGGER WI KOS (RUN)
12, 3-01-11, NA04+          (RUN)
;
13, 3-04-00, PRESC NSING    (RUN*BEAM)
14, 3-04-01, MONITOR        (RUN*BEAM)
15, 3-04-02, NN COIN        (RUN*BEAM)
16, 3-04-03, PRESC NPCOIN   (RUN*BEAM)
;
17, 3-05-00, PRESC PPCOIN   (RUN*BEAM)
18, 3-05-01, EVENT  W/O KOS (RUN*BEAM)
19, 3-05-02, TRIGGR W/O KOS (RUN*BEAM)
20, 3-05-03, CA01+          (RUN*BEAM)
;
21, 3-06-00, NA04+          (RUN*BEAM)
22, 3-06-01, NC04+          (RUN*BEAM)
23, 3-06-02, NC14+          (RUN*BEAM)
24, 3-06-03, CC01+          (RUN*BEAM)
;
25, 3-08-00, PRESC NSING    (RUN*BEAM*-BSY)
26, 3-08-01, MONITOR        (RUN*BEAM*-BSY)
27, 3-08-02, NN COIN        (RUN*BEAM*-BSY)
28, 3-08-03, PRESC NPCOIN   (RUN*BEAM*-BSY)
```

```
;
29, 3-09-00, PRESC PPCOIN   (RUN*BEAM*-BSY)
30, 3-09-01, EVENT          (RUN*BEAM*-BSY)
31, 3-09-02, TRIGGER        (RUN*BEAM*-BSY)
32, 3-09-03, SPARE          (RUN*BEAM*-BSY)
;
33, 3-10-00, SPARE          (RUN*BEAM*-BSY)
34, 3-10-01, SPARE          (RUN*BEAM*-BSY)
35, 3-10-02, SPARE          (RUN*BEAM*-BSY)
36, 3-10-03, SPARE          (RUN*BEAM*-BSY)
;
37, 3-12-00, BEAM GATES     (RUN*N*P)
38, 3-12-01, NTERO2         (RUN*N*P)
39, 3-12-02, FARADAY CUP    (RUN*N*P)
40, 3-12-03, NTERO1         (RUN*N*P)
;
41, 3-13-00, BEAM GATES     (RUN*R*P)
42, 3-13-01, NTERO2         (RUN*R*P)
43, 3-13-02, FARADAY CUP    (RUN*R*P)
44, 3-13-03, NTERO1         (RUN*R*P)
;
45, 3-14-00, BEAM GATES     (RUN*N*Q)
46, 3-14-01, NTERO2         (RUN*N*Q)
47, 3-14-02, FARADAY CUP    (RUN*N*Q)
48, 3-14-03, NTERO1         (RUN*N*Q)
;
49, 3-15-00, BEAM GATES     (RUN*R*Q)
50, 3-15-01, NTERO2         (RUN*R*Q)
51, 3-15-02, FARADAY CUP    (RUN*R*Q)
52, 3-15-03, NTERO1         (RUN*R*Q)
;
53, 3-16-00, NTPO LEFT      (RUN*N*P*BG)
54, 3-16-01, NTPO RIGHT     (RUN*N*P*BG)
55, 3-16-02, NTPO UP        (RUN*N*P*BG)
56, 3-16-03, NTPO DOWN      (RUN*N*P*BG)
;
57, 3-17-00, NTPO LEFT      (RUN*R*P*BG)
58, 3-17-01, NTPO RIGHT     (RUN*R*P*BG)
59, 3-17-02, NTPO UP        (RUN*R*P*BG)
60, 3-17-03, NTPO DOWN      (RUN*R*P*BG)
;
61, 3-18-00, CA01+          (RUN*N*P*BG)
62, 3-18-01, NA04+          (RUN*N*P*BG)
63, 3-18-02, CC01+          (RUN*N*P*BG)
64, 3-18-03, NC04+          (RUN*N*P*BG)
;
65, 3-19-00, CA01+          (RUN*R*P*BG)
66, 3-19-01, NA04+          (RUN*R*P*BG)
67, 3-19-02, CC01+          (RUN*R*P*BG)
68, 3-19-03, NC04+          (RUN*R*P*BG)
;
69, 3-20-00, EVENT          (RUN*N*P)
70, 3-20-01, TRIGGER        (RUN*N*P)
71, 3-20-02, TAPED TRIGGERS (RUN*N*P)
72, 3-20-03, SPARE          (RUN*N*P)
73, 3-20-04, SPARE          (RUN*N*P)
```

```
74, 3-20,05, SPARE              (RUN*N*P)
;
75, 3-21-00, EVENT              (RUN*R*P)
76, 3-21-01, TRIGGER            (RUN*R*P)
77, 3-21-02, TAPED TRIGGERS     (RUN*R*P)
78, 3-21-03, SPARE              (RUN*R*P)
79, 3-21-04, SPARE              (RUN*R*P)
80, 3-21-05, SPARE              (RUN*R*P)
;
81, 3-22-00, BEAM GATES         (RUN)
82, 3-22-01, NTERO2             (RUN)
83, 3-22-02, SPARE              (RUN)
84, 3-22-03, SPARE              (RUN)
;
257,LBUVAX (POL*N)   LBPO1 LEFT PROMPT
258,LBUVAX (POL*N)   LBPO1 RIGHT PROMPT
259,LBUVAX (POL*N)   LBPO1 DOWN PROMPT
260,LBUVAX (POL*N)   LBPO1 UP PROMPT
261,LBUVAX (POL*N)   LBPO1 LEFT DELAYED
262,LBUVAX (POL*N)   LBPO1 RIGHT DELAYED
263,LBUVAX (POL*N)   LBPO1 DOWN DELAYED
264,LBUVAX (POL*N)   LBPO1 UP DELAYED
265,LBUVAX (POL*N)   LBPO2 LEFT PROMPT
266,LBUVAX (POL*N)   LBPO2 RIGHT PROMPT
267,LBUVAX (POL*N)   LBPO2 DOWN PROMPT
268,LBUVAX (POL*N)   LBPO2 UP PROMPT
269,LBUVAX (POL*N)   LBPO2 LEFT DELAYED
270,LBUVAX (POL*N)   LBPO2 RIGHT DELAYED
271,LBUVAX (POL*N)   LBPO2 DOWN DELAYED
272,LBUVAX (POL*N)   LBPO2 UP DELAYED
273,LBUVAX (POL*N)   EPPO LEFT PROMPT
274,LBUVAX (POL*N)   EPPO RIGHT PROMPT
275,LBUVAX (POL*N)   EPPO DOWN PROMPT
276,LBUVAX (POL*N)   EPPO UP PROMPT
277,LBUVAX (POL*N)   EPPO LEFT DELAYED
278,LBUVAX (POL*N)   EPPO RIGHT DELAYED
279,LBUVAX (POL*N)   EPPO DOWN DELAYED
280,LBUVAX (POL*N)   EPPO UP DELAYED
281,LBUVAX (POL*N)   MSPO LEFT PROMPT
282,LBUVAX (POL*N)   MSPO RIGHT PROMPT
283,LBUVAX (POL*N)   MSPO DOWN PROMPT
284,LBUVAX (POL*N)   MSPO UP PROMPT
285,LBUVAX (POL*N)   MSPO LEFT DELAYED
286,LBUVAX (POL*N)   MSPO RIGHT DELAYED
287,LBUVAX (POL*N)   MSPO DOWN DELAYED
288,LBUVAX (POL*N)   MSPO UP DELAYED
289,LBUVAX (POL*N)   NTPO LEFT PROMPT
290,LBUVAX (POL*N)   NTPO RIGHT PROMPT
291,LBUVAX (POL*N)   NTPO DOWN PROMPT
292,LBUVAX (POL*N)   NTPO UP PROMPT
293,LBUVAX (POL*N)   NTPO LEFT DELAYED
294,LBUVAX (POL*N)   NTPO RIGHT DELAYED
295,LBUVAX (POL*N)   NTPO DOWN DELAYED
296,LBUVAX (POL*N)   NTPO UP DELAYED
297,LBUVAX (POL*N)   LCPO1 LEFT PROMPT
298,LBUVAX (POL*N)   LCPO1 RIGHT PROMPT
```

```
299,LBUVAX (POL*N)   LCPO1 DOWN PROMPT
300,LBUVAX (POL*N)   LCPO1 UP PROMPT
301,LBUVAX (POL*N)   LCPO1 LEFT DELAYED
302,LBUVAX (POL*N)   LCPO1 RIGHT DELAYED
303,LBUVAX (POL*N)   LCPO1 DOWN DELAYED
304,LBUVAX (POL*N)   LCPO1 UP DELAYED
305,LBUVAX (POL*N)   LCPO2 LEFT PROMPT
306,LBUVAX (POL*N)   LCPO2 RIGHT PROMPT
307,LBUVAX (POL*N)   LCPO2 DOWN PROMPT
308,LBUVAX (POL*N)   LCPO2 UP PROMPT
309,LBUVAX (POL*N)   LCPO2 LEFT DELAYED
310,LBUVAX (POL*N)   LCPO2 RIGHT DELAYED
311,LBUVAX (POL*N)   LCPO2 DOWN DELAYED
312,LBUVAX (POL*N)   LCPO2 UP DELAYED
313,LBUVAX (POL*N)   SPARE
314,LBUVAX (POL*N)   SPARE
315,LBUVAX (POL*N)   SPARE
316,LBUVAX (POL*N)   SPARE
317,LBUVAX (POL*N)   SPARE
318,LBUVAX (POL*N)   SPARE
319,LBUVAX (POL*N)   SPARE
320,LBUVAX (POL*N)   SPARE
321,LBUVAX (POL*R)   LBPO1 LEFT PROMPT
322,LBUVAX (POL*R)   LBPO1 RIGHT PROMPT
323,LBUVAX (POL*R)   LBPO1 DOWN PROMPT
324,LBUVAX (POL*R)   LBPO1 UP PROMPT
325,LBUVAX (POL*R)   LBPO1 LEFT DELAYED
326,LBUVAX (POL*R)   LBPO1 RIGHT DELAYED
327,LBUVAX (POL*R)   LBPO1 DOWN DELAYED
328,LBUVAX (POL*R)   LBPO1 UP DELAYED
329,LBUVAX (POL*R)   LBPO2 LEFT PROMPT
330,LBUVAX (POL*R)   LBPO2 RIGHT PROMPT
331,LBUVAX (POL*R)   LBPO2 DOWN PROMPT
332,LBUVAX (POL*R)   LBPO2 UP PROMPT
333,LBUVAX (POL*R)   LBPO2 LEFT DELAYED
334,LBUVAX (POL*R)   LBPO2 RIGHT DELAYED
335,LBUVAX (POL*R)   LBPO2 DOWN DELAYED
336,LBUVAX (POL*R)   LBPO2 UP DELAYED
337,LBUVAX (POL*R)   EPPO LEFT PROMPT
338,LBUVAX (POL*R)   EPPO RIGHT PROMPT
339,LBUVAX (POL*R)   EPPO DOWN PROMPT
340,LBUVAX (POL*R)   EPPO UP PROMPT
341,LBUVAX (POL*R)   EPPO LEFT DELAYED
342,LBUVAX (POL*R)   EPPO RIGHT DELAYED
343,LBUVAX (POL*R)   EPPO DOWN DELAYED
344,LBUVAX (POL*R)   EPPO UP DELAYED
345,LBUVAX (POL*R)   MSPO LEFT PROMPT
346,LBUVAX (POL*R)   MSPO RIGHT PROMPT
347,LBUVAX (POL*R)   MSPO DOWN PROMPT
348,LBUVAX (POL*R)   MSPO UP PROMPT
349,LBUVAX (POL*R)   MSPO LEFT DELAYED
350,LBUVAX (POL*R)   MSPO RIGHT DELAYED
351,LBUVAX (POL*R)   MSPO DOWN DELAYED
352,LBUVAX (POL*R)   MSPO UP DELAYED
353,LBUVAX (POL*R)   NTPO LEFT PROMPT
354,LBUVAX (POL*R)   NTPO RIGHT PROMPT
```

```
355,LBUVAX (POL*R)   NTPO DOWN PROMPT
356,LBUVAX (POL*R)   NTPO UP PROMPT
357,LBUVAX (POL*R)   NTPO LEFT DELAYED
358,LBUVAX (POL*R)   NTPO RIGHT DELAYED
359,LBUVAX (POL*R)   NTPO DOWN DELAYED
360,LBUVAX (POL*R)   NTPO UP DELAYED
361,LBUVAX (POL*R)   LCPO1 LEFT PROMPT
362,LBUVAX (POL*R)   LCPO1 RIGHT PROMPT
363,LBUVAX (POL*R)   LCPO1 DOWN PROMPT
364,LBUVAX (POL*R)   LCPO1 UP PROMPT
365,LBUVAX (POL*R)   LCPO1 LEFT DELAYED
366,LBUVAX (POL*R)   LCPO1 RIGHT DELAYED
367,LBUVAX (POL*R)   LCPO1 DOWN DELAYED
368,LBUVAX (POL*R)   LCPO1 UP DELAYED
369,LBUVAX (POL*R)   LCPO2 LEFT PROMPT
370,LBUVAX (POL*R)   LCPO2 RIGHT PROMPT
371,LBUVAX (POL*R)   LCPO2 DOWN PROMPT
372,LBUVAX (POL*R)   LCPO2 UP PROMPT
373,LBUVAX (POL*R)   LCPO2 LEFT DELAYED
374,LBUVAX (POL*R)   LCPO2 RIGHT DELAYED
375,LBUVAX (POL*R)   LCPO2 DOWN DELAYED
376,LBUVAX (POL*R)   LCPO2 UP DELAYED
377,LBUVAX (POL*R)   SPARE
378,LBUVAX (POL*R)   SPARE
379,LBUVAX (POL*R)   SPARE
380,LBUVAX (POL*R)   SPARE
381,LBUVAX (POL*R)   SPARE
382,LBUVAX (POL*R)   SPARE
383,LBUVAX (POL*R)   SPARE
384,LBUVAX (POL*R)   SPARE
385,LBUVAX (QEN*N)   LBPO1 LEFT PROMPT
386,LBUVAX (QEN*N)   LBPO1 RIGHT PROMPT
387,LBUVAX (QEN*N)   LBPO1 DOWN PROMPT
388,LBUVAX (QEN*N)   LBPO1 UP PROMPT
389,LBUVAX (QEN*N)   LBPO1 LEFT DELAYED
390,LBUVAX (QEN*N)   LBPO1 RIGHT DELAYED
391,LBUVAX (QEN*N)   LBPO1 DOWN DELAYED
392,LBUVAX (QEN*N)   LBPO1 UP DELAYED
393,LBUVAX (QEN*N)   LBPO2 LEFT PROMPT
394,LBUVAX (QEN*N)   LBPO2 RIGHT PROMPT
395,LBUVAX (QEN*N)   LBPO2 DOWN PROMPT
396,LBUVAX (QEN*N)   LBPO2 UP PROMPT
397,LBUVAX (QEN*N)   LBPO2 LEFT DELAYED
398,LBUVAX (QEN*N)   LBPO2 RIGHT DELAYED
399,LBUVAX (QEN*N)   LBPO2 DOWN DELAYED
400,LBUVAX (QEN*N)   LBPO2 UP DELAYED
401,LBUVAX (QEN*N)   EPPO LEFT PROMPT
402,LBUVAX (QEN*N)   EPPO RIGHT PROMPT
403,LBUVAX (QEN*N)   EPPO DOWN PROMPT
404,LBUVAX (QEN*N)   EPPO UP PROMPT
405,LBUVAX (QEN*N)   EPPO LEFT DELAYED
406,LBUVAX (QEN*N)   EPPO RIGHT DELAYED
407,LBUVAX (QEN*N)   EPPO DOWN DELAYED
408,LBUVAX (QEN*N)   EPPO UP DELAYED
409,LBUVAX (QEN*N)   MSPO LEFT PROMPT
410,LBUVAX (QEN*N)   MSPO RIGHT PROMPT
```

```
411,LBUVAX (QEN*N)   MSPO DOWN PROMPT
412,LBUVAX (QEN*N)   MSPO UP PROMPT
413,LBUVAX (QEN*N)   MSPO LEFT DELAYED
414,LBUVAX (QEN*N)   MSPO RIGHT DELAYED
415,LBUVAX (QEN*N)   MSPO DOWN DELAYED
416,LBUVAX (QEN*N)   MSPO UP DELAYED
417,LBUVAX (QEN*N)   NTPO LEFT PROMPT
418,LBUVAX (QEN*N)   NTPO RIGHT PROMPT
419,LBUVAX (QEN*N)   NTPO DOWN PROMPT
420,LBUVAX (QEN*N)   NTPO UP PROMPT
421,LBUVAX (QEN*N)   NTPO LEFT DELAYED
422,LBUVAX (QEN*N)   NTPO RIGHT DELAYED
423,LBUVAX (QEN*N)   NTPO DOWN DELAYED
424,LBUVAX (QEN*N)   NTPO UP DELAYED
425,LBUVAX (QEN*N)   LCPO1 LEFT PROMPT
426,LBUVAX (QEN*N)   LCPO1 RIGHT PROMPT
427,LBUVAX (QEN*N)   LCPO1 DOWN PROMPT
428,LBUVAX (QEN*N)   LCPO1 UP PROMPT
429,LBUVAX (QEN*N)   LCPO1 LEFT DELAYED
430,LBUVAX (QEN*N)   LCPO1 RIGHT DELAYED
431,LBUVAX (QEN*N)   LCPO1 DOWN DELAYED
432,LBUVAX (QEN*N)   LCPO1 UP DELAYED
433,LBUVAX (QEN*N)   LCPO2 LEFT PROMPT
434,LBUVAX (QEN*N)   LCPO2 RIGHT PROMPT
435,LBUVAX (QEN*N)   LCPO2 DOWN PROMPT
436,LBUVAX (QEN*N)   LCPO2 UP PROMPT
437,LBUVAX (QEN*N)   LCPO2 LEFT DELAYED
438,LBUVAX (QEN*N)   LCPO2 RIGHT DELAYED
439,LBUVAX (QEN*N)   LCPO2 DOWN DELAYED
440,LBUVAX (QEN*N)   LCPO2 UP DELAYED
441,LBUVAX (QEN*N)   SPARE
442,LBUVAX (QEN*N)   SPARE
443,LBUVAX (QEN*N)   SPARE
444,LBUVAX (QEN*N)   SPARE
445,LBUVAX (QEN*N)   SPARE
446,LBUVAX (QEN*N)   SPARE
447,LBUVAX (QEN*N)   SPARE
448,LBUVAX (QEN*N)   SPARE
449,LBUVAX (QEN*R)   LBPO1 LEFT PROMPT
450,LBUVAX (QEN*R)   LBPO1 RIGHT PROMPT
451,LBUVAX (QEN*R)   LBPO1 DOWN PROMPT
452,LBUVAX (QEN*R)   LBPO1 UP PROMPT
453,LBUVAX (QEN*R)   LBPO1 LEFT DELAYED
454,LBUVAX (QEN*R)   LBPO1 RIGHT DELAYED
455,LBUVAX (QEN*R)   LBPO1 DOWN DELAYED
456,LBUVAX (QEN*R)   LBPO1 UP DELAYED
457,LBUVAX (QEN*R)   LBPO2 LEFT PROMPT
458,LBUVAX (QEN*R)   LBPO2 RIGHT PROMPT
459,LBUVAX (QEN*R)   LBPO2 DOWN PROMPT
460,LBUVAX (QEN*R)   LBPO2 UP PROMPT
461,LBUVAX (QEN*R)   LBPO2 LEFT DELAYED
462,LBUVAX (QEN*R)   LBPO2 RIGHT DELAYED
463,LBUVAX (QEN*R)   LBPO2 DOWN DELAYED
464,LBUVAX (QEN*R)   LBPO2 UP DELAYED
465,LBUVAX (QEN*R)   EPPO LEFT PROMPT
466,LBUVAX (QEN*R)   EPPO RIGHT PROMPT
```

```
467,LBUVAX (QEN*R)   EPPO DOWN PROMPT
468,LBUVAX (QEN*R)   EPPO UP PROMPT
469,LBUVAX (QEN*R)   EPPO LEFT DELAYED
470,LBUVAX (QEN*R)   EPPO RIGHT DELAYED
471,LBUVAX (QEN*R)   EPPO DOWN DELAYED
472,LBUVAX (QEN*R)   EPPO UP DELAYED
473,LBUVAX (QEN*R)   MSPO LEFT PROMPT
474,LBUVAX (QEN*R)   MSPO RIGHT PROMPT
475,LBUVAX (QEN*R)   MSPO DOWN PROMPT
476,LBUVAX (QEN*R)   MSPO UP PROMPT
477,LBUVAX (QEN*R)   MSPO LEFT DELAYED
478,LBUVAX (QEN*R)   MSPO RIGHT DELAYED
479,LBUVAX (QEN*R)   MSPO DOWN DELAYED
480,LBUVAX (QEN*R)   MSPO UP DELAYED
481,LBUVAX (QEN*R)   NTPO LEFT PROMPT
482,LBUVAX (QEN*R)   NTPO RIGHT PROMPT
483,LBUVAX (QEN*R)   NTPO DOWN PROMPT
484,LBUVAX (QEN*R)   NTPO UP PROMPT
485,LBUVAX (QEN*R)   NTPO LEFT DELAYED
486,LBUVAX (QEN*R)   NTPO RIGHT DELAYED
487,LBUVAX (QEN*R)   NTPO DOWN DELAYED
488,LBUVAX (QEN*R)   NTPO UP DELAYED
489,LBUVAX (QEN*R)   LCPO1 LEFT PROMPT
490,LBUVAX (QEN*R)   LCPO1 RIGHT PROMPT
491,LBUVAX (QEN*R)   LCPO1 DOWN PROMPT
492,LBUVAX (QEN*R)   LCPO1 UP PROMPT
493,LBUVAX (QEN*R)   LCPO1 LEFT DELAYED
494,LBUVAX (QEN*R)   LCPO1 RIGHT DELAYED
495,LBUVAX (QEN*R)   LCPO1 DOWN DELAYED
496,LBUVAX (QEN*R)   LCPO1 UP DELAYED
497,LBUVAX (QEN*R)   LCPO2 LEFT PROMPT
498,LBUVAX (QEN*R)   LCPO2 RIGHT PROMPT
499,LBUVAX (QEN*R)   LCPO2 DOWN PROMPT
500,LBUVAX (QEN*R)   LCPO2 UP PROMPT
501,LBUVAX (QEN*R)   LCPO2 LEFT DELAYED
502,LBUVAX (QEN*R)   LCPO2 RIGHT DELAYED
503,LBUVAX (QEN*R)   LCPO2 DOWN DELAYED
504,LBUVAX (QEN*R)   LCPO2 UP DELAYED
505,LBUVAX (QEN*R)   SPARE
506,LBUVAX (QEN*R)   SPARE
507,LBUVAX (QEN*R)   SPARE
508,LBUVAX (QEN*R)   SPARE
509,LBUVAX (QEN*R)   SPARE
510,LBUVAX (QEN*R)   SPARE
511,LBUVAX (QEN*R)   SPARE
512,LBUVAX (QEN*R)   SPARE
```

APPENDIX E

DATA WORD TITLE FILE

```
; BLK001.TXT
;
; * Titles for data variables for NTOF event7
; *
; * last updated 15-NOV-1987
;
;******** raw data words (1-200) ********
;
;
001, ITRFO
002, ITEPMON * EPPO BEAM MONITOR "BIT"
003, ITNTMON * NTPO BEAM MONITOR "BIT"
004, NN,NP,PP TIME (XOR)
005, COSMIC TRIGGER TIME
006, SINGLE TRIGGER TIME
007, MTCA0 * CHARGED PARTICLE CA0 MEANTIME
008, MTCA1 * CHARGED PARTICLE CA1 MEANTIME
009, MTCA2 * CHARGED PARTICLE CA2 MEANTIME
010, MTCA3 * CHARGED PARTICLE CA3 MEANTIME
011, MTCA4 * CHARGED PARTICLE CA4 MEANTIME
012, MTCC0 * CHARGED PARTICLE CC0 MEANTIME
013, MTCC1 * CHARGED PARTICLE CC1 MEANTIME
014, MTCC2 * CHARGED PARTICLE CC2 MEANTIME
015, MTCC3 * CHARGED PARTICLE CC3 MEANTIME
016, MTCC4 * CHARGED PARTICLE CC4 MEANTIME
;
017, ITIM(1,0,1) * TIME "+" CELL 0 PLANE 1
018, ITIM(2,0,1) * TIME "-" CELL 0 PLANE 1
019, ITIM(1,1,1) * TIME "+" CELL 1 PLANE 1
020, ITIM(2,1,1) * TIME "-" CELL 1 PLANE 1
021, ITIM(1,2,1) * TIME "+" CELL 2 PLANE 1
022, ITIM(2,2,1) * TIME "-" CELL 2 PLANE 1
023, ITIM(1,3,1) * TIME "+" CELL 3 PLANE 1
024, ITIM(2,3,1) * TIME "-" CELL 3 PLANE 1
025, ITIM(1,4,1) * TIME "+" CELL 4 PLANE 1
026, ITIM(2,4,1) * TIME "-" CELL 4 PLANE 1
027, ITIM(1,5,1) * TIME "+" CELL 5 PLANE 1
028, ITIM(2,5,1) * TIME "-" CELL 5 PLANE 1
029, ITIM(1,6,1) * TIME "+" CELL 6 PLANE 1
030, ITIM(2,6,1) * TIME "-" CELL 6 PLANE 1
031, ITIM(1,7,1) * TIME "+" CELL 7 PLANE 1
032, ITIM(2,7,1) * TIME "-" CELL 7 PLANE 1
033, ITIM(1,8,1) * TIME "+" CELL 8 PLANE 1
034, ITIM(2,8,1) * TIME "-" CELL 8 PLANE 1
035, ITIM(1,9,1) * TIME "+" CELL 9 PLANE 1
036, ITIM(2,9,1) * TIME "-" CELL 9 PLANE 1
;
037, ITIM(1,0,2) * TIME "+" CELL 0 PLANE 2
038, ITIM(2,0,2) * TIME "-" CELL 0 PLANE 2
039, ITIM(1,1,2) * TIME "+" CELL 1 PLANE 2
040, ITIM(2,1,2) * TIME "-" CELL 1 PLANE 2
041, ITIM(1,2,2) * TIME "+" CELL 2 PLANE 2
042, ITIM(2,2,2) * TIME "-" CELL 2 PLANE 2
043, ITIM(1,3,2) * TIME "+" CELL 3 PLANE 2
044, ITIM(2,3,2) * TIME "-" CELL 3 PLANE 2
```

```
151, NORMAL  SPIN LEVEL
152, REVERSE SPIN LEVEL
153, ANALOG MULTIPLICITY PLANE 1
154, ANALOG MULTIPLICITY PLANE 2
155, ANALOG MULTIPLICITY PLANE 3
156, SPARE P.H.
157, SPARE P.H.
158, SPARE P.H.
159, SPARE P.H.
160, SPARE P.H.
;
;****** basic calculated data words ****************
;
201, XDF(0,1)* POSITION DIFFERENCE CELL 0 PLANE 1
202, XDF(1,1)* POSITION DIFFERENCE CELL 1 PLANE 1
203, XDF(2,1)* POSITION DIFFERENCE CELL 2 PLANE 1
204, XDF(3,1)* POSITION DIFFERENCE CELL 3 PLANE 1
205, XDF(4,1)* POSITION DIFFERENCE CELL 4 PLANE 1
206, XDF(5,1)* POSITION DIFFERENCE CELL 5 PLANE 1
207, XDF(6,1)* POSITION DIFFERENCE CELL 6 PLANE 1
208, XDF(7,1)* POSITION DIFFERENCE CELL 7 PLANE 1
209, XDF(8,1)* POSITION DIFFERENCE CELL 8 PLANE 1
210, XDF(9,1)* POSITION DIFFERENCE CELL 9 PLANE 1
;
211, XDF(0,2)* POSITION DIFFERENCE CELL 0 PLANE 2
212, XDF(1,1)* POSITION DIFFERENCE CELL 1 PLANE 2
213, XDF(2,2)* POSITION DIFFERENCE CELL 2 PLANE 2
214, XDF(3,2)* POSITION DIFFERENCE CELL 3 PLANE 2
215, XDF(4,2)* POSITION DIFFERENCE CELL 4 PLANE 2
216, XDF(5,2)* POSITION DIFFERENCE CELL 5 PLANE 2
217, XDF(6,2)* POSITION DIFFERENCE CELL 6 PLANE 2
218, XDF(7,2)* POSITION DIFFERENCE CELL 7 PLANE 2
219, XDF(8,2)* POSITION DIFFERENCE CELL 8 PLANE 2
220, XDF(9,2)* POSITION DIFFERENCE CELL 9 PLANE 2
;
221, XDF(0,3)* POSITION DIFFERENCE CELL 0 PLANE 3
222, XDF(1,3)* POSITION DIFFERENCE CELL 1 PLANE 3
223, XDF(2,3)* POSITION DIFFERENCE CELL 2 PLANE 3
224, XDF(3,3)* POSITION DIFFERENCE CELL 3 PLANE 3
225, XDF(4,3)* POSITION DIFFERENCE CELL 4 PLANE 3
226, XDF(5,3)* POSITION DIFFERENCE CELL 5 PLANE 3
227, XDF(6,3)* POSITION DIFFERENCE CELL 6 PLANE 3
228, XDF(7,3)* POSITION DIFFERENCE CELL 7 PLANE 3
229, XDF(8,3)* POSITION DIFFERENCE CELL 8 PLANE 3
230, XDF(9,3)* POSITION DIFFERENCE CELL 9 PLANE 3
;
231, PHG(0,1) * GEO MN PH CELL 0 PLANE 1
232, PHG(1,1) * GEO MN PH CELL 1 PLANE 1
233, PHG(2,1) * GEO MN PH CELL 2 PLANE 1
234, PHG(3,1) * GEO MN PH CELL 3 PLANE 1
235, PHG(4,1) * GEO MN PH CELL 4 PLANE 1
236, PHG(5,1) * GEO MN PH CELL 5 PLANE 1
237, PHG(6,1) * GEO MN PH CELL 6 PLANE 1
238, PHG(7,1) * GEO MN PH CELL 7 PLANE 1
239, PHG(8,1) * GEO MN PH CELL 8 PLANE 1
240, PHG(9,1) * GEO MN PH CELL 9 PLANE 1
```

```
099, IPH(1,9,1) * PH "+"  CELL 9 PLANE 1
100, IPH(2,9,1) * PH "-"  CELL 9 PLANE 1
;
101, IPH(1,0,2) * PH "+"  CELL 0 PLANE 2
102, IPH(2,0,2) * PH "-"  CELL 0 PLANE 2
103, IPH(1,1,2) * PH "+"  CELL 1 PLANE 2
104, IPH(2,1,2) * PH "-"  CELL 1 PLANE 2
105, IPH(1,2,2) * PH "+"  CELL 2 PLANE 2
106, IPH(2,2,2) * PH "-"  CELL 2 PLANE 2
107, IPH(1,3,2) * PH "+"  CELL 3 PLANE 2
108, IPH(2,3,2) * PH "-"  CELL 3 PLANE 2
109, IPH(1,4,2) * PH "+"  CELL 4 PLANE 2
110, IPH(2,4,2) * PH "-"  CELL 4 PLANE 2
111, IPH(1,5,2) * PH "+"  CELL 5 PLANE 2
112, IPH(2,5,2) * PH "-"  CELL 5 PLANE 2
113, IPH(1,6,2) * PH "+"  CELL 6 PLANE 2
114, IPH(2,6,2) * PH "-"  CELL 6 PLANE 2
115, IPH(1,7,2) * PH "+"  CELL 7 PLANE 2
116, IPH(2,7,2) * PH "-"  CELL 7 PLANE 2
117, IPH(1,8,2) * PH "+"  CELL 8 PLANE 2
118, IPH(2,8,2) * PH "-"  CELL 8 PLANE 2
119, IPH(1,9,2) * PH "+"  CELL 9 PLANE 2
120, IPH(2,9,2) * PH "-"  CELL 9 PLANE 2
;
121, IPH(1,0,3) * PH "+"  CELL 0 PLANE 3
122, IPH(2,0,3) * PH "-"  CELL 0 PLANE 3
123, IPH(1,1,3) * PH "+"  CELL 1 PLANE 3
124, IPH(2,1,3) * PH "-"  CELL 1 PLANE 3
125, IPH(1,2,3) * PH "+"  CELL 2 PLANE 3
126, IPH(2,2,3) * PH "-"  CELL 2 PLANE 3
127, IPH(1,3,3) * PH "+"  CELL 3 PLANE 3
128, IPH(2,3,3) * PH "-"  CELL 3 PLANE 3
129, IPH(1,4,3) * PH "+"  CELL 4 PLANE 3
130, IPH(2,4,3) * PH "-"  CELL 4 PLANE 3
131, IPH(1,5,3) * PH "+"  CELL 5 PLANE 3
132, IPH(2,5,3) * PH "-"  CELL 5 PLANE 3
133, IPH(1,6,3) * PH "+"  CELL 6 PLANE 3
134, IPH(2,6,3) * PH "-"  CELL 6 PLANE 3
135, IPH(1,7,3) * PH "+"  CELL 7 PLANE 3
136, IPH(2,7,3) * PH "-"  CELL 7 PLANE 3
137, IPH(1,8,3) * PH "+"  CELL 8 PLANE 3
138, IPH(2,8,3) * PH "-"  CELL 8 PLANE 3
139, IPH(1,9,3) * PH "+"  CELL 9 PLANE 3
140, IPH(2,9,3) * PH "-"  CELL 9 PLANE 3
;
141, PHCA0 * SUMMED P.H. CHARGE PARTICLE CA0
142, PHCA1 * SUMMED P.H. CHARGE PARTICLE CA1
143, PHCA2 * SUMMED P.H. CHARGE PARTICLE CA2
144, PHCA3 * SUMMED P.H. CHARGE PARTICLE CA3
145, PHCA4 * SUMMED P.H. CHARGE PARTICLE CA4
146, PHCC0 * SUMMED P.H. CHARGE PARTICLE CC0
147, PHCC1 * SUMMED P.H. CHARGE PARTICLE CC1
148, PHCC2 * SUMMED P.H. CHARGE PARTICLE CC2
149, PHCC3 * SUMMED P.H. CHARGE PARTICLE CC3
150, PHCC4 * SUMMED P.H. CHARGE PARTICLE CC4
;
```

```
045, ITIM(1,4,2) * TIME "+" CELL 4 PLANE 2
046, ITIM(2,4,2) * TIME "-" CELL 4 PLANE 2
047, ITIM(1,5,2) * TIME "+" CELL 5 PLANE 2
048, ITIM(2,5,2) * TIME "-" CELL 5 PLANE 2
049, ITIM(1,6,2) * TIME "+" CELL 6 PLANE 2
050, ITIM(2,6,2) * TIME "-" CELL 6 PLANE 2
051, ITIM(1,7,2) * TIME "+" CELL 7 PLANE 2
052, ITIM(2,7,2) * TIME "-" CELL 7 PLANE 2
053, ITIM(1,8,2) * TIME "+" CELL 8 PLANE 2
054, ITIM(2,8,2) * TIME "-" CELL 8 PLANE 2
055, ITIM(1,9,2) * TIME "+" CELL 9 PLANE 2
056, ITIM(2,9,2) * TIME "-" CELL 9 PLANE 2
;
057, ITIM(1,0,3) * TIME "+" CELL 0 PLANE 3
058, ITIM(2,0,3) * TIME "-" CELL 0 PLANE 3
059, ITIM(1,1,3) * TIME "+" CELL 1 PLANE 3
060, ITIM(2,1,3) * TIME "-" CELL 1 PLANE 3
061, ITIM(1,2,3) * TIME "+" CELL 2 PLANE 3
062, ITIM(2,2,3) * TIME "-" CELL 2 PLANE 3
063, ITIM(1,3,3) * TIME "+" CELL 3 PLANE 3
064, ITIM(2,3,3) * TIME "-" CELL 3 PLANE 3
065, ITIM(1,4,3) * TIME "+" CELL 4 PLANE 3
066, ITIM(2,4,3) * TIME "-" CELL 4 PLANE 3
067, ITIM(1,5,3) * TIME "+" CELL 5 PLANE 3
068, ITIM(2,5,3) * TIME "-" CELL 5 PLANE 3
069, ITIM(1,6,3) * TIME "+" CELL 6 PLANE 3
070, ITIM(2,6,3) * TIME "-" CELL 6 PLANE 3
071, ITIM(1,7,3) * TIME "+" CELL 7 PLANE 3
072, ITIM(2,7,3) * TIME "-" CELL 7 PLANE 3
073, ITIM(1,8,3) * TIME "+" CELL 8 PLANE 3
074, ITIM(2,8,3) * TIME "-" CELL 8 PLANE 3
075, ITIM(1,9,3) * TIME "+" CELL 9 PLANE 3
076, ITIM(2,9,3) * TIME "-" CELL 9 PLANE 3
077, SPARE TIME
078, SPARE TIME
079, SPARE TIME
080, SPARE TIME
;
081, IPH(1,0,1) * PH "+"  CELL 0 PLANE 1
082, IPH(2,0,1) * PH "-"  CELL 0 PLANE 1
083, IPH(1,1,1) * PH "+"  CELL 1 PLANE 1
084, IPH(2,1,1) * PH "-"  CELL 1 PLANE 1
085, IPH(1,2,1) * PH "+"  CELL 2 PLANE 1
086, IPH(2,2,1) * PH "-"  CELL 2 PLANE 1
087, IPH(1,3,1) * PH "+"  CELL 3 PLANE 1
088, IPH(2,3,1) * PH "-"  CELL 3 PLANE 1
089, IPH(1,4,1) * PH "+"  CELL 4 PLANE 1
090, IPH(2,4,1) * PH "-"  CELL 4 PLANE 1
091, IPH(1,5,1) * PH "+"  CELL 5 PLANE 1
092, IPH(2,5,1) * PH "-"  CELL 5 PLANE 1
093, IPH(1,6,1) * PH "+"  CELL 6 PLANE 1
094, IPH(2,6,1) * PH "-"  CELL 6 PLANE 1
095, IPH(1,7,1) * PH "+"  CELL 7 PLANE 1
096, IPH(2,7,1) * PH "-"  CELL 7 PLANE 1
097, IPH(1,8,1) * PH "+"  CELL 8 PLANE 1
098, IPH(2,8,1) * PH "-"  CELL 8 PLANE 1
```

```
;
241, PHG(0,2) * GEO MN PH CELL 0 PLANE 2
242, PHG(1,2) * GEO MN PH CELL 1 PLANE 2
243, PHG(2,2) * GEO MN PH CELL 2 PLANE 2
244, PHG(3,2) * GEO MN PH CELL 3 PLANE 2
245, PHG(4,2) * GEO MN PH CELL 4 PLANE 2
246, PHG(5,2) * GEO MN PH CELL 5 PLANE 2
247, PHG(6,2) * GEO MN PH CELL 6 PLANE 2
248, PHG(7,2) * GEO MN PH CELL 7 PLANE 2
249, PHG(8,2) * GEO MN PH CELL 8 PLANE 2
250, PHG(9,2) * GEO MN PH CELL 9 PLANE 2
;
251, PHG(0,3) * GEO MN PH CELL 0 PLANE 3
252, PHG(1,3) * GEO MN PH CELL 1 PLANE 3
253, PHG(2,3) * GEO MN PH CELL 2 PLANE 3
254, PHG(3,3) * GEO MN PH CELL 3 PLANE 3
255, PHG(',3) * GEO MN PH CELL 4 PLANE 3
256, PHG(5,3) * GEO MN PH CELL 5 PLANE 3
257, PHG(6,3) * GEO MN PH CELL 6 PLANE 3
258, PHG(7,3) * GEO MN PH CELL 7 PLANE 3
259, PHG(8,3) * GEO MN PH CELL 8 PLANE 3
260, PHG(9,3) * GEO MN PH CELL 9 PLANE 3
;
261, XTM(0,1) * X TIME POS IN CELL 0 PLANE 1
262, XTM(1,1) * X TIME POS IN CELL 1 PLANE 1
263, XTM(2,1) * X TIME POS IN CELL 2 PLANE 1
264, XTM(3,1) * X TIME POS IN CELL 3 PLANE 1
265, XTM(4,1) * X TIME POS IN CELL 4 PLANE 1
266, XTM(5,1) * X TIME POS IN CELL 5 PLANE 1
267, XTM(6,1) * X TIME POS IN CELL 6 PLANE 1
268, XTM(7,1) * X TIME POS IN CELL 7 PLANE 1
269, XTM(8,1) * X TIME POS IN CELL 8 PLANE 1
270, XTM(9,1) * X TIME POS IN CELL 9 PLANE 1
;
271, XTM(0,2) * X TIME POS IN CELL 0 PLANE 2
272, XTM(1,2) * X TIME POS IN CELL 1 PLANE 2
273, XTM(2,2) * X TIME POS IN CELL 2 PLANE 2
274, XTM(3,2) * X TIME POS IN CELL 3 PLANE 2
275, XTM(4,2) * X TIME POS IN CELL 4 PLANE 2
276, XTM(5,2) * X TIME POS IN CELL 5 PLANE 2
277, XTM(6,2) * X TIME POS IN CELL 6 PLANE 2
278, XTM(7,2) * X TIME POS IN CELL 7 PLANE 2
279, XTM(8,2) * X TIME POS IN CELL 8 PLANE 2
280, XTM(9,2) * X TIME POS IN CELL 9 PLANE 2
;
281, XTM(0,3) * X TIME POS IN CELL 0 PLANE 3
282, XTM(1,3) * X TIME POS IN CELL 1 PLANE 3
283, XTM(2,3) * X TIME POS IN CELL 2 PLANE 3
284, XTM(3,3) * X TIME POS IN CELL 3 PLANE 3
285, XTM(4,3) * X TIME POS IN CELL 4 PLANE 3
286, XTM(5,3) * X TIME POS IN CELL 5 PLANE 3
287, XTM(6,3) * X TIME POS IN CELL 6 PLANE 3
288, XTM(7,3) * X TIME POS IN CELL 7 PLANE 3
289, XTM(8,3) * X TIME POS IN CELL 8 PLANE 3
290, XTM(9,3) * X TIME POS IN CELL 9 PLANE 3
;
```

```
291, TOF(0,1) * TOF WRT.RF CELL 0 PLANE 1
292, TOF(1,1) * TOF WRT.RF CELL 1 PLANE 1
293, TOF(2,1) * TOF WRT.RF CELL 2 PLANE 1
294, TOF(3,1) * TOF WRT RF CELL 3 PLANE 1
295, TOF(4,1) * TOF WRT.RF CELL 4 PLANE 1
296, TOF(5,1) * TOF WRT.RF CELL 5 PLANE 1
297, TOF(6,1) * TOF WRT RF CELL 6 PLANE 1
298, TOF(7,1) * TOF WRT.RF CELL 7 PLANE 1
299, TOF(8,1) * TOF WRT.RF CELL 8 PLANE 1
300, TOF(9,1) * TOF WRT.RF CELL 9 PLANE 1
;
301, TOF(0,2) * TOF WRT RF CELL 0 PLANE 2
302, TOF(1,2) * TOF WRT.RF CELL 1 PLANE 2
303, TOF(2,2) * TOF WRT.RF CELL 2 PLANE 2
304, TOF(3,2) * TOF WRT RF CELL 3 PLANE 2
305, TOF(4,2) * TOF WRT.RF CELL 4 PLANE 2
306, TOF(5,2) * TOF WRT.RF CELL 5 PLANE 2
307, TOF(6,2) * TOF WRT RF CELL 6 PLANE 2
308, TOF(7,2) * TOF WRT.RF CELL 7 PLANE 2
309, TOF(8,2) * TOF WRT.RF CELL 8 PLANE 2
310, TOF(9,2) * TOF WRT.RF CELL 9 PLANE 2
;
311, TOF(0,3) * TOF WRT RF CELL 0 PLANE 3
312, TOF(1,3) * TOF WRT.RF CELL 1 PLANE 3
313, TOF(2,3) * TOF WRT.RF CELL 2 PLANE 3
314, TOF(3,3) * TOF WRT RF CELL 3 PLANE 3
315, TOF(4,3) * TOF WRT.RF CELL 4 PLANE 3
316, TOF(5,3) * TOF WRT.RF CELL 5 PLANE 3
317, TOF(6,3) * TOF WRT RF CELL 6 PLANE 3
318, TOF(7,3) * TOF WRT.RF CELL 7 PLANE 3
319, TOF(8,3) * TOF WRT.RF CELL 8 PLANE 3
320, TOF(9,3) * TOF WRT.RF CELL 9 PLANE 3
;
321, MTM(0,1) * MEAN TIME CELL 0 PLANE 1
322, MTM(1,1) * MEAN TIME CELL 1 PLANE 1
323, MTM(2,1) * MEAN TIME CELL 2 PLANE 1
324, MTM(3,1) * MEAN TIME CELL 3 PLANE 1
325, MTM(4,1) * MEAN TIME CELL 4 PLANE 1
326, MTM(5,1) * MEAN TIME CELL 5 PLANE 1
327, MTM(6,1) * MEAN TIME CELL 6 PLANE 1
328, MTM(7,1) * MEAN TIME CELL 7 PLANE 1
329, MTM(8,1) * MEAN TIME CELL 8 PLANE 1
330, MTM(9,1) * MEAN TIME CELL 9 PLANE 1
;
331, MTM(0,2) * MEAN TIME CELL 0 PLANE 2
332, MTM(1,2) * MEAN TIME CELL 1 PLANE 2
333, MTM(2,2) * MEAN TIME CELL 2 PLANE 2
334, MTM(3,2) * MEAN TIME CELL 3 PLANE 2
335, MTM(4,2) * MEAN TIME CELL 4 PLANE 2
336, MTM(5,2) * MEAN TIME CELL 5 PLANE 2
337, MTM(6,2) * MEAN TIME CELL 6 PLANE 2
338, MTM(7,2) * MEAN TIME CELL 7 PLANE 2
339, MTM(8,2) * MEAN TIME CELL 8 PLANE 2
340, MTM(9,2) * MEAN TIME CELL 9 PLANE 2
;
341, MTM(0,3) * MEAN TIME CELL 0 PLANE 3
```

```
342, MTM(1,3) * MEAN TIME CELL 1 PLANE 3
343, MTM(2,3) * MEAN TIME CELL 2 PLANE 3
344, MTM(3,3) * MEAN TIME CELL 3 PLANE 3
345, MTM(4,3) * MEAN TIME CELL 4 PLANE 3
346, MTM(5,3) * MEAN TIME CELL 5 PLANE 3
347, MTM(6,3) * MEAN TIME CELL 6 PLANE 3
348, MTM(7,3) * MEAN TIME CELL 7 PLANE 3
349, MTM(8,3) * MEAN TIME CELL 8 PLANE 3
350, MTM(9,3) * MEAN TIME CELL 9 PLANE 3
;
351, XDEV(0,1) * X-DEVIATION FROM FITTED COSMIC TRACK CELL 0 PLANE 1
352, XDEV(1,1) * X-DEVIATION FROM FITTED COSMIC TRACK CELL 1 PLANE 1
353, XDEV(2,1) * X-DEVIATION FROM FITTED COSMIC TRACK CELL 2 PLANE 1
354, XDEV(3,1) * X-DEVIATION FROM FITTED COSMIC TRACK CELL 3 PLANE 1
355, XDEV(4,1) * X-DEVIATION FROM FITTED COSMIC TRACK CELL 4 PLANE 1
356, XDEV(5,1) * X-DEVIATION FROM FITTED COSMIC TRACK CELL 5 PLANE 1
357, XDEV(6,1) * X-DEVIATION FROM FITTED COSMIC TRACK CELL 6 PLANE 1
358, XDEV(7,1) * X-DEVIATION FROM FITTED COSMIC TRACK CELL 7 PLANE 1
359, XDEV(8,1) * X-DEVIATION FROM FITTED COSMIC TRACK CELL 8 PLANE 1
360, XDEV(9,1) * X-DEVIATION FROM FITTED COSMIC TRACK CELL 9 PLANE 1
;
361, XDEV(0,2) * X-DEVIATION FROM FITTED COSMIC TRACK CELL 0 PLANE 2
362, XDEV(1,2) * X-DEVIATION FROM FITTED COSMIC TRACK CELL 1 PLANE 2
363, XDEV(2,2) * X-DEVIATION FROM FITTED COSMIC TRACK CELL 2 PLANE 2
364, XDEV(3,2) * X-DEVIATION FROM FITTED COSMIC TRACK CELL 3 PLANE 2
365, XDEV(4,2) * X-DEVIATION FROM FITTED COSMIC TRACK CELL 4 PLANE 2
366, XDEV(5,2) * X-DEVIATION FROM FITTED COSMIC TRACK CELL 5 PLANE 2
367, XDEV(6,2) * X-DEVIATION FROM FITTED COSMIC TRACK CELL 6 PLANE 2
368, XDEV(7,2) * X-DEVIATION FROM FITTED COSMIC TRACK CELL 7 PLANE 2
369, XDEV(8,2) * X-DEVIATION FROM FITTED COSMIC TRACK CELL 8 PLANE 2
370, XDEV(9,2) * X-DEVIATION FROM FITTED COSMIC TRACK CELL 9 PLANE 2
;
371, XDEV(0,3) * X-DEVIATION FROM FITTED COSMIC TRACK CELL 0 PLANE 3
372, XDEV(1,3) * X-DEVIATION FROM FITTED COSMIC TRACK CELL 1 PLANE 3
373, XDEV(2,3) * X-DEVIATION FROM FITTED COSMIC TRACK CELL 2 PLANE 3
374, XDEV(3,3) * X-DEVIATION FROM FITTED COSMIC TRACK CELL 3 PLANE 3
375, XDEV(4,3) * X-DEVIATION FROM FITTED COSMIC TRACK CELL 4 PLANE 3
376, XDEV(5,3) * X-DEVIATION FROM FITTED COSMIC TRACK CELL 5 PLANE 3
377, XDEV(6,3) * X-DEVIATION FROM FITTED COSMIC TRACK CELL 6 PLANE 3
378, XDEV(7,3) * X-DEVIATION FROM FITTED COSMIC TRACK CELL 7 PLANE 3
379, XDEV(8,3) * X-DEVIATION FROM FITTED COSMIC TRACK CELL 8 PLANE 3
380, XDEV(9,3) * X-DEVIATION FROM FITTED COSMIC TRACK CELL 9 PLANE 3
;
381, TDEV(0,1) * T-DEVIATION FROM FITTED COSMIC TRACK CELL 0 PLANE 1
382, TDEV(1,1) * T-DEVIATION FROM FITTED COSMIC TRACK CELL 1 PLANE 1
383, TDEV(2,1) * T-DEVIATION FROM FITTED COSMIC TRACK CELL 2 PLANE 1
384, TDEV(3,1) * T-DEVIATION FROM FITTED COSMIC TRACK CELL 3 PLANE 1
385, TDEV(4,1) * T-DEVIATION FROM FITTED COSMIC TRACK CELL 4 PLANE 1
386, TDEV(5,1) * T-DEVIATION FROM FITTED COSMIC TRACK CELL 5 PLANE 1
387, TDEV(6,1) * T-DEVIATION FROM FITTED COSMIC TRACK CELL 6 PLANE 1
388, TDEV(7,1) * T-DEVIATION FROM FITTED COSMIC TRACK CELL 7 PLANE 1
389, TDEV(8,1) * T-DEVIATION FROM FITTED COSMIC TRACK CELL 8 PLANE 1
390, TDEV(9,1) * T-DEVIATION FROM FITTED COSMIC TRACK CELL 9 PLANE 1
;
391, TDEV(0,2) * T-DEVIATION FROM FITTED COSMIC TRACK CELL 0 PLANE 2
392, TDEV(1,2) * T-DEVIATION FROM FITTED COSMIC TRACK CELL 1 PLANE 2
```

```
393, TDEV(2,2) * T-DEVIATION FROM FITTED COSMIC TRACK CELL 2 PLANE 2
394, TDEV(3,2) * T-DEVIATION FROM FITTED COSMIC TRACK CELL 3 PLANE 2
395, TDEV(4,2) * T-DEVIATION FROM FITTED COSMIC TRACK CELL 4 PLANE 2
396, TDEV(5.2) * T-DEVIATION FROM FITTED COSMIC TRACK CELL 5 PLANE 2
397, TDEV(6,2) * T-DEVIATION FROM FITTED COSMIC TRACK CELL 6 PLANE 2
398, TDEV(7,2) * T-DEVIATION FROM FITTED COSMIC TRACK CELL 7 PLANE 2
399, TDEV(8,2) * T-DEVIATION FROM FITTED COSMIC TRACK CELL 8 PLANE 2
400, TDEV(9,2) * T-DEVIATION FROM FITTED COSMIC TRACK CELL 9 PLANE 2
;
401, TDEV(0,3) * T-DEVIATION FROM FITTED COSMIC TRACK CELL 0 PLANE 3
402, TDEV(1,3) * T-DEVIATION FROM FITTED COSMIC TRACK CELL 1 PLANE 3
403, TDEV(2,3) * T-DEVIATION FROM FITTED COSMIC TRACK CELL 2 PLANE 3
404, TDEV(3,3) * T-DEVIATION FROM FITTED COSMIC TRACK CELL 3 PLANE 3
405, TDEV(4,3) * T-DEVIATION FROM FITTED COSMIC TRACK CELL 4 PLANE 3
406, TDEV(5,3) * T-DEVIATION FROM FITTED COSMIC TRACK CELL 5 PLANE 3
407, TDEV(6,3) * T-DEVIATION FROM FITTED COSMIC TRACK CELL 6 PLANE 3
408, TDEV(7,3) * T-DEVIATION FROM FITTED COSMIC TRACK CELL 7 PLANE 3
409, TDEV(8,3) * T-DEVIATION FROM FITTED COSMIC TRACK CELL 8 PLANE 3
410, TDEV(9,3) * T-DEVIATION FROM FITTED COSMIC TRACK CELL 9 PLANE 3
;
411, PHCR(0,1) * COSMIC-RAY PULSE-HEIGHT RATIO CELL 0 PLANE 1
412, PHCR(1,1) * COSMIC-RAY PULSE-HEIGHT RATIO CELL 1 PLANE 1
413, PHCR(2,1) * COSMIC-RAY PULSE-HEIGHT RATIO CELL 2 PLANE 1
414, PHCR(3,1) * COSMIC-RAY PULSE-HEIGHT RATIO CELL 3 PLANE 1
415, PHCR(4,1) * COSMIC-RAY PULSE-HEIGHT RATIO CELL 4 PLANE 1
416, PHCR(5,1) * COSMIC-RAY PULSE-HEIGHT RATIO CELL 5 PLANE 1
417, PHCR(6,1) * COSMIC-RAY PULSE-HEIGHT RATIO CELL 6 PLANE 1
418, PHCR(7,1) * COSMIC-RAY PULSE-HEIGHT RATIO CELL 7 PLANE 1
419, PHCR(8,1) * COSMIC-RAY PULSE-HEIGHT RATIO CELL 8 PLANE 1
420, PHCR(9,1) * COSMIC-RAY PULSE-HEIGHT RATIO CELL 9 PLANE 1
;
421, PHCR(0,2) * COSMIC-RAY PULSE-HEIGHT RATIO CELL 0 PLANE 2
422, PHCR(1,2) * COSMIC-RAY PULSE-HEIGHT RATIO CELL 1 PLANE 2
423, PHCR(2,2) * COSMIC-RAY PULSE-HEIGHT RATIO CELL 2 PLANE 2
424, PHCR(3,2) * COSMIC-RAY PULSE-HEIGHT RATIO CELL 3 PLANE 2
425, PHCR(4,2) * COSMIC-RAY PULSE-HEIGHT RATIO CELL 4 PLANE 2
426, PHCR(5,2) * COSMIC-RAY PULSE-HEIGHT RATIO CELL 5 PLANE 2
427, PHCR(6,2) * COSMIC-RAY PULSE-HEIGHT RATIO CELL 6 PLANE 2
428, PHCR(7,2) * COSMIC-RAY PULSE-HEIGHT RATIO CELL 7 PLANE 2
429, PHCR(8,2) * COSMIC-RAY PULSE-HEIGHT RATIO CELL 8 PLANE 2
430, PHCR(9,2) * COSMIC-RAY PULSE-HEIGHT RATIO CELL 9 PLANE 2
;
431, PHCR(0,3) * COSMIC-RAY PULSE-HEIGHT RATIO CELL 0 PLANE 3
432, PHCR(1,3) * COSMIC-RAY PULSE-HEIGHT RATIO CELL 1 PLANE 3
433, PHCR(2,3) * COSMIC-RAY PULSE-HEIGHT RATIO CELL 2 PLANE 3
434, PHCR(3,3) * COSMIC-RAY PULSE-HEIGHT RATIO CELL 3 PLANE 3
435, PHCR(4,3) * COSMIC-RAY PULSE-HEIGHT RATIO CELL 4 PLANE 3
436, PHCR(5,3) * COSMIC-RAY PULSE-HEIGHT RATIO CELL 5 PLANE 3
437, PHCR(6,3) * COSMIC-RAY PULSE-HEIGHT RATIO CELL 6 PLANE 3
438, PHCR(7,3) * COSMIC-RAY PULSE-HEIGHT RATIO CELL 7 PLANE 3
439, PHCR(8,3) * COSMIC-RAY PULSE-HEIGHT RATIO CELL 8 PLANE 3
440, PHCR(9,3) * COSMIC-RAY PULSE-HEIGHT RATIO CELL 9 PLANE 3
;
;**** bookkeeping data words ************
;
501, MULT(1) * MULTIPLICITY PLANE 1
```

```
502, MULT(2) * MULTIPLICITY PLANE 2
503, MULT(3) * MULTIPLICITY PLANE 3
504, NPLHIT  * NUMBER OF PLANES HIT
;
505, CELL(1) * CELL ID PLANE 1: NOT VALID FOR MULT>2,CSEP>1
506, CELL(2) * CELL ID PLANE 2: NOT VALID FOR MULT>2,CSEP>1
507, CELL(3) * CELL ID PLANE 3: NOT VALID FOR MULT>2,CSEP>1
508, C1C2    * EVENT TYPE COUNTER (SAME AS IUCF D1D2)
;
509, CSEP(1) * CELL SEPARATION FOR MULT=2 PLANE 1
510, CSEP(2) * CELL SEPARATION FOR MULT=2 PLANE 2
511, CSEP(3) * CELL SEPARATION FOR MULT=2 PLANE 3
;
512, RANDM   * RANDOM NUMBER BETWEEN 0 AND 1
513, TRF     * GAIN-MATCHED AND OFFSET RFO STOP TIME
514, TEPMON  * GAIN-MATCHED EP MONITOR TIME WRT TRF
515, TNTMON  * GAIN-MATCHED NT MONITOR TIME WRT TRF
;
;*** data words assigned to planes **************************
;
521, XDFP(1) * POSITION DIFFERENCE PLANE 1
522, XDFP(2) * POSITION DIFFERENCE PLANE 2
523, XDFP(3) * POSITION DIFFERENCE PLANE 3
;
524, PHGP(1) * GEOM. MEAN P.H. FOR PLANE 1
525, PHGP(2) * GEOM. MEAN P.H. FOR PLANE 2
526, PHGP(3) * GEOM. MEAN P.H. FOR PLANE 3
;
527, XTMP(1) * X POSITION FOR PLANE 1
528, XTMP(2) * X POSITION FOR PLANE 2
529, XTMP(3) * X POSITION FOR PLANE 3
;
530, YP(1) * Y POSITION FOR PLANE 1
531, YP(2) * Y POSITION FOR PLANE 2
532, YP(3) * Y POSITION FOR PLANE 3
;
533. TOFP(1) * TOF FOR PLANE 1
534, TOFP(2) * TOF FOR PLANE 2
535, TOFP(3) * TOF FOR PLANE 3
;
536, MNTMP(1) * MEAN TIME FOR PLANE 1
537, MNTMP(2) * MEAN TIME FOR PLANE 2
538, MNTMP(3) * MEAN TIME FOR PLANE 3
;
;*** differences for double hit events
;
551, XDFM2(1) * X POSITION DIFFERENCE FOR DOUBLE HITS PLANE 1
552, XDFM2(2) * X POSITION DIFFERENCE FOR DOUBLE HITS PLANE 2
553, XDFM2(3) * X POSITION DIFFERENCE FOR DOUBLE HITS PLANE 3
;
554, TDFM2(1) * TIME DIFFERENCE FOR DOUBLE HITS PLANE 1
555, TDFM2(2) * TIME DIFFERENCE FOR DOUBLE HITS PLANE 2
556, TDFM2(3) * TIME DIFFERENCE FOR DOUBLE HITS PLANE 3
;
;*** cosmic ray quantities
;
```

```
560, MSDX(1) * MEAN SQ X DEV FROM FITTED COSMIC RAY TRACK PLANE 1
561, MSDX(2) * MEAN SQ X DEV FROM FITTED COSMIC RAY TRACK PLANE 2
562, MSDX(3) * MEAN SQ X DEV FROM FITTED COSMIC RAY TRACK PLANE 3
;
563, MSDT(1) * MEAN SQ T DEV FROM FITTED COSMIC RAY TRACK PLANE 1
564, MSDT(2) * MEAN SQ T DEV FROM FITTED COSMIC RAY TRACK PLANE 2
565, MSDT(3) * MEAN SQ T DEV FROM FITTED COSMIC RAY TRACK PLANE 3
;
566, ZANG(1) * ZENITH ANGLE FOR COSMIC TRACKS PLANE 1
567, ZANG(2) * ZENITH ANGLE FOR COSMIC TRACKS PLANE 2
568, ZANG(3) * ZENITH ANGLE FOR COSMIC TRACKS PLANE 3
;
569, PHAVG(1) * AVERAGE COSMIC-RAY PULSE HEIGHT PLANE 1
570, PHAVG(2) * AVERAGE COSMIC-RAY PULSE HEIGHT PLANE 2
571, PHAVG(3) * AVERAGE COSMIC-RAY PULSE HEIGHT PLANE 3
;
;**** kinematic, ratio, and angle data words ***********
;
581, T1        * KINETIC ENERGY OF INCIDENT NUCLEON
582, PHNP      * NORMALIZED BACKPLANE DELTA-E
583, DTOF      * TOF BETWEEN FRONT AND BACK
584, DELX      * X DIFF BETWEEN FRONT AND BACK
585, DELY      * Y DIFF BETWEEN FRONT AND BACK
586, RAD1      * RADIUS FROM CENTER OF NAO
;
;** ratios:
;
590, VSCAT     * VELOCITY/C  OF SCATTERED PARTICLE
591, VRATIO    * (SCATTERED VELOCITY)/(FREE NN SCATTERED VELOCITY)
592, PHT1      * (ANALYZER PH)/(INC KINETIC ENG)
593, PHTR      * (ANALYZER PH)/(NN RECOIL ENG)
;
;** angles
;
595, THTFB     * POLAR SCATTERING ANGLE FROM FRONT TO BACK
596, PHI       * AZIMUTHAL ANGLE (LEFT<0, RIGHT>0)
597, SINTH2    * SIN(THETA)**2
;
;** projected target position (useful with p,p events)
;
600, ZTGT * PROJECTED Z OF TARGET
601, XTGT * PROJECTED X OF TARGET
602, YTGT * PROJECTED Y OF TARGET
;
```

REFERENCES

1. G. W. Hoffmann, G. Blanpied, W. R. Coker, R. Liljestrand, L. Ray, J. Spencer, H. Thiessen, N. Hintz, M. Oothoudt, T. Bauer, G. Igo, G. Pauletta, J. Soukup, C. Whitten Jr., D. Madland, J. Pratt, H. Nann, K. Seth, C. Glasshausser, D. McDaniels, J. Tinsley, and P Varghese,, Phys. Rev. Lett. 40, 1256 (1978).

2. G. W. Hoffmann, G. Blanpied, W. R. Coker, R. Liljestrand, L. Ray, J. Spencer, H. Thiessen, N. Hintz, M. Oothoudt, T. Bauer, G. Igo, G. Pauletta, J. Soukup, C. Whitten Jr., H. Nann, K. Seth, C. Glasshausser, D. McDaniels, J. Tinsley, and P Varghese, Phys. Lett. 76B, 383 (1978).

3. G. W. Hoffmann, L. Ray, M. Barlett, R. Fergerson. J. McGill, E. C. Milner, K. Seth, D. Barlow, M. Bosko, S. Iverson, M. Kaletka, A. Saha, and D. Smith, Phys. Rev. Lett. 47, 1436 (1981).

4. D. Hutcheon, J. Cameron, R. Liljestrand, P. Kitching, C. Miller, W. McDonald, D. Sheppard, W. Olsen, G. Neilson, H. Sherif, D. McDaniels, J. Tinsley, L. Swenson, P. Schwandt, C. Stronach, and L. Ray, Phys. Rev. Lett. 47, 315 (1981).

5. L. Ray and J. R. Shepard, private communication.

6. L. Ray and J. R. Shepard, private communication.

7. C. J. Horowitz, Phys. Rev. C31, 1340 (1985).

8. J. A. Tjon and S. J. Wallace, Phys. Rev. C32, 1667 (1985); C35, 280 (1987); C32,267 (1985); C36, 1085 (1987).

9. D. P. Murdock and C. J. Horowitz, Phys. Rev. C35, 1442 (1987).

10. H. Palevsky, J. Friedes, R. Sutter, G. Bennett, G. Igo, W. Simpson, G. Phillips, D. Corley, N. Wall, R. Stearns, and B. Gottschalk, Phys. Rev. Lett. 18, 1200 (1967).

11. G. D. Alkhazov, G. M. Amalsky, S. L. Belostotsky, A. A. Vorobyov, O. A. Domchenkov, Yu. V. Dotsenko, and V. E. Starodubsky, Phys. Lett. 42B, 121 (1972).

12. R. Bertini, R. Beurtey, F. Brouchard, G. Bruge, H. Catz, A. Chaumeaux, J. M. Durand, J. C. Faivre, J. M. Fontaine, D. Garreta, C. Gustafsson, D. Hendrie, F. Hibou, D. Legrand, J. Saudinos, and J. Thiron, Phys Lett. 45B, 119 (1973).

13. G. W. Hoffmann, in Proceedings of the LAMPF Workshop on Dirac Approaches to Nuclear Physics, edited by J. R. Shepard, C. Y. Cheung and R. L. Boudrie (LAMPF report LA-10438-C, 1985) p. 28.

14. B. C. Clark, L. Arnold, R. Mercer, Contribution 4C5, Eighth International Conference on High Energy Physics and Nuclear Structure, Vancouver (1979).

15. A. K. Kerman, H. McManus, and R. M. Thaler, Ann. Phys. (N.Y.) 8, 551 (1959).

16. R. J. Glauber and P. Osland, Phys. Lett. 80B, 401 (1979).

17. B. C. Clark, R. L. Mercer, and P. Schwandt, Phys. Lett. 122B, 211 (1983).

18. D. E. Bainum, J. Rapaport, C. D. Goodman, D. J. Horen, C. C. Foster, M. B. Greenfield, and C. A. Goulding, Phys. Rev. Lett. 44, 1751 (1980).

19. T. N. Taddeucci, Measurement of $D_{LL}(0°)$ for $1^{\pm}$ (p,n) Transitions in p-shell Nuclei, LAMPF Proposal 1137.

20. J. R. Shepard, in Proceedings of the LAMPF Workshop on Physics with Polarized Targets, edited by J. Burleson, W. Gibbs, G. Hoffmann, J. Jarmer, N. Tanaka (LAMPF report LA-10772-C, 1986) p. 73.

21. T. N. Taddeucci, J. Phys. Soc. Jpn. 55 Supple. 156 (1986).

22. M. S. Livingston, "LAMPF: A Nuclear Research Facility," Los Alamos Scientific Laboratory report LA-6878-MS (September, 1977).

23. "LAMPF" , J. C. Allred and B. Talley, Ed., Los Alamos Scientific Laboratory report LA-UR-87-327 (January, 1987).

24. J. B. McClelland, D. A. Clark, J. L. Davis, R. C. Haight, R. W. Johnson, N. S. P. King, G. L. Morgan, L. R. Rybarcyk, W. R. Smythe, D. A. Lind, C. D. Zafiratos, "Longitudinal LINAC Beam Focusing for Neutron Time-Of-Flight Measurements", to be published.

25. M. W. McNaughton, and E. P. Chamberlin, Phys. Rev. C24, 1778 (1981).

26. T. A. Carey, private communication.

27. D. A. Kellogg, Phys. Rev. 90, 224 (1953).

28. W. C. Sailor, R. C. Byrd, and Y. Yariv, TRACE: A Monte Carlo Code for the Efficiency of Muli-Element Neutron Scintillator Detectors, (LANL Report LA-11348-MS, 1988).

29. J. B. McClelland, private communication.

30. B. Zacharov, "CAMAC Systems: A Pedestrians Guide," Daresbury Nuclear Physics Laboratory report WA4-4AD, Warrington, England (1972).

31. J. F. Amann, "Summary of FERA Notes", unpublished (June 1987).

32. S. Shlaer, "An MBD Primer," Los Alamos Scientific Laboratory report LA-5511-MS (August, 1974).

33. "A Histogramming System under RSX 11M and VMS," Los Alamos National Laboratory Document MP-1-3407-4 (February, 1985).

34. "Histogramming Support Systems Under RSX 11M and VMS," Los Alamos National Laboratory Document MP-1-3403-4 (March, 1986).

35. "A Data Testing Package Under RSX 11M and VMS," Los Alamos National Laboratory Document MP-1-3412-3 (February, 1985).

36. "Users Manual (preliminary)," Indiana University Cyclotron Facility Document (April, 1974).

37. P. R. Bevington, Data Reduction and Error Analysis for the Physical Sciences, (McGraw-Hill, New York, 1969) p.73.

38. L. J. Rybarcyk et al. "Program GAUFIT" , unpublished.

39. J. Amann, "Program PEK", unpublished.

40. J. D'Auria, M. Dombsky, L. Moritz, T. Ruth, G. Sheffer, T. E. Ward, C. C. Foster, J. W. Watson, B. D. Anderson, J. Rapaport, Phys. Rev. C30, 1999 (1984).

41. T. N. Taddeucci, C. A. Goulding, T. A. Carey, R. C. Byrd, C. D. Goodman, C. Gaarde, J. Larson, D. J. Horen, J. Rapaport, E. Sugarbaker, Nuclear Physics A469, 125 (1987).

42. C. D. Goodman, C. A. Goulding, M. B. Greenfield, J. Rapaport, D. E. Bainum, C. C. Foster, W. G. Love, and F. Petrovich, Phys Rev. Lett. 44, 1755 (1980).

43. W. G. Love, K. Nakayama, and M. A. Franey, Phys. Rev. Lett. 59, 1401 (1987).

44. T. N. Taddeucci, J. Rapaport, D.E. Bainum, C. Gaarde, J. Larson, C. D. Goodman, D. J. Horen, T. Masterson, C. A. Goulding, E. Sugarbaker, C. C. Foster, Phys. Rev. C25, 1094 (1981).

45. J. R. Shepard, private communication.

46. R. Schaeffer and J. Raynal, "DWBA70" program unpublished. J. R. Comfort, "DW81" revised program unpublished.

47. M. A. Franey and W. G. Love, Phys. Rev. C31, 488 (1985).

48. K. W. Jones, C. Glashausser, R. de Swiniarski, S. Nanda, T. A. Carey, W. Cornelius, J. M. Moss, J. B. McClelland, J. R. Comfort, J. L. Escudie, M. Gazzaly, N. Hintz, G. Igo, M. Haji-Saeid, C. A. Whitten, Jr., Phys. Rev. C33, 17 (1986).

49. S. Cohen, and D. Kurath, Nuclear Physics 73, 1 (1965).

50. T. -S. H. Lee, and D. Kurath, Phys. Rev. C21, 293 (1980).

51. J. Rapaport, D. Wang, J. A. Carr, F. Perovich, C. C. Foster, C. D. Goodman, C. Gaarde, J. Larsen, C. A. Goulding, T. N. Taddeucci, D. Horen, E. Sugarbaker, Phys. Rev. C36, 500 (1987).

52. C. J. Horowitz, Phys. Lett. B196, 285 (1987).

53. J. A. Tjon and S. J. Wallace, Phys Rev. C32, 1667 (1985); C35, 280 (1987); C32, 267 (1985); and C36, 1085 (1987).

☆U.S. GOVERNMENT PRINTING OFFICE: 1989-773-034/00216